

The optical morphologies of the 2Jy sample of radio galaxies: evidence for galaxy interactions

C. Ramos Almeida^{1*}, C. N. Tadhunter¹, K. J. Inskip², R. Morganti^{3,4}, J. Holt⁵, & D. Dicken⁶

¹*Department of Physics and Astronomy, University of Sheffield, Sheffield, S3 7RH, UK*

²*Max-Planck-Institut für Astronomie, Königstuhl 17, D-69117 Heidelberg, Germany*

³*Netherlands Institute for Radio Astronomy, Postbus 2, 7990 AA Dwingeloo, the Netherlands*

⁴*Kapteyn Astronomical Institute, University of Groningen, Postbus 800, 9700 AV Groningen, the Netherlands*

⁵*Leiden Observatory, Leiden University, PO Box 9513, 2300 RA Leiden, the Netherlands*

⁶*Department of Physics and Astronomy, Rochester Institute of Technology, 84 Lomb Memorial Drive, Rochester NY 14623, USA*

ABSTRACT

We present deep GMOS-S/Gemini optical broad-band images for a complete sample of 46 southern 2Jy radio galaxies at intermediate redshifts ($0.05 < z < 0.7$). Based on them, we discuss the role of galaxy interactions in the triggering of powerful radio galaxies (PRGs). The high-quality observations presented here show for the first time that the overall majority of PRGs at intermediate redshifts (78–85%) show peculiarities in their optical morphologies at relatively high levels of surface brightness ($\bar{\mu}_V = 23.6 \text{ mag arcsec}^{-2}$; $\Delta\mu_V \simeq [21, 26] \text{ mag arcsec}^{-2}$). The observed morphological peculiarities include tails, fans, bridges, shells, dust lanes, irregular features, amorphous haloes, and multiple nuclei. While the results for many of the galaxies are consistent with them being observed at, or after, the time of coalescence of the nuclei in a galaxy merger, we find that more than one-third of the sample are observed in a pre-coalescence phase of the merger, or following a close encounter between galaxies that will not necessarily lead to a merger. By dividing the sample into Weak-Line Radio Galaxies (WLRGs; 11 objects) and Strong-Line Radio Galaxies (SLRGs; 35 objects) we find that only 27% of the former show clear evidence for interactions in their optical morphologies, in contrast to the SLRGs, of which at least 94% appear interacting. This is consistent with the idea that many WLRGs are fuelled/triggered by Bondi accretion of hot gas. However, the evidence for interactions and dust features in a fraction of them indicates that the accretion of cold gas cannot always be ruled out. Of the 28% of the sample that display evidence for significant starburst activity, we find that 92% present disturbed morphologies, following the same general trend as the total and SLRG samples. By comparing our PRGs with various samples of quiescent ellipticals from the literature, we conclude that the percentage of morphological disturbance that we find here exceeds that found for quiescent ellipticals when similar surface brightnesses are considered. Overall, our study indicates that galaxy interactions are likely to play a key role in the triggering of AGN/jet activity.

Key words: galaxies: active – galaxies: nuclei – galaxies: interactions – galaxies: photometry.

1 INTRODUCTION

Over recent years, substantial evidence has accumulated for links between Active Galactic Nuclei (AGN) activity and the evolution of galaxies (e.g., Cattaneo et al. 2009). Not only are the masses of the central black holes (BHs) which power the AGN tightly correlated with the prop-

erties of the bulges of the host galaxies (Gebhardt et al. 2000; Ferrarese & Merritt 2000; Greene & Ho 2006), but the variation in the co-moving number density of PRGs (Dunlop & Peacock 1990) bears a striking similarity to the evolution of the global star formation rate in the Universe (Madau et al. 1996). Simulations of hierarchical galaxy evolution predict that the periods of BH growth and AGN activity are intimately tied to the growth of the host galaxy, and that the triggering of the main phase of AGN

* E-mail: C.Ramos@sheffield.ac.uk

activity in gas-rich mergers will always be accompanied by a major galaxy-wide starburst (Kauffmann et al. 2000; Di Matteo et al. 2005; Springel et al. 2005; Hopkins et al. 2008a,b; Somerville et al. 2008). However, the timescales involved in both the triggering of the merger-induced starburst and the AGN activity remain uncertain.

In order to understand the symbiosis between galaxy evolution and AGN activity, it is important to test the models for the triggering of nuclear activity and starbursts (starbursts) using observations of well-defined samples of nearby AGN. Radio galaxies are particularly useful in this context because they are invariably associated with early-type hosts, allowing cleaner searches for signs of morphological disturbance and recent star formation activity.

Although morphological evidence for mergers/interactions has been found in some nearby radio galaxies (Heckman et al. 1986; Smith & Heckman 1989, hereafter H86, SH89), this mechanism for triggering the AGN activity is not without controversy (Dunlop et al. 2003; Grogin et al. 2005). On the one hand, using ground-based deep imaging observations SH89 found that over 50% of their sample of PRGs display morphological deviations from elliptical symmetry at high levels of surface brightness, and that about half of the PRGs with strong optical emission lines exhibit peculiar optical morphologies. These peculiarities include tails, fans, bridges, shells and dust lanes. More recently, Roche & Eales (2000) found that at least 13 out of 15 3CR radio galaxies with ground-based optical imaging appear to be interacting with neighbours, based on the projected separations of the galaxy pairs. On the other hand, the high spatial resolution Hubble Space Telescope (HST) images of a sample of nearby radio galaxies, radio-quiet quasars (QSOs) and radio-loud QSOs presented by Dunlop et al. (2003) indicated that they are hosted by relatively undisturbed giant elliptical galaxies. Indeed, the main conclusion of the latter work is that the hosts of radio-loud and radio-quiet AGN are indistinguishable from quiescent ellipticals of similar mass.

At least part of the discrepancy between the previous imaging results may be due to the differences in the depth of the ground- and space-based observations. Despite the higher spatial resolution of the HST images, the short exposure time data obtained by Dunlop et al. (2003) using the Wide Field Planetary Camera 2 (WFPC2)/HST are relatively insensitive to large-scale diffuse structures such as tidal tails, fans or shells. Indeed, Canalizo et al. (2007) and Bennert et al. (2008) recently presented deeper Advanced Camera for Surveys (ACS)/HST optical images (5 orbits) of five nearby QSOs classified by Dunlop et al. (2003) as undisturbed elliptical galaxies. These deeper images reveal shells and tidal tails in four of the five galaxies that were not apparent in the earlier HST observations.

The morphological features found by H86, SH89, and Roche & Eales (2000) can be the result of either mergers between gas-rich galaxies (i.e., late-type galaxies), gas-poor galaxies (those involving two early-type galaxies: the so-called “dry-mergers”) or galaxy encounters that will not lead to a merger. Dry-mergers have been shown to explain the observed properties of high-luminosity ($M_V \lesssim -21$) boxy, velocity dispersion-supported early-type galaxies (Naab et al. 2006), whereas simulations of merging disks easily reproduce the remnants of disk, rotationally-supported low-

luminosity elliptical galaxies (Toomre & Toomre 1972; Bendo & Barnes 2000; Naab et al. 1999; Naab & Burkert 2003). The morphological signatures of gas-poor interactions are normally very weak: e.g., broad and low surface brightness tidal tails, fans, asymmetries, and double nuclei (Borne 1984; Borne & Hoessel 1985; Combes et al. 1995; Naab et al. 2006; Bell et al. 2006). Given the small amount of cool gas involved in the interaction between elliptical galaxies, the gas disruption in such dry-mergers may result in only a small amount of star formation. In contrast, gas-rich interactions usually result in sharper, narrower and brighter tails, shells or fans. In this case, there is plenty of cold gas to trigger the star formation. In general, close pairs and gas-rich mergers are expected to be visible for a timescale between 0.5 and 1.5 Gyr (Le Fèvre et al. 2000; Patton et al. 2002; Conselice et al. 2003; Kawata et al. 2006), whereas dry-mergers are visible for only ~ 150 Myr (Bell et al. 2006). Considering that the AGN/jet activity in PRGs is estimated to last no longer than 100 Myr (Leahy et al. 1989), gas-rich merger signatures would be detectable once the radio/AGN activity faded, whereas the visible signs of a dry-merger would be roughly coincident with the PRG lifetime.

Although evidence for mergers and interactions is found in many PRGs, a subset presents optical morphologies and emission line kinematics that do not support the idea of the triggering of the radio activity via mergers. These include some central cluster galaxies surrounded by massive haloes of hot gas (Tadhunter et al. 1989; Baum et al. 1992). In such cases, the infall of cold gas condensing from the X-ray haloes in cooling flows has been suggested as a triggering mechanism (e.g., Tadhunter et al. 1989; Baum et al. 1992; Bremer et al. 1997). Also, it has been shown that the direct accretion of hot gas from the X-ray haloes of galaxies is a plausible mechanism for fuelling radio galaxies that lack strong emission lines, namely the Weak-Line Radio Galaxies (WLRGs; Allen et al. 2006; Best et al. 2006; Hardcastle et al. 2007; Balmaverde et al. 2008).

In order to test the idea that the powerful radio galaxies are triggered in galaxy interactions, and also to examine the diversity of triggering mechanisms, it is crucial to use deep imaging observations to determine the interaction status of the galaxies. In this, the first of two papers, we present deep imaging data for a complete sample of 46 intermediate redshift ($0.05 < z < 0.7$) 2Jy radio galaxies (Tadhunter et al. 1993, 1998), making a first qualitative study of the morphologies of the host galaxies. We search for signs of nearby companions, secondary nuclei, shells and extended low surface brightness features such as tidal tails and bridges. This represents the first systematic imaging study of a major sample of radio galaxies using an 8m telescope. In a forthcoming paper we will make a full quantitative assessment of the interaction status of the radio galaxies, and also quantify their environments, relating these properties to those of the AGN and stellar populations.

In Section 2, we present details of our sample of PRGs. Section 3 describes the observations and data reduction. A description of the image enhancement techniques employed in this work can be found in Section 4, and in Section 5 we present the observational results. Discussion and conclusions are presented in Sections 6 and 7, respectively. Finally, notes on the individual galaxies are reported in Appendix

A, and processed images for all the galaxies in the sample are shown in Appendix B. Throughout this paper we assume a cosmology with $H_0=73 \text{ km s}^{-1} \text{ Mpc}^{-1}$; $\Omega_m=0.27$, and $\Omega_\Lambda=0.73$.

2 SAMPLE SELECTION

The objects studied here comprise all powerful radio galaxies (PRGs) and quasars from the Tadhunter et al. (1993) sample of 2Jy radio galaxies with $S_{2.7\text{GHz}} \geq 2.0 \text{ Jy}$, steep radio spectra $\alpha_{2.7}^{4.8} > 0.5$ ($F_\nu \propto \nu^{-\alpha}$), declinations $\delta < +10^\circ$ and redshifts $0.05 < z < 0.7$ (see Table 1). It is itself a subset of the Wall & Peacock (1985) complete sample of 2Jy radio sources. We also included the source PKS 0347+05 (di Serego Alighieri et al. 1994), that was not in the original Tadhunter et al. (1993) sample, but subsequently proved to fulfil the same selection criteria. This sample is unique in terms of the depth, completeness, and quality of its supporting optical (Tadhunter et al. 1993, 1998, 2002; Holt et al. 2007), near-infrared (NIR; for the $z < 0.5$ subset; Inskip et al. 2010), mid- to far-infrared (Dicken et al. 2008, 2009, 2010), and radio data (Morganti et al. 1993, 1997, 1999), which provide an accurate picture, not only of the radio source and AGN properties, but also of the level of star formation in each host galaxy. Much of the existing information on this sample is summarized on the 2Jy website¹. For further details on sample selection and completeness see Tadhunter et al. (1993, 1998) and Dicken et al. (2008). The $z > 0.05$ limit ensures that the radio galaxies are genuinely powerful sources, while the $z < 0.7$ limit ensures that sources are sufficiently nearby for detailed morphological studies. In all the Tables and Appendices presented in this work the PRGs are ordered in redshift, from the most nearby sources to the most distant ones.

In terms of the optical classification, based on both previous optical spectra (Tadhunter et al. 1998) and on optical appearance (Wall & Peacock 1985), the sample comprises 24% WLRGs (sources with [O III] $\lambda 5007$ emission line equivalent widths below 10 Å), 43% Narrow-Line Radio Galaxies (NLRGs), and 33% Broad-Line Radio Galaxies and quasars (BLRGs and QSOs). The QSOs were classified by Wall & Peacock (1985) based on their stellar appearance on optical images, and later confirmed from optical spectroscopy (Tadhunter et al. 1998). BLRGs and NLRGs are defined on the basis of whether or not their optical spectra show broad line components of the permitted emission lines.

Considering the radio morphologies, Fanaroff-Riley II (FRII) sources constitute the majority of the sample (72%), 13% are Fanaroff-Riley I (FRI), and the remaining 15% correspond to compact, steep-spectrum (CSS) or Gigahertz-peaked spectrum (GPS) sources (Table 1). All FRIs in our sample are WLRGs according to their optical spectra. In contrast, the majority of FRII and CSS/GPS sources are classified as SLRGs, with a minority showing WLRG spectra. Only thirteen out of the 46 radio galaxies in the sample (28%) present any evidence of recent starburst activity, based on their optical spectra (Tadhunter et al. 1993), far-infrared (FIR) excess, and/or the detection of polycyclic

aromatic hydrocarbons (PAHs) in their mid-infrared (MIR) spectra (Dicken et al. 2008, 2009, 2010).

3 OBSERVATIONS AND DATA REDUCTION

Deep optical imaging data were obtained for the full sample using the Gemini Multi-Object Spectrograph South (GMOS-S) on the 8.1 m Gemini South telescope at Cerro Pachón, Chile. The observations were carried out in queue mode between July 2008 and April 2009 under good seeing conditions (median seeing FWHM = $0.8''$, ranging from $0.4''$ to $1.15''$), as required to allow the best chance to detect subtle morphological features. The seeing values were measured individually for each of the 46 GMOS-S images using foreground stars. Details of the observations are reported in Table 2. The GMOS-S detector (Hook et al. 2004) comprises three adjacent 2048x4096 pixel CCDs separated by two gaps of $\sim 2.8''$, giving a field-of-view (FOV) of $5.5 \times 5.5 \text{ arcmin}^2$, with a pixel size of $0.146'' \text{ pixel}^{-1}$.

With the exception of the source PKS 2250-41², all the galaxies with $z \lesssim 0.4$ were observed in the r' -band filter ($r\text{-G0326}$, $\lambda_{eff}=6300 \text{ Å}$, $\Delta\lambda=1360 \text{ Å}$), while those with $z > 0.4$ were observed in the i' -band ($i\text{-G0327}$, $\lambda_{eff}=7800 \text{ Å}$, $\Delta\lambda=1440 \text{ Å}$), in order to cover the typical rest frame wavelength range 4500-6000 Å. The GMOS-S r' and i' filters are very similar to the r and i used by the Sloan Digital Sky Survey (SDSS; see Fukugita et al. 1996 for details of the latter photometric system).

Depending on source brightness, and in order to avoid saturation of sources with either bright nuclei or close foreground stars, we took from four to sixteen images per filter, arranged in either 2x2 square or 3x2 rectangular dither pattern with a step size of $10''$. The purpose of the dithering is to eliminate the gaps between the three CCDs, remove other image blemishes, and improve flat fielding. For details of the dither patterns and exposure times for each source see Table 2. The total integration times (from 256s to 1500s depending on redshift) were designed to make the observations deep enough to detect features at relatively low levels of surface brightness. In addition to longer exposure images, the radio source PKS 1814-63 also has a short exposure time observation of 4x15s, which was obtained to avoid saturation of a foreground star in front of the galaxy (see Table 2). As well as the main science target fields, offset fields ($\sim 20'$ offset) were observed after each radio galaxy observation, in order to better quantify the background galaxy population of the host galaxies for future environmental studies. The latter data will be analyzed in a forthcoming paper.

The data were reduced using the GMOS dedicated software packages within the IRAF³ environment. The reduction process included bias subtraction and flat fielding, merging of the three separate CCD images comprising each

² Observed with the i' -band filter in order to avoid contamination by off-nuclear [O III] $\lambda 5007 \text{ Å}$ line emission, which we know is very prominent from optical spectra (Tadhunter et al. 2002).

³ IRAF is distributed by the National Optical Astronomy Observatory, which is operated by the Association of Universities for the Research in Astronomy, Inc., under cooperative agreement with the National Science Foundation (<http://iraf.noao.edu/>).

¹ <http://2jy.extragalactic.info>

PKS ID	Other	Optical	Radio	z	Scale	Distance	Morphology	Group
0620-52		WLRG*	FRI	0.051	965	220	...	5
0625-53		WLRG	FRI	0.054	1014	232	B	1
0915-11	Hydra A	WLRG*	FRI	0.054	1044	240	D	4
0625-35	OH-342	WLRG	FRI	0.055	1027	236	J	5
2221-02	3C445	BLRG	FRII	0.057	1027	236	F,S	1
1949+02	3C403	NLRG	FRII	0.059	1083	250	S,D	2
1954-55		WLRG	FRI	0.060	1075	248	...	5
1814-63		NLRG*	CSS	0.063	1160	270	2I,D	2
0349-27		NLRG	FRII	0.066	1215	285	2B,[S]	1
0034-01	3C15	WLRG	FRII	0.073	1316	312	J	5
0945+07	3C227	BLRG	FRII	0.086	1565	381	S	2
0404+03	3C105	NLRG	FRII	0.089	1593	398	[S]	5
2356-61		NLRG	FRII	0.096	1708	423	2S,F,I	2
1733-56		BLRG*	FRII	0.098	1743	433	2T,2I,2S,[D]	2
1559+02	3C327	NLRG	FRII	0.104	1854	467	2S,D,[2N]	2
0806-10	3C195	NLRG	FRII	0.110	1943	494	F,2S	2
1839-48		WLRG	FRI	0.112	1945	495	2N,S,[T]	2,3
0043-42		WLRG	FRII	0.116	2010	516	[2N],[B]	5
0213-13	3C62	NLRG	FRII	0.147	2464	668	2S,[T]	2
0442-28		NLRG	FRII	0.147	2474	671	S	2
2211-17	3C444	WLRG	FRII	0.153	2544	696	D,[F]	4
1648+05	Herc A	WLRG	FRII?	0.154	2574	707	D	4
1934-63		NLRG*	GPS	0.183	2961	854	2N,2T	1,3
0038+09	3C18	BLRG	FRII	0.188	3013	875	T	2
2135-14		QSO	FRII	0.200	3171	941	T,S,A,[B]	2
0035-02	3C17	BLRG	FRII	0.220	3408	1044	B,F,[S]	1
2314+03	3C459	NLRG*	FRII	0.220	3409	1044	2F,[T]	2
1932-46		BLRG*	FRII	0.231	3551	1109	2F,A,I	2
1151-34		QSO*	CSS	0.258	3873	1267	F,[S]	1
0859-25		NLRG	FRII	0.305	4362	1535	2N	3
2250-41		NLRG*	FRII	0.310	4393	1553	2B,[T],[F]	1
1355-41		QSO	FRII	0.313	4438	1580	S,T	2
0023-26		NLRG*	CSS	0.322	4508	1623	A,[D]	2
0347+05		WLRG*	FRII	0.339	4673	1727	B,3T,D	1
0039-44		NLRG	FRII	0.346	4734	1767	2N,3S,[T],[D]	2,3
0105-16	3C32	NLRG	FRII	0.400	5192	2096	B	1
1938-15		BLRG	FRII	0.452	5589	2428	F	2
1602+01	3C327.1	BLRG	FRII	0.462	5667	2500	F,S,[J]	2
1306-09		NLRG	CSS	0.464	5686	2518	2N,S	2,3
1547-79		BLRG	FRII	0.483	5810	2636	2N,T	2,3
1136-13		QSO	FRII	0.554	6276	3147	T,J	2
0117-15	3C38	NLRG	FRII	0.565	6303	3180	3N,S,I,[D]	2,3
0252-71		NLRG	CSS	0.566	6324	3207	[A]	5
0235-19	OD-159	BLRG	FRII	0.620	6592	3565	2T,[B]	2
2135-20	OX-258	BLRG*	CSS	0.635	6663	3669	F	2
0409-75		NLRG*	FRII	0.693	6925	4095	2N	3

Table 1. Full classification of the sample objects ordered by redshift. Columns 1 and 2 give the PKS and alternative names (if any) for the sample objects. Columns 3 and 4 give the spectroscopic class (* indicates evidence of starburst signatures) and radio morphology. Columns 5, 6, and 7 list the spectroscopic redshift as reported in the NASA/IPAC Extragalactic Database (NED), the scale in pc arcsec^{-1} (calculated using $H_0 = 73 \text{ km s}^{-1} \text{ Mpc}^{-1}$, $\Omega_{\text{matter}}=0.27$, $\Omega_{\text{vacuum}}=0.73$), and the luminosity distance (Mpc). Columns 8 and 9 correspond to our morphological classification (T: Tail; F: Fan; B: Bridge; S: Shell; D: Dust feature; 2N: Double Nucleus; 3N: Triple Nucleus; A: Amorphous Halo; I: Irregular feature; and J: Jet; brackets indicate uncertain identification of the feature), and sample division in 1) galaxy pair or group in tidal interaction; 2) galaxies showing T,F,S,D,A,I; 3) multiple nuclei (inside a 9.6 kpc); 4) galaxies with dust as the only detected feature, 5) isolated galaxies with no sign of interaction.

exposure into a single combined frame, and finally, production of a single image by combining the mosaicked frames. For the i' -band images, an additional step was necessary to remove the fringing that is significant for this filter. The dithered images were median-combined without aligning them after the objects were masked, resulting in an image of the fringe pattern only. This master fringe frame was

later subtracted from the individual frames before coadding them.

In order to calibrate the data in terms of a magnitude scale, observations of several Landolt photometric standard stars were taken on the same nights as the target radio galaxies. Using the latter to determine the photometric zero points, we estimate that the photometric accuracy of the

PKS ID	Exptime (s)	Obs. date	Seeing	Filter	A _λ (mag)	Mag (AB)	Mag (corr)
0620-52	100x8	2008-10-24	0.70''	r'	0.181	13.75	13.51
0625-53	100x8	2008-11-01	1.00''	r'	0.250	13.81	13.49
0915-11	67x16	2009-02-20	1.00''	r'	0.109	14.33	14.15
0625-35	90x8	2008-11-01	1.00''	r'	0.176	14.22	13.98
2221-02	16x16	2008-09-24	0.60''	r'	0.220	15.25	14.96
1949+02	100x8	2008-08-05	0.70''	r'	0.505	14.98	14.40
1954-55	62x16	2008-08-08	0.85''	r'	0.153	14.88*	14.65*
1814-63	67x16/15x4	2009-04-21/23	0.70''/0.65''	r'	0.228	15.84*	15.53*
0349-27	100x8	2008-08-30	0.85''	r'	0.024	15.83	15.72
0034-01	100x8	2008-10-06	0.85''	r'	0.057	15.23	15.08
0945+07	67x16	2009-02-21	0.85''	r'	0.069	16.02	15.85
0404+03	250x4	2008-10-24	0.70''	r'	1.264	17.67	16.30
2356-61	100x8	2008-08-26	1.00''	r'	0.036	15.82	15.67
1733-56	125x8	2009-04-03	0.55''	r'	0.264	16.00	15.62
1559+02	67x16	2009-03-25	0.95''	r'	0.237	15.84	15.48
0806-10	125x8	2009-02-19	0.70''	r'	0.225	16.06	15.70
1839-48	125x8	2009-04-03	0.75''	r'	0.178	15.67	15.36
0043-42	250x4	2008-08-10	0.80''	r'	0.031	16.20	16.03
0213-13	250x4	2008-10-28	0.85''	r'	0.054	16.69	16.46
0442-28	250x4	2008-10-23	0.55''	r'	0.087	16.80	16.54
2211-17	250x4	2008-08-26	0.85''	r'	0.067	17.01	16.76
1648+05	250x8	2009-03-25	0.85''	r'	0.251	17.79	17.35
1934-63	250x4	2008-07-25	0.65''	r'	0.226	17.75	17.30
0038+09	250x4	2008-10-24	1.00''	r'	0.422	18.34	17.69
2135-14	35x12	2008-09-24	0.55''	r'	0.139	16.41	16.03
0035-02	250x4	2008-08-09	0.60''	r'	0.062	18.16	17.83
2314+03	250x4	2008-10-06	1.10''	r'	0.173	17.48	17.04
1932-46	300x4	2008-07-25	0.80''	r'	0.144	18.68	18.25
1151-34	250x4	2009-02-22	0.55''	r'	0.219	17.75	17.21
0859-25	300x4	2009-02-21	0.85''	r'	0.546	18.80	17.85
2250-41	167x6	2008-08-04	1.00''	i'	0.025	16.58	16.32
1355-41	67x16	2009-03-19	0.40''	r'	0.232
0023-26	300x5	2008-08-04	0.90''	r'	0.042	19.08	18.60
0347+05	300x4	2008-10-07	0.50''	r'	0.745	19.68	18.46
0039-44	300x4	2008-08-09	0.55''	r'	0.021	18.82	18.31
0105-16	300x4	2008-10-26	0.85''	i'	0.041	19.02	18.66
1938-15	250x6	2008-07-25	0.80''	i'	0.465	19.30	18.47
1602+01	168x6	2009-03-02	0.70''	i'	0.250	18.93	18.31
1306-09	167x6	2009-02-24	0.55''	i'	0.087	18.79	18.33
1547-79	167x6	2009-02-25	0.80''	i'	0.402	18.36	17.56
1136-13	83x12	2009-02-05	0.80''	i'	0.074	16.50	15.94
0117-15	250x6	2008-10-22	0.50''	i'	0.035	19.19	18.66
0252-71	250x6	2008-10-28	1.00''	i'	0.058	20.46	19.90
0235-19	250x6	2008-10-28	0.70''	i'	0.062	19.11	18.44
2135-20	250x6	2008-08-05	0.95''	i'	0.064	19.09	18.38
0409-75	250x6	2008-10-01	1.15''	i'	0.148	20.54	19.57

Table 2. Summary of observations. Columns 1, 2, and 3 give the PKS name, the exposure times, and the date of observation. Columns 4 and 5 list the measured seeing and the filter employed in each observation. Column 6 gives either the A_{r'} or A_{i'} (see column 5) values determined using the E(B-V) values from the NASA/IPAC IRSA and the Galactic extinction law of Cardelli et al. (1989). Two last columns (7 and 8) correspond to the apparent magnitudes of the galaxies in a 30 kpc diameter metric aperture after removing the flux from any contaminating object and the K-corrected magnitudes in both r' and i' filters using Fukugita et al. (1995) K-corrections. All the magnitudes are also corrected for Galactic extinction. * The determination of these magnitudes was particularly difficult due to the presence of a bright foreground star in front of the galaxies. We do not report any magnitude values for PKS 1355-41 because the galaxy nucleus is saturated.

observations is ± 0.04 mag in both r' and i' bands. Column 7 of Table 2 lists the aperture magnitudes in the AB system using a fixed metric aperture of 30 kpc for each source. We have corrected these magnitudes for any contaminating objects (e.g., foreground stars and small companion galaxies) that are close enough to the science target to be contained in our fixed aperture. In some cases, the presence of saturated or near-saturated stars very close to the radio galaxy

complicates the determination of the aperture magnitudes (e.g., PKS 1954-55 and PKS 1814-63).

Considering the relatively large range of redshift spanned by the galaxies in our sample, it is necessary to apply K-corrections to the aperture magnitudes in order to make them comparable. In order to do this, we made use of the values reported in Frei & Gunn (1994) and Fukugita et al. (1995) for elliptical galaxies. Column 8 of

Table 2 presents the aperture magnitudes from column 7, K-corrected and Galactic extinction-corrected. For the galactic extinction correction, we made use of the E(B-V) values from Schlegel et al. (1998) and the Galactic extinction law of Cardelli et al. (1989) to derive the corresponding $A_{r'}$ and $A_{i'}$ values (see Table 2).

4 DATA ANALYSIS

The main aim of this work is to take advantage of our deep GMOS-S images to detect fine structure in the optical morphologies of powerful radio galaxies, such as tidal features, multiple nuclei, and dust (see description in Section 5.1). Our primary morphological assessment of each galaxy was based on visual inspection of the fully-reduced GMOS-S images. However, in order to improve our sensitivity to faint structure, we have also made use of three image enhancement techniques, which have been shown to greatly improve the search for faint features in elliptical galaxies: 1) image filtering; 2) unsharp-masking; and 3) smoothed galaxy subtraction. All these techniques have been applied to the data using the Interactive Data Language (IDL).

- *Image filtering.* This enhancement technique computes the median of the pixels contained in a moving square box of a given width, replacing the central pixel with the computed median (i.e., the image is smoothed; McGaugh & Bothun 1990). It also processes the pixels at the edges and corners of the images, and it is possible to apply iterative smoothing. For the GMOS-S images, we used a box width of 5 pixels, with the exception of two galaxies with large-scale tidal features (PKS 0038+09 and PKS 0349-27) for which we employed larger box width values (10 and 20 pixels, respectively). By median-filtering the images, large and/or broad features like bridges or tails, and broad fans or shells are generally well enhanced.

- *Unsharp-masking.* This technique is appropriate for enhancing sharp features such as shells, ripples and tails in the outer parts of elliptical galaxies. When the features are faint, the radial intensity gradient of the galaxy makes them difficult to detect. This procedure consists of smoothing the image until the small-scale features disappear, and then subtracting this blurred image from the original to create a high-pass filtered image. As a result, the finer details of the morphology are enhanced. This method is not suitable for galaxy centers, but rather produces good results in the outer halos. Indeed, it is the digital equivalent of the technique applied by Malin & Carter (1983) to photographic plates in order to reveal faint shells and filaments in nearby ellipticals. More recently, Colbert et al. (2001) applied this technique to optical and NIR images of RC3 early-type galaxies, and Peng et al. (2002) did the same for optical data of Centaurus A. For our galaxies we smoothed the images using a box width between 5 and 20 pixels, depending on the size of the features and redshifts of the galaxies.

- *Smoothed galaxy subtraction.* This technique is similar to the unsharp-masking. The difference is that, in this case, we subtract a highly smoothed image (using a filter of 10-20 pixels) from an slightly smoothed one (2 pixels). This generally produces a better result than the unsharp-masking for detecting dust or jet/tails at large scales. For example,

Fabian et al. (2006) applied this technique to Chandra X-ray observations of Perseus A.

We tried the three techniques described above with all the galaxies in our sample, and present here the results for the two techniques which gave the best result in each case, i.e., that in which the features appeared most clearly. The purpose of all these image enhancement techniques is to allow us to display the faint features that we detect as clearly as possible. Representative examples of the different features we detected are shown in Figures 1 to 9. The processed images for the whole sample are shown in the electronic edition of the journal (Appendix B), and descriptions of the galaxy morphologies are given in Appendix A.

5 RESULTS

5.1 Optical Morphologies

5.1.1 Morphological Features

The morphological classification of the galaxies was done blind, with no information about any previous work on the sources, by CRA visually inspecting the GMOS-S images. The first categorization was made using the raw reduced images, and then confirmed by inspecting the enhanced images (using the three methods described in Section 4). The classified features are listed in Tables 1 and 3; note that these were all first detected in the original, rather than the enhanced images.

The classification of the various features detected in the GMOS-S images is based on that first used by H86. In this context, a *tail* corresponds to a narrow curvilinear feature with roughly radial orientation (see Figures 1 and 2); a *fan* is similar to a tail, but shorter and broader (see Figure 3); by *bridge* we mean a feature that links the radio galaxy with a companion (Figure 4); and a *shell* is a curving filamentary structure with a roughly tangential orientation to the main body of the galaxy (Figures 2, 5, and 6). *Dust lanes* are also found in some of the galaxies (e.g., Figures 1, 7 and 8), and some have *amorphous haloes* (Figure 8). By *irregular* we refer to any feature that cannot be classified as any of the previous (Figures 6 and 7). Finally, we considered *multiple nuclei* when there are two or more brightness peaks inside 9.6 kpc, following the definition employed by SH89, based on statistical studies of cluster galaxies (Hoessel 1980)⁴ and N-body simulations of interacting binary galaxies (Borne 1984). An example of a double nucleus system is shown in Figure 9. All of these features, apart, perhaps, from the dust, are very likely the result of galaxy mergers or close encounters. In Tables 1 and 3 we also reported the detection of *jets* emanating from the nuclei of a few of the galaxies. However, we do not consider such jets as genuine morphological disturbances related to galaxy interactions, since they generally coincide with synchrotron-emitting jets already detected at radio wavelengths.

Simulations have shown how spiral-spiral (S-S),

⁴ Hoessel (1980) claimed that typical cluster members are expected to experience a close encounter or merger within this radius every 10^9 years.

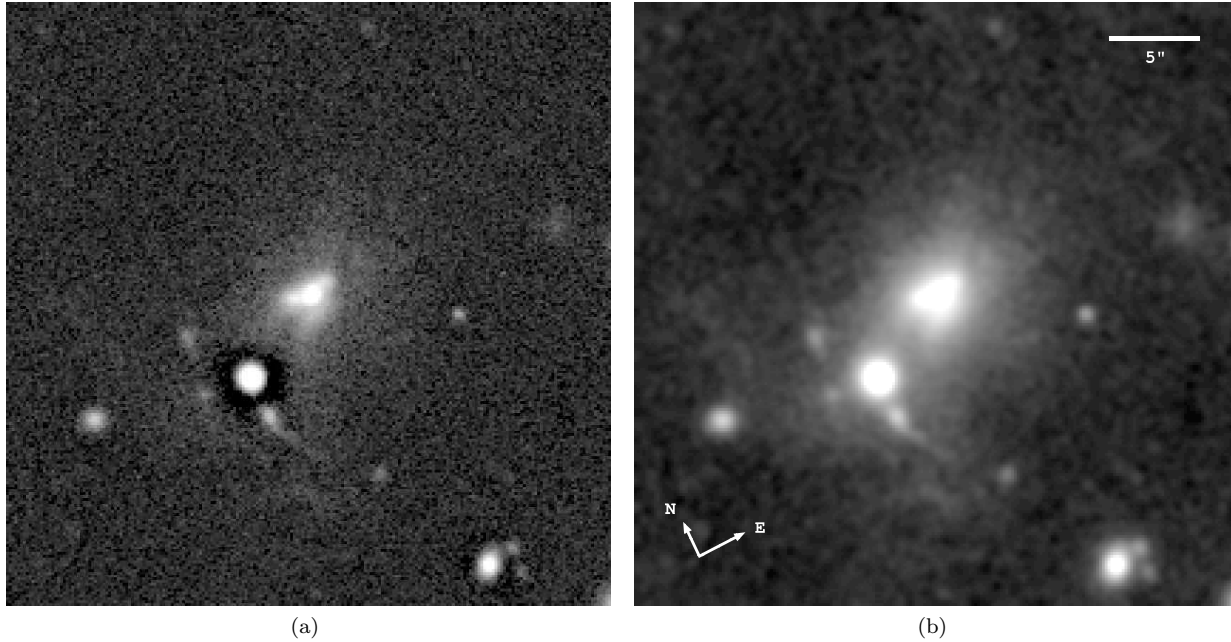


Figure 1. Example of the detection of tidal tails, a bridge, and dust in the interacting system between the WLRG PKS 0347+05 (center) and a QSO (SW of the radio galaxy). (a) Unsharp-masked image using a 10 pixel radius for the Gaussian smoothing filter. (b) Median filtered image using a 5 pixel box width. At least three tails, a bridge between the QSO and the radio galaxy, and dust are detected. (The images of all the galaxies in the sample are available in the electronic edition of the journal; Appendix B. We strongly encourage the reader to look at the electronic versions of the figures in order to clearly distinguish the detail).

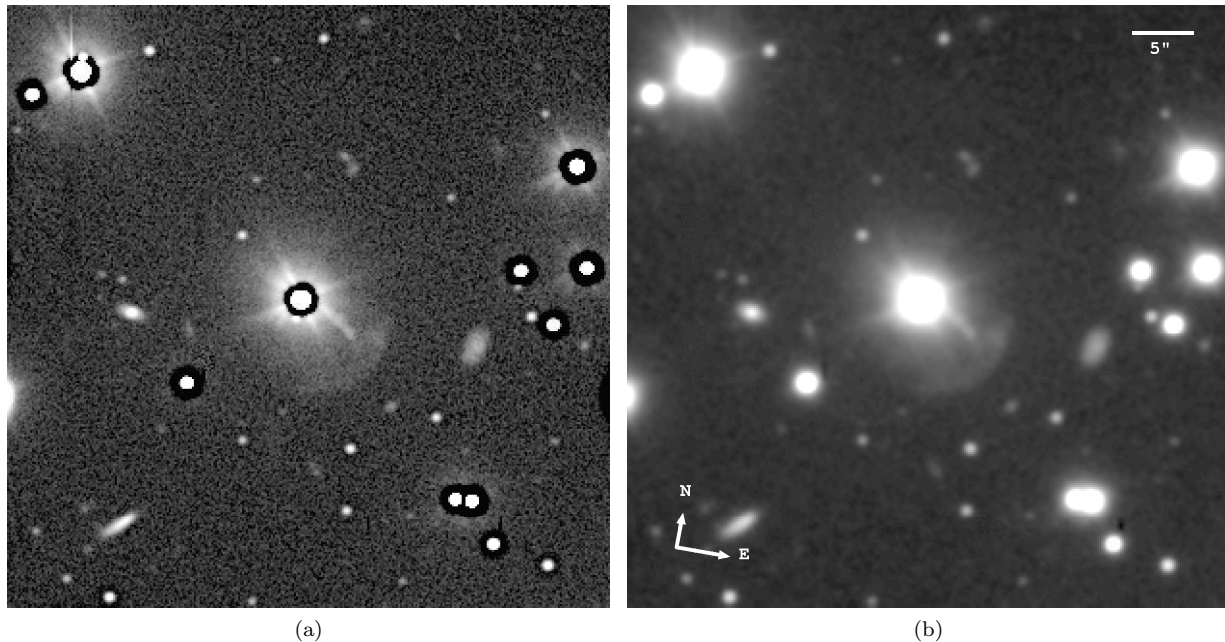


Figure 2. Illustration of the detection of a shell and a tail in the galaxy PKS 1355-41. (a) Unsharp-masked image using a moving box of 5 pixels width. (b) Median filtered image using a 5 pixel box width. A spectacular shell and a bright tail to SE of the radio galaxy nucleus are detected.

elliptical-spiral (E-S) and elliptical-elliptical (E-E) interactions can produce all of the features that form the basis of our classification (Quinn 1984; Hernquist & Spiegel 1992; Cattaneo et al. 2005; Lotz et al. 2008; Feldmann et al. 2008). To produce long and narrow morphological features such as *tails* in elliptical systems, a dynamically

cold gas supply from the companion galaxy is required (Feldmann et al. 2008). However, tidal tails can also be produced as the result of a dry-merger according to some simulations (Combes et al. 1995). The latter type of tails are broader and shorter-lived (and consequently, more diffuse) than the narrow tails produced in a gas-rich merger

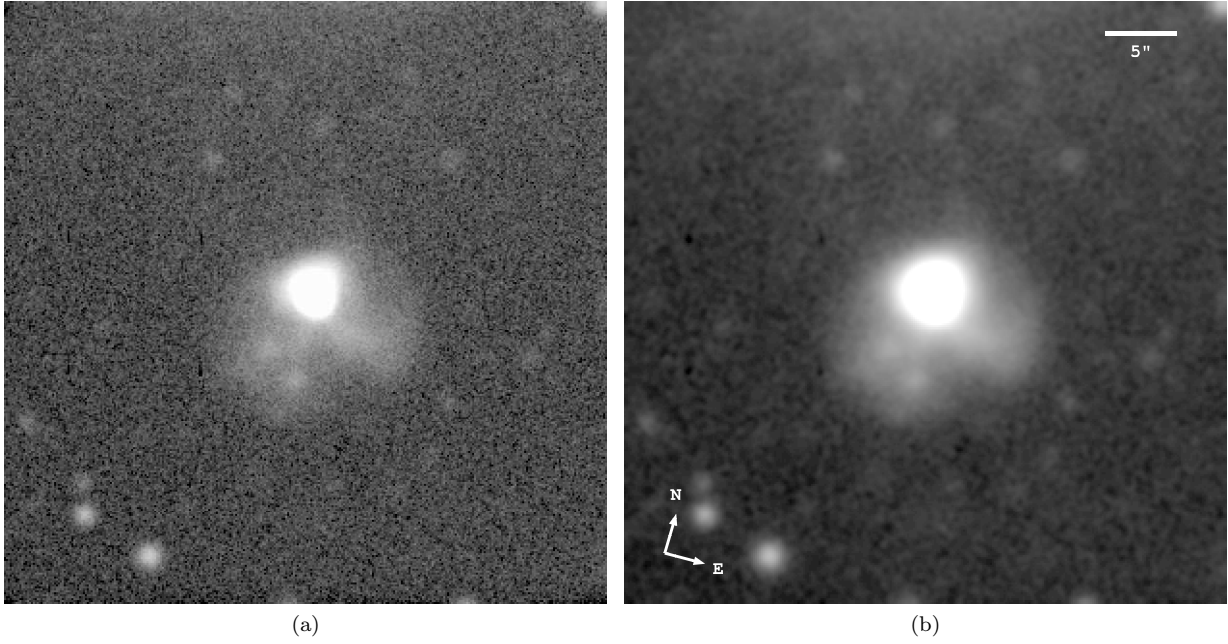


Figure 3. Example of the detection of fans and a tail in the galaxy PKS 2314+03. (a) Unsharp-masked image using a moving box width of 10 pixels. (b) Median filtered image using a 5 pixel box width. Two bright fans are clearly detected in both images, together with a faint tail pointing towards the North.

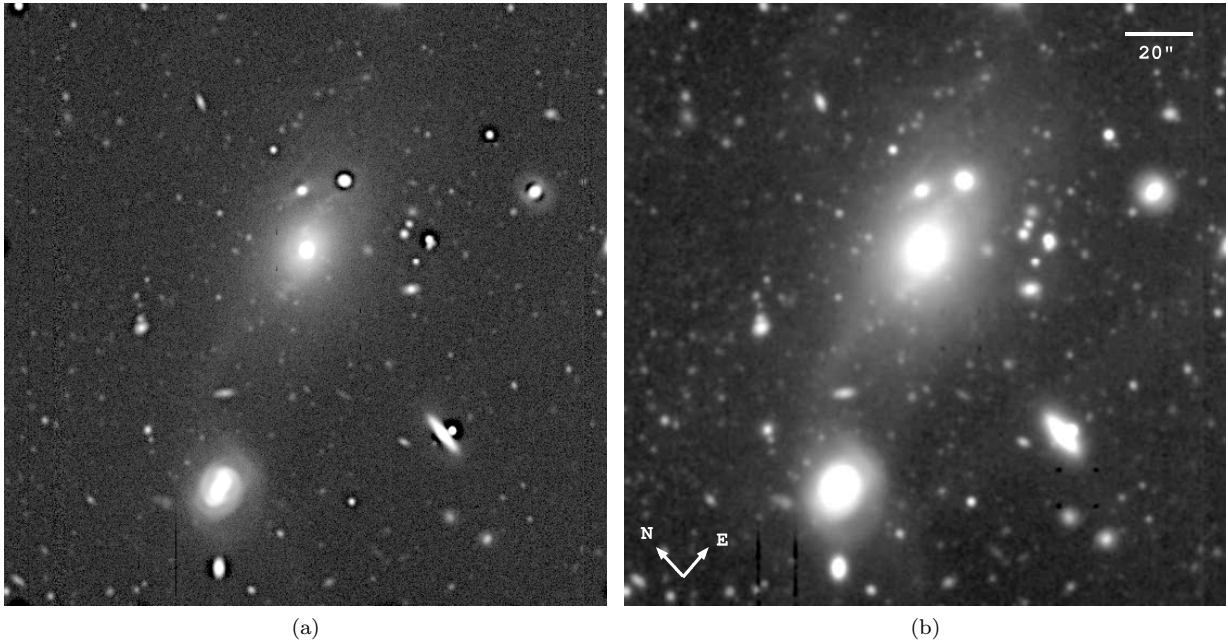


Figure 4. Illustration of the detection of bridges in the galaxy PKS 0349-27. (a) Unsharp-masked image using a moving box width of 10 pixels. (b) Median filtered image using a 5 pixel box width. Two bridges linking the radio galaxy with the large western galaxy and the small galaxy towards the East of the radio source are clearly detected. Also noticeable is the high level of distortion of the large companion galaxy.

(Naab et al. 2006; Bell et al. 2006). Broad *fans* are also quite common in interacting systems involving two elliptical galaxies (McIntosh et al. 2008) and have been reproduced in dry-merger simulations with low surface brightness (Borne 1984; Borne & Hoessel 1985). *Shells* are quite common in large ellipticals (Schweizer 1980; Malin & Carter 1983;

van Dokkum 2005; Sikkema et al. 2007; Tal et al. 2009), and are generally considered to be the result of the accretion or capture of a small disk (minor merger; Quinn 1984), although they can also be produced in major mergers (e.g., Hernquist & Spergel 1992). Simple numerical simulations are able to reproduce the observed properties of

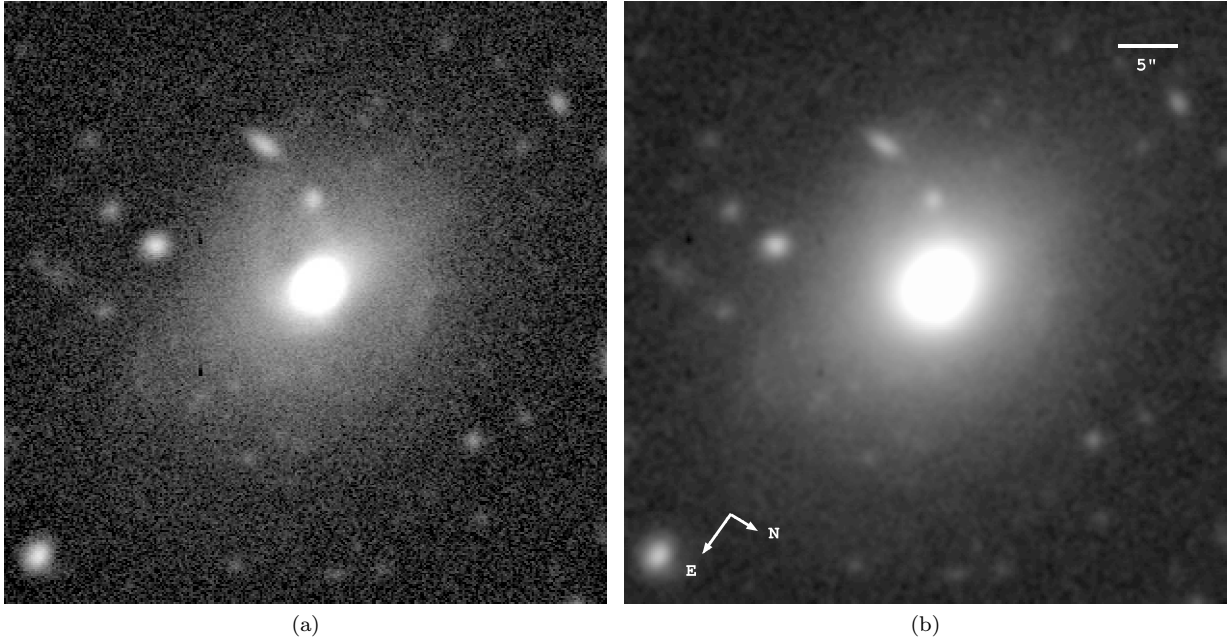


Figure 5. Example of the detection of shells and a tail in the galaxy PKS 0213-13. (a) Unsharp-masked image using a 20 pixel radius for the Gaussian smoothing filter. (b) Median filtered image using a 5 pixel box width. Two shells are detected towards East and North from the radio galaxy nucleus, respectively. A faint tail towards the SW is also revealed in the processed images.

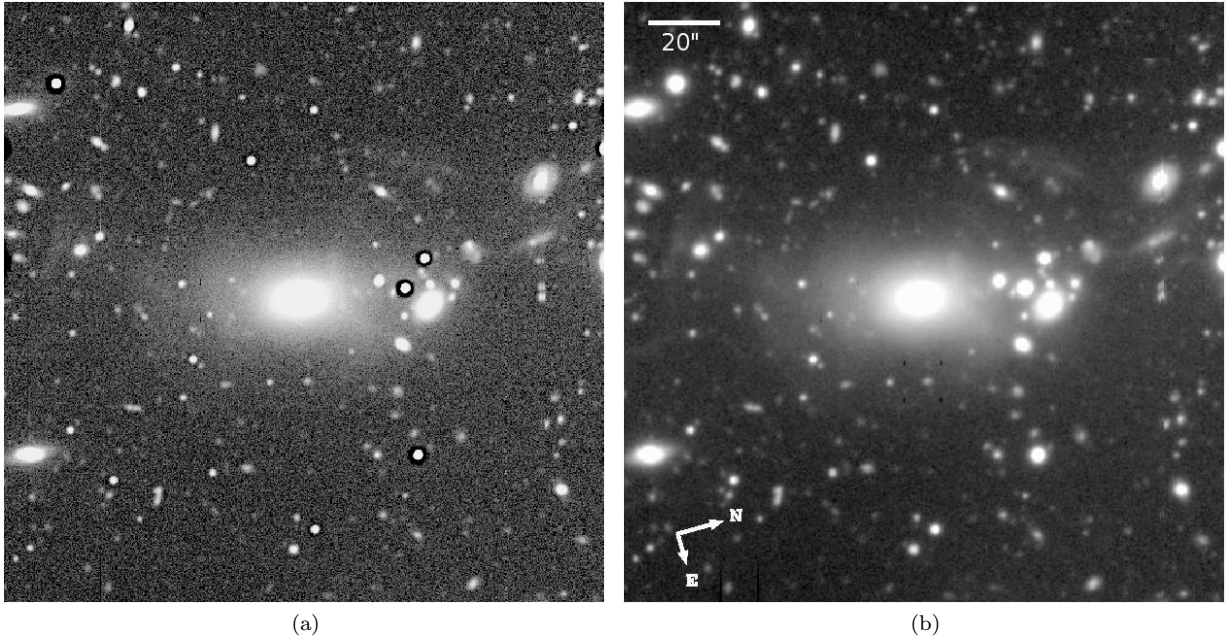


Figure 6. Illustration of the detection of shells, a fan, and irregular arc-like features in the galaxy PKS 2356-61. (a) Unsharp-masked image using a moving box width of 10 pixels. (b) Median filtered image using a 5 pixel box width. Two shells are detected close to the galaxy center, one broad fan towards the South, and at least three irregular arc-like features.

these shells (Dupraz & Combes 1986; Canalizo et al. 2007). Canalizo et al. (2007) successfully reproduced the system of shells that they found for a QSO hosted by an elliptical galaxy by simulating a minor merger as well as a major merger of two ellipticals.

Note that, in order to distinguish between the dry/wet nature of the interactions that produce features presented

here, a more quantitative and finer-grained analysis of the optical morphologies is necessary. This will be addressed in forthcoming papers. Moreover, in the future it may also be possible to tackle the dry versus wet issue by directly quantifying the cool dust and gas contents of the galaxies via their FIR emission (e.g., using combined Spitzer and Herschel observations).

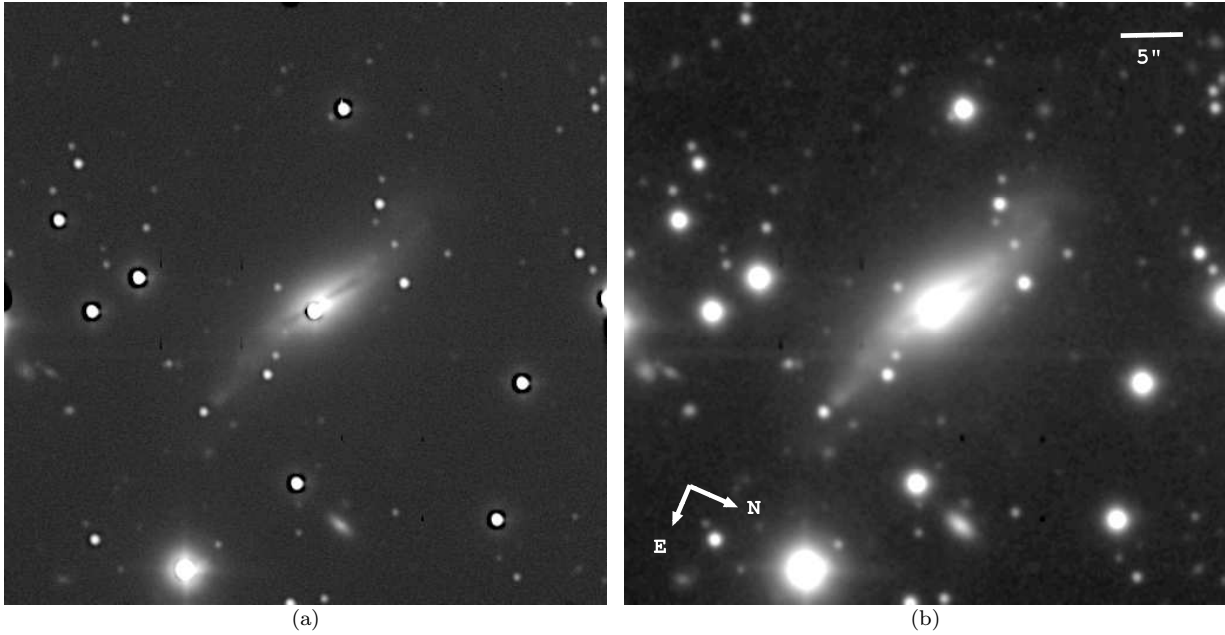


Figure 7. Illustration of the detection of dust and irregular features in the galaxy PKS 1814-63. (a) Unsharp-masked image using a moving box of 5 pixels width. (b) Median filtered image using a 5 pixel box width. A prominent dust lane crosses the galaxy center. Note also the high level of distortion in the outer disk of the galaxy, showing two irregular features in the edges.

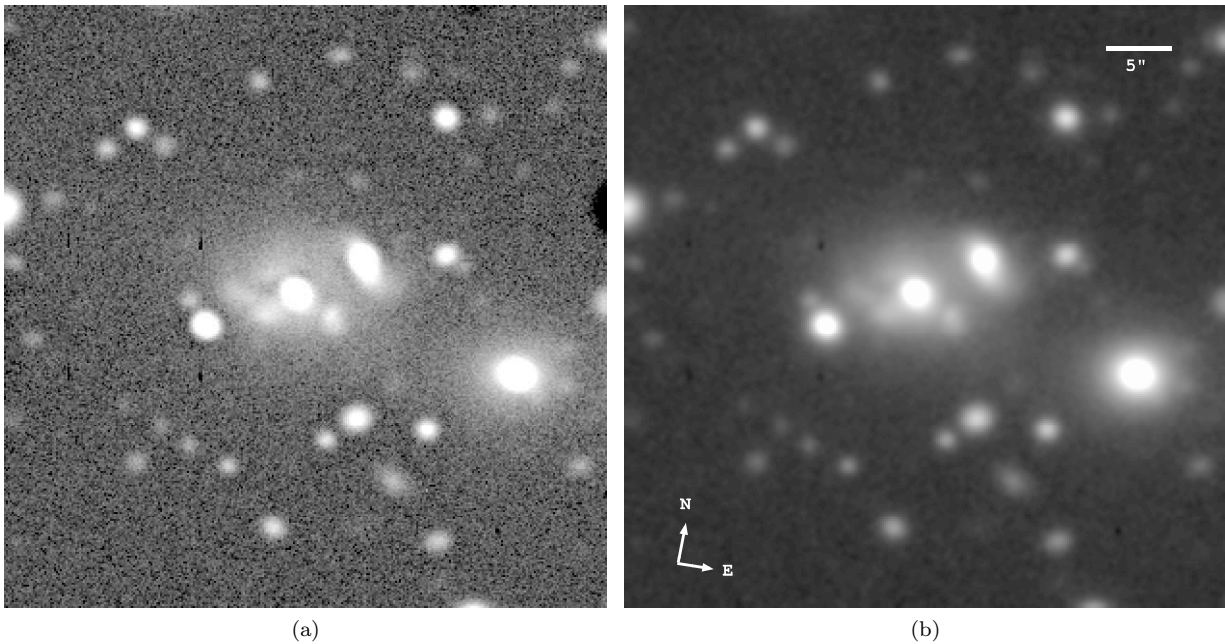


Figure 8. Example of the detection of an amorphous halo and dust in the galaxy PKS 0023-26. (a) Unsharp-masked image using a moving box of 10 pixels width. (b) Median filtered image using a 5 pixel box width. Note the amorphous halo that lies between the galaxy and its companions. Dust also seems to be present.

5.1.2 Emission-line contamination

A potentially important issue is emission-line contamination which may affect the detected features. For the low-redshift galaxies ($z < 0.065$) the $H\alpha$ emission is included in the r' -band filter, and the same happens with the $[O\ III]\lambda 5007$ Å for objects with $z > 0.14$. To confirm whether or not some of the detected features are emission-line gas, we made use of

our own published and unpublished optical long-slit spectroscopic observations (e.g., Tadhunter et al. 1993, 1998, 2002; Holt et al. 2007), published optical spectra and narrow-band images obtained by other groups, as well as of the K-band images presented in Inskip et al. (2010) for the objects in common with our sample. By comparing these data sets with our optical images we find that, if we consider the galaxies in the sample showing morphological features apart from dust

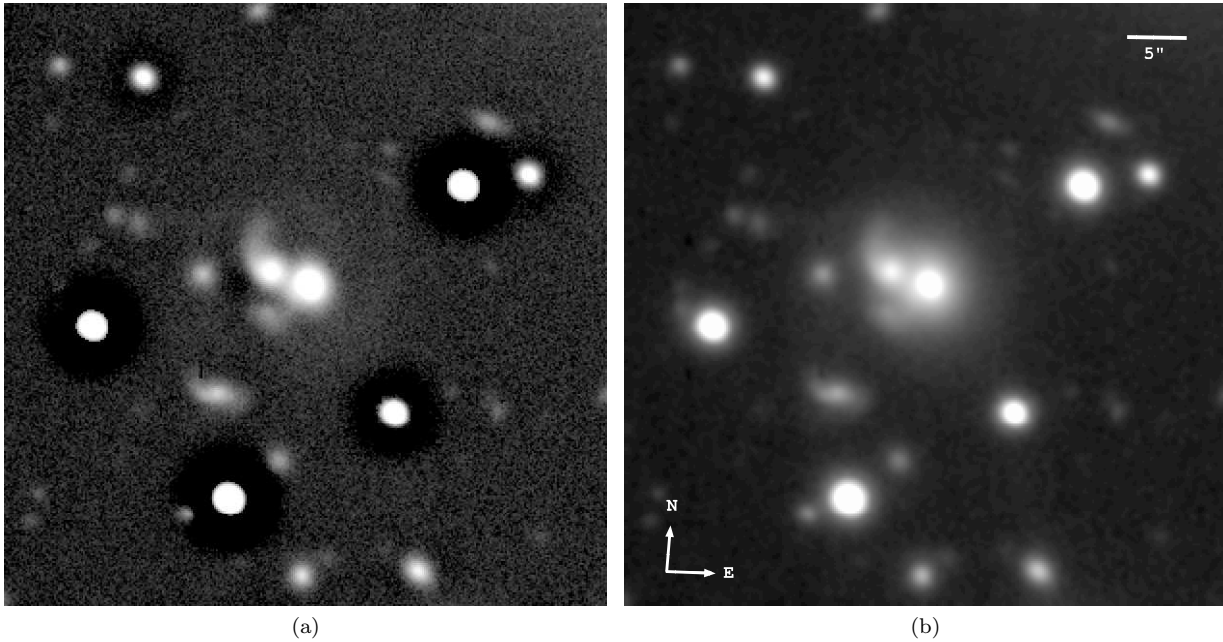


Figure 9. Example of the detection of a double nucleus and tidal tails in the galaxy PKS 1934-63. (a) Unsharp-masked image using a moving box width of 20 pixels. (b) Median filtered image using a 5 pixel box width. Two nuclei, separated by 8.9 kpc, are detected together with two tidal tails.

and jets (36 objects; 78% of the total sample), for 20/36 (56%) we can confirm either from their optical spectra or their NIR images (or both) that at least some of the peculiar features are continuum rather than emission-line features. Only for two galaxies in the sample, namely PKS 0349-27 and PKS 0235-19, do the long-slit spectra show that emission line contamination is likely to be a major issue for all the peculiar features. For the remaining 14 galaxies, there are neither optical spectra nor infrared data suitable for assessing the degree of emission line contamination. Thus, for those objects in the sample showing peculiar features for which we have sufficient data to either rule out or confirm emission line contamination (22 objects), 20 galaxies (91%) have at least some features which are continuum, rather than emission-line gas. By extrapolating this result to the whole sample, we can conclude that for the overall majority of the detected features emission line contamination is not a serious issue. See Appendix A for details on each individual object.

5.1.3 Classification

In column 5 of Table 3 we report the apparent surface brightnesses (μ_{AB}) for all the secure detections of *tails*, *fans*, *shells*, *bridges*, *amorphous haloes* and *irregular features* detected in our images. These surface brightnesses have been corrected for the sky and the diffuse host galaxy background. Using the same methodology that we used for the aperture magnitudes of the galaxies, in column 6 of Table 3 we present the μ_{AB}^{corr} values, after applying Galactic extinction and K-corrections (see Section 3). When considering surface brightness, it is also necessary to include the effect of the $(1+z)^4$ cosmological dimming. Thus, in addition to the previous corrections, we also subtract from our μ_{AB}

values the surface brightness dimming values reported in the NASA/IPAC Extragalactic Database (NED) for each galaxy, in order to estimate the depth the features would appear to have at zero redshift (see Table 3). Assuming typical colors for elliptical galaxies (Fukugita et al. 1995), we converted our μ_{AB}^{corr} measurements in both the r' and i' filters into μ_V values, in order to allow better comparison with the results of published studies. Thus, the median depth and range of surface brightness for the detected features, once corrected, are $\bar{\mu}_V = 23.6 \text{ mag arcsec}^{-2}$ and $\Delta\mu_V = [21.3, 26.2] \text{ mag arcsec}^{-2}$, respectively.

The previous transformations of surface brightnesses into V-band measurements were done by assuming K-corrections and colors of elliptical galaxies (Frei & Gunn 1994; Fukugita et al. 1995). However, some of the features (e.g., shells) may be produced in mergers involving small disk galaxies. In this case, the color of the shell would likely be similar to that of a spiral galaxy. In order to assess the importance of this effect we re-calculated the μ_V values for the detected features using K-corrections and colors of Sbc-type spiral galaxies from Frei & Gunn (1994) and Fukugita et al. (1995), and found that they do not change significantly ($\bar{\mu}_V = 23.7 \text{ mag arcsec}^{-2}$ and $\Delta\mu_V = [21.3, 26.3] \text{ mag arcsec}^{-2}$ using Sbc colors and K-corrections).

Considering only the secure identifications of morphological features⁵, the sample can be divided into five groups:

(1) *Galaxy pair or group in tidal interaction.* Galaxy pairs showing bridges (e.g., PKS 0349-27), or co-aligned distorted

⁵ For some of the galaxies, we also report in Table 3 the existence of features whose identification is not completely secure, or which are only detected in the processed images.

PKS ID	Filter	Dimming	Morphology	μ_{AB} (mag arcsec ⁻²)	μ_{AB}^{corr} (mag arcsec ⁻²)
0620-52	r'	0.218
0625-53	r'	0.229	B	22.81	22.26
0915-11	r'	0.236	D
0625-35	r'	0.232	J
2221-02	r'	0.232	F,S	25.23, 24.93	24.71, 24.41
1949+02	r'	0.246	S,D	23.03	22.21
1954-55	r'	0.244
1814-63	r'	0.264	2I,D	24.29, 24.52	23.72, 23.95
0349-27	r'	0.275	2B,[S]	26.19, 25.13	25.81, 24.75
0034-01	r'	0.303	J
0945+07	r'	0.362	S	24.03	23.49
0404+03	r'	0.369	[S]
2356-61	r'	0.397	2S,F,I	25.30, 25.75, 26.03, 25.13	24.75, 25.20, 25.48, 24.58
1733-56	r'	0.408	2T,2I,2S,[D]	24.07, 24.00, 24.40, 24.02, 24.45, 24.86	23.28, 23.21, 23.61, 23.23, 23.66, 24.07
1559+02	r'	0.434	2S,D,[2N]	23.61, 24.07	22.81, 23.27
0806-10	r'	0.453	F,2S	23.88, 23.78, 25.07	23.07, 22.97, 24.26
1839-48	r'	0.456	2N,S,[T]	22.52	21.75
0043-42	r'	0.474	[2N],[B]
0213-13	r'	0.593	2S,[T]	25.56, 25.18	24.74, 24.36
0442-28	r'	0.595	S	26.23	25.37
2211-17	r'	0.614	D,[F]
1648+05	r'	0.622	D
1934-63	r'	0.729	2N,2T	24.21, 23.90	23.03, 22.72
0038+09	r'	0.744	T	27.27	25.88
2135-14	r'	0.789	T,S,A,[B]	25.05, 24.35, 23.41	23.88, 23.18, 22.24
0035-02	r'	0.858	B,F,[S]	25.78, 25.96	24.59, 24.77
2314+03	r'	0.859	2F,[T]	24.50, 24.22	23.20, 22.92
1932-46	r'	0.900	2F,A,I	24.52, 24.57, 24.26, 25.19	23.19, 23.24, 22.93, 23.86
1151-34	r'	1.001	F,[S]	25.95	24.40
0859-25	r'	1.159	2N
2250-41	i'	1.170	2B,[T],[F]	25.62, 25.53	24.19, 24.10
1355-41	r'	1.185	S,T	24.32, 23.61	22.48, 21.77
0023-26	r'	1.209	A,[D]	24.35	22.66
0347+05	r'	1.266	B,3T,D	25.46, 24.30, 25.92, 26.39	22.98, 21.82, 23.44, 23.91
0039-44	r'	1.288	2N,3S,[T],[D]	24.72, 24.77, 25.53	22.93, 22.98, 23.74
0105-16	i'	1.458	B	25.64	23.82
1938-15	i'	1.618	F	24.85	22.40
1602+01	i'	1.651	F,S,[J]	22.82, 24.75	20.55, 22.48
1306-09	i'	1.659	2N,S	25.83	23.71
1547-79	i'	1.712	2N,T	26.03	23.52
1136-13	i'	1.929	T,J	24.26	21.78
0117-15	i'	1.942	3N,S,I,[D]	22.99, 26.83	20.51, 24.35
0252-71	i'	1.953	[A]
0235-19	i'	2.093	2T,[B]	24.38, 24.22	21.62, 21.46
2135-20	i'	2.133	F	25.52	22.68
0409-75	i'	2.287	2N

Table 3. Surface brightness measurements. Columns 1, 2, and 3 give the PKS ID, GMOS-S filter, and surface brightness dimming from the NED (magnitude per unit area). Column 4 lists our morphological classification on the basis of the detected features (same as in Table 1). Apparent and corrected (including galactic extinction, K-correction and dimming) surface brightness for secure identifications of T, F, S, B, A and I are given in columns 5 and 6, respectively. Brackets in column 4 indicate either uncertain identification of the feature, or detection in the processed images only. We do not report surface brightness measurements for the latter features.

structures (e.g., PKS 2221-02). 20% of the 2Jy PRGs are including in this category.

(2) *Galaxies presenting any sign of morphological disruption.* Galaxies showing shells, fans, tails, amorphous haloes, and irregular features. 54% of the sample show such features.

(3) *Multiple nuclei.* Galaxies with a companion lying inside a 9.6 kpc radius (17% of the sample), according to the theoretical definition employed by Hoessel (1980) and SH89.

(4) *Dust features.* Galaxies presenting dust features as the only sign of disturbance (7%).

(5) *Isolated galaxies with no sign of interaction.* Objects in which we cannot confidently identify morphological peculiarities (15%).

Note that these categories are not exclusive because some galaxies show more than one of the morphological features described above (see Table 1). Initially we considered objects in groups 1, 2, 3, and 4 as showing disturbed morphologies consistent with them having been involved in a galaxy interaction/merger, whilst galaxies classified in the fifth group were classified as undisturbed. Based on this

classification, 85% of the sample are very likely interacting objects or the result of a past merger event. Three of the galaxies included in this 85%, namely PKS 0915-11, PKS 2211-17 and PKS 1648+05, present dust features as the only detected sign of disturbance (see Table 1). It is worth noticing that all the three of these sources are WLRGs (see Section 5.2). However, *dust* features by themselves may not necessarily be a sign of galaxy interactions. If we do not consider dust as a sign of morphological disturbance related to mergers and interactions, then the percentage of galaxies in the full sample presenting evidence for interactions/mergers is 78%. Note that, while small-scale dust is often taken as an observational signature for recent mergers (e.g., van Dokkum & Franx 1995), it may also be associated with cooling flows in cluster galaxies (e.g., Fabian et al. 1994; Hansen et al. 1995; Edge et al. 1999, 2010).

On the other hand, we also note that the two SLRGs classified in group 5, namely PKS 0404+03 and PKS 0252-71, are very likely undergoing an interaction/merger, based on their morphologies. In the case of PKS 0404+03 our processed images reveal hints of a shell towards NE, but the presence of a bright star close to the radio galaxy, and high dust extinction ($A_V > 1$ mag) that affects this area of the sky, prevent us from making any secure classification. The galaxy PKS 0252-71 appears to be surrounded by a distorted halo which points towards a faint companion galaxy at ~ 33 kpc towards the South, indicating a possible interaction. Unfortunately, the relatively poor seeing for the image of this object (FWHM=1'') prevents us from confidently classifying it as disturbed. Thus, it is likely that all the SLRGs in our sample are interacting objects presenting morphological peculiarities.

5.1.4 Sample Morphologies

The main result of this work is that 85% (78% if we do not consider galaxies with dust features only) of our sample of PRGs show peculiar optical morphologies at relatively high levels of surface brightness ($\bar{\mu}_V = 23.6$ mag arcsec $^{-2}$ and $\Delta\mu_V = [21.3, 26.2]$ mag arcsec $^{-2}$). This fraction of distorted morphologies is much higher than that found for radio quiet ellipticals at the same brightness level, as we will discuss in Section 6.1. It is also greater than the fraction presented in the literature for nearby PRGs (H86, SH89, Dunlop et al. 2003).

In order to track any changes with redshift/radio power, and also to avoid any problems caused by the variation in effective spatial resolution and limiting surface brightness with redshift, the sample can be divided into three redshift ranges for the analysis: $0.05 < z < 0.11$ (15 objects); $0.11 \leq z < 0.31$ (15 objects); and $0.31 \leq z < 0.7$ (16 objects). Across each of these ranges the effective spatial scale (kpc arcsec $^{-1}$) and limiting monochromatic luminosity surface brightness vary by less than a factor of two. Considering these three ranges of redshift (Δz_1 , Δz_2 , and Δz_3 from lower to higher z), the percentages of morphological disturbance for each subset are 67% for the galaxies within Δz_1 , 93% for those in Δz_2 , and 94% considering sources in Δz_3 (60%, 80%, and 94% respectively if we do not consider dust as a sign of disturbance). Indeed, there are only two galaxies in the higher redshift range ($\Delta z_2 + \Delta z_3$) showing no clear sign of interaction (PKS 0043-42 and PKS 0252-71), indi-

cating a higher proportion of interacting galaxies at higher redshifts/radio powers.

However, it is important to note that four of the five undisturbed galaxies within Δz_1 are WLRGs, which have been proposed to be powered by hot gas accretion instead of the typical AGN cold gas accretion (see Section 5.2 for a more detailed explanation). Thus, the apparently lower percentage of interacting galaxies at low redshift could be due to the higher number of WLRGs in Δz_1 subsample. The percentages of morphological disturbance found for the total sample, the SLRGs and the WLRGs in each redshift bin are given in Table 4.

The morphological features detected in our sample of PRGs are very likely the result of galaxy mergers/interactions. In terms of the merger scenario, it is interesting that we appear to be observing many of the systems *before* the final coalescence of the nuclei of the merging galaxies. The galaxies classified in groups 1 (*galaxy pair or group in tidal interaction*) and 3 (*multiple nuclei*) would correspond to systems observed before the nuclei have coalesced, whereas those in group 2 (*galaxies presenting any sign of disturbance*), and possibly in 4 (*dust features*), would correspond to more evolved systems (coalescence or post-coalescence). By considering only galaxies in groups 1 and 3, we find that 35% of the sample are clearly pre-coalescence systems, presenting bridges with close companions (e.g., PKS 0625-53, PKS 0349-27, PKS 0035-02, and PKS 2250-41), co-aligned distorted structures (e.g., PKS 2221-02, PKS 1934-63, and PKS 1151-34) and multiple nuclei (PKS 1306-09, PKS 1547-79, and PKS 0409-75). This percentage increases up to 41% if we consider the galaxies with tentative detections of bridges linking the radio source host with companion galaxies (PKS 0043-42, PKS 2135-14, and PKS 0235-19). In the case of PKS 0043-42, the bridge also appears to be detected in the K-band image presented in Inskip et al. (2010), and for the other two, the bridges are relatively clear in the median-filtered images, but not in the original reduced frames.

Thus, the results for more than one-third of the sample are consistent with the systems being observed after the first peri-center passage but before the final coalescence of the merging nuclei. It is clear that, if radio galaxies are indeed triggered in galaxy mergers, they are not triggered at a unique phase of the merger (e.g., as the nuclei coalesce). Moreover, since we do not know the relative velocities of the galaxies, it is not possible to rule out the idea that the activity in some systems has been triggered in galaxy encounters that will not eventually lead to a merger.

5.2 Comparison between Weak- and Strong-Line Radio Galaxies.

5.2.1 Optical Morphologies

As we described in Section 2, according to the spectroscopic classification 24% of the sample of PRGs presented here are WLRGs, 43% are NLRGs, and 33% are BLRGs or QSOs (see Table 1). In order to compare them in terms of their morphologies, we define the Strong-Line Radio Galaxies (SLRGs) to include NLRGs, BLRGs, and QSOs. Thus, we have 76% of SLRGs versus 24% of WLRGs, also known in the literature as High- and Low-excitation radio Galaxies

Redshift bin	Range	Total Sample		SLRGs		WLRGs	
		Galaxies	Disturbed	Galaxies	Disturbed	Galaxies	Disturbed
Δz_1	$0.05 < z < 0.11$	15	67% (60%)	9	89% (89%)	6	33% (17%)
Δz_2	$0.11 \leq z < 0.31$	15	93% (80%)	11	100% (100%)	4	75% (25%)
Δz_3	$0.31 \leq z < 0.7$	16	94% (94%)	15	93% (93%)	1	100% (100%)

Table 4. Division of all the galaxies in the sample, SLRGs, and WLRGs in the three redshift ranges considered. The number of galaxies in a given redshift bin and the fraction of distorted morphologies found (i.e., objects classified in groups 1, 2, 3, and 4) are given for each group. Percentages given within parenthesis exclude objects with dust as the only identified feature (group 4).

(HEGs and LEGs, respectively; see Buttiglione et al. 2010 and references therein).

Considering the radio morphologies of our PRGs, only 13% of the sample are FRI sources (six objects), and all of them are WLRGs according to their optical spectra (see Table 1). In contrast, while all the SLRGs in the sample are associated with FR II radio morphologies (or alternatively CSS/GPS), some FR II sources are, in fact, WLRGs (PKS 0034-01, PKS 0043-42, PKS 2211-17, and PKS 0347+05).

The optical spectra of WLRGs are dominated by the stellar continua of the host galaxies; they are defined by a small [O III] λ 5007 Å equivalent width ($EW_{[OIII]} < 10$ Å; Tadhunter et al. 1998). These objects also show a low ionization state, as indicated by their [O II] λ 3727/[O III] λ 5007 ratios (see also Buttiglione et al. 2010). By definition, strong emission lines are detected in the optical spectra of SLRGs, but not in WLRGs. Previous studies failed to explain the differences between WLRGs and SLRGs as due to different or time-varying accretion rates (Ghisellini & Celotti 2001). An alternative interpretation (see Buttiglione et al. 2010 and references therein) is that SLRGs are powered by cold gas accretion (e.g., provided by a recent merger), with the cold gas flowing to the central region of the AGN, while WLRGs are fuelled by accretion of hot gas provided by the reservoir of their X-ray gaseous coronae (Allen et al. 2006; Best et al. 2006; Hardcastle et al. 2007; Balmaverde et al. 2008). The high temperature of this hot gas would prevent the formation of the “cold” structures (e.g., the Broad-Line Region and the torus). This hypothesis would explain the non-detection of broad lines in the vast majority of WLRGs, and also their X-ray properties. Therefore, it is interesting to compare the optical morphologies of the two types of radio galaxies, in order to check whether or not the percentage of mergers/interactions is higher in SLRGs than in WLRGs.

Despite the fact that, in our sample of PRGs, there are only 11 WLRGs versus 35 SLRGs, we can investigate possible differences in their optical morphologies. Out of the 11 WLRGs, 6 show morphological peculiarities in our optical images (55%), in contrast to the SLRGs, for which all but two (94%) show such peculiarities.

As we discussed at the end of Section 5.1.3, three of the galaxies in the sample, namely PKS 0915-11, PKS 2211-17 and PKS 1648+05, are found to present dust features as the only detected sign of disturbance, and all the three are WLRGs. If we do not consider dust as a morphological feature, then the percentage of WLRGs which show signs of morphological disturbance decreases to 27% (3 galaxies), whilst for SLRGs it remains the same (94%). It is worth mentioning that all the WLRGs showing signs of interaction are pre-coalescence systems, whereas more than half of the SLRGs

(57%) are in the coalescence or post-coalescence phase of the interaction (see Table 5). In Figures 10 and 11 we show the processed images of 9 WLRGs and 9 SLRGs with redshift $z < 0.18$ (containing all-but two of the WLRGs) to visually illustrate the differences in the typical morphologies of the two radio galaxy types.

5.2.2 Triggering scenarios for WLRGs

Our result follows the similar trend of undisturbed morphologies found by SH89 for a sample of 72 PRGs. They claim that 7% and 50% of the WLRGs and SLRGs in their sample, respectively, show morphological features such as tails, fans, bridges or shells. On the other hand, based on the analysis of K-band images of a different (but strongly overlapping) subset of the 2Jy sample, Inskip et al. (2010) found that a higher proportion of disturbed WLRG hosts: 62% compared with 40% for the SLRGs. Given the small number statistics, the rate of morphological disturbance for the WLRGs is consistent between the optical and NIR studies, and the major difference lies in the much lower rate of interaction detected in the NIR observations of the SLRGs than in our optical observations of the same objects. The latter is to be expected, since the optical observations are more sensitive to subtle, low-surface-brightness signs of galaxy interactions than the NIR observations. Moreover, the SLRGs are at higher redshifts on average than the WLRGs, decreasing the likelihood of morphological disturbances being detected for the higher-redshift SLRGs in the K-band.

For those WLRGs which do not display any of the tidal features reported in Table 1, we speculate on two possible scenarios which could explain the lack of any sign of past interactions. On the one hand, they could be fuelled by accretion of hot gas from their X-ray coronae (i.e., Bondi accretion; see e.g. Allen et al. 2006). In this case, a hot rather than cold gas supply would trigger the AGN/radio activity, and consequently, no interaction signatures would necessarily be present. On the other hand, it is also possible that these PRGs were triggered in dry-mergers or gas-poor interactions. In this scenario, broad tails or fans can be produced as result of the interaction (e.g., Naab et al. 2006; Bell et al. 2006), but without cold and young gas component, these are expected to be more diffuse and shorter-lived (~ 150 Myr; Bell et al. 2006) than those seen in mergers involving at least one late-type (gas-rich) galaxy (see Section 5.1.1). Indeed, by analysing a large sample of early-type galaxy pairs with SDSS spectra, Rogers et al. (2009) claimed that even in the absence of visual signs of disturbance, it is possible to detect the effects of a close pair interaction from the activity of the AGN as shown by the spectra of elliptical galaxies. Thus,

Morphology	Group	Total Sample	SLRGs	WLRGs	Starbursts	Non-starbursts
Pre-coalescence	1,3	35%	37%	27%	38%	33%
Coalescence or post-coalescence	2*	43%	57%	0	46%	43%
No sign of interaction	4,5	22%	6%	73%	16%	24%

Table 5. Classification of all the galaxies in the sample, SLRGs, WLRGs, starburst, and non-starburst galaxies based on the detected features. Sources belonging to groups 1 and 3 are considered as pre-coalescence systems, those in group 2 are likely coalescence or post-coalescence scenarios, and finally, galaxies classified in groups 4 and 5 do not show signs of interaction. * Those galaxies classified as (2,3) in Table 1 (the WLRG PKS 1839-48 and the SLRGs PKS 0039-44, PKS 1306-09, PKS 1547-79, and PKS 0117-15) are considered as pre-coalescence systems here, although they belong to group 2 as well.

it is possible to trigger the activity in interactions involving early-type galaxies that involve relatively small quantities of warm/cold gas. This is clearly the case for the WLRG PKS 0625-53, which in our GMOS-S image appears to be interacting with an early-type galaxy companion at 18.6 kpc. Both the accretion of hot gas and the gas-poor interaction scenarios could explain the non-detection of tidal features in the WLRGs in our sample for which they are absent (73%), whereas for the 6% of SLRGs showing no morphological peculiarities, the second scenario would be the more probable, since accretion of hot gas cannot explain the SLRG spectra.

5.3 Starburst vs non-starburst radio galaxies.

In terms of the merger hypothesis for the triggering of AGN activity, hydrodynamic simulations predict that, if the triggering mergers are both major and gas-rich, merger-induced star formation activity will occur in two main phases: around the first peri-centre passage of the merging nuclei, and close to the final coalescence of nuclei (e.g., Mihos & Hernquist 1996; Barnes & Hernquist 1996; Springel et al. 2005; Cox et al. 2006; Di Matteo et al. 2007). The relative importance of these two phases, and the time lag between them, depends on the details of the models.

Strong observational support for the general idea that gas-rich mergers trigger substantial star formation activity is provided the fact that the overwhelming majority of ultra luminous infrared galaxies (ULIRGs) – representing the most luminous star forming galaxies in the local Universe – show signs of severe morphological disturbance consistent with them having undergone major mergers (Sanders & Mirabel 1996; Veilleux et al. 2002). Moreover, analysis of the stellar populations of nearby ULIRGs provides strong evidence that we are observing most of them within ~ 100 Myr the final coalescence of the merging nuclei in major, gas-rich mergers (Rodríguez Zaurín et al. 2009, 2010).

In this context it is interesting that we find evidence for significant recent star formation activity – based both on optical and MIR/FIR data – in only 28% of the 2Jy sample of radio galaxies considered in this paper, and only two objects in the sample (4%) are sufficiently luminous at infrared wavelengths to be classified as ULIRGs. These results immediately imply that most radio galaxies are not triggered in the final coalescence phase of major galaxy mergers that are also gas-rich. Note, however, that other phases of such mergers, or different types of galaxy interactions (e.g. more minor and/or less gas-rich mergers) are not ruled out as triggers for the AGN activity, based on the evidence of the stellar populations alone (see Tadhunter et al. 2010 and

references therein). Indeed, as we saw in the previous sections, a large fraction of 2Jy radio galaxies in fact show morphological evidence that they are/have been involved in recent galaxy interactions. The question then arises: is there any evidence for morphological differences between the starburst and non-starburst radio galaxies which might suggest that the two groups have been triggered in different types of galaxy interactions, or at different phases of the same type of interaction?

First, if we simply consider the rates of morphological disturbance in the two sub-samples, we find no significant differences: 92% of the starburst radio galaxies and 82% of the non-starburst radio galaxies appear morphologically disturbed. Excluding objects in which dust features are the only sign of morphological disturbance, or excluding WLRGs, makes little difference to this comparison. Second, looking at the surface brightnesses of the detected features, we again fail to find any significant differences: the median and range of surface brightness of the morphological features in the starburst radio galaxies ($\bar{\mu}_V = 23.6 \text{ mag arcsec}^{-2}$ and $\Delta\mu_V = [22.2, 25.0] \text{ mag arcsec}^{-2}$ respectively) are both similar to those of the non-starburst galaxies. In contrast, if starburst radio galaxies were triggered in more major or more gas-rich mergers than non-starburst radio galaxies, we might expect them to show higher surface brightness features, because of the larger stellar masses in the infalling galaxies, and the potential for merger-induced star formation.

Looking at the classification of the galaxies in more detail we find no significant differences between the rate of disturbance measured for starburst and non-starburst radio galaxies, at least at the crude level of the five major morphological classes considered here (two last columns of Table 5).

However, on a more detailed level we find that, whereas shells are the most commonly detected feature in the 2Jy sample as a whole, and are detected in 15 out of 33 (45%) of the non-starburst systems, they are found in only 1 out of 13 (8%) of the starburst systems. If shells are predominantly associated with minor mergers (e.g., Quinn 1984; Dupraz & Combes 1986), then these results suggest that the non-starburst radio galaxies are more likely to be associated with minor mergers than their starburst counterparts. This in turn would be consistent with the lack of evidence for recent star formation activity in the former group.

We emphasise that the lack of greater evidence for differences between the morphologies of starburst and non-starburst radio galaxies may be partly a consequence of our relatively crude classification scheme and small sample size;

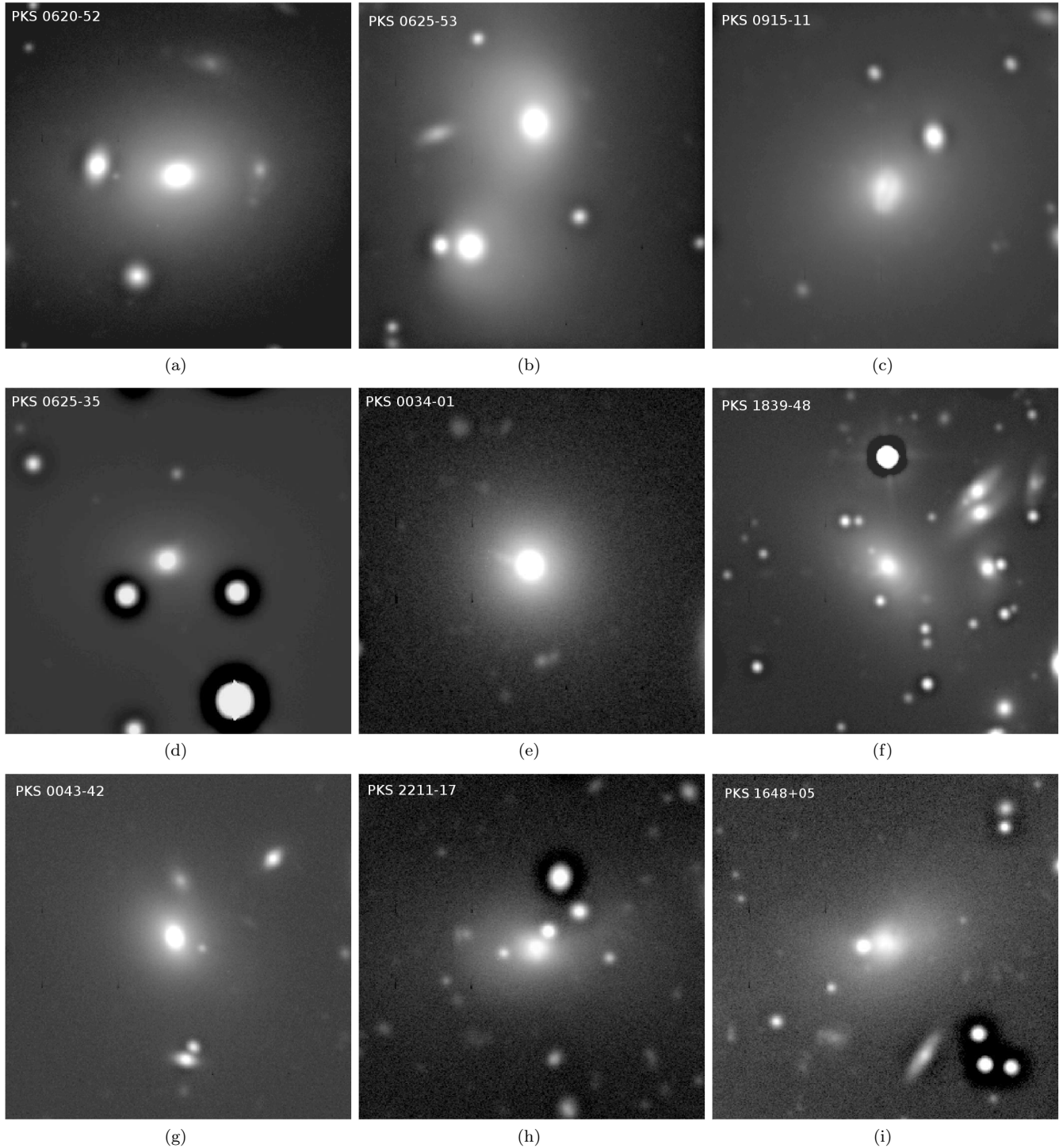


Figure 10. Processed images of 45×45 arcsec² size of the nine WLRGs in the sample with redshift $z < 0.18$ (we excluded PKS 1954-55 because of the bright foreground, star in front of the galaxy). Only two out of the nine WLRGs shown here present signs of interaction, versus eleven out to the twelve SLRGs at $z < 0.18$. Considering the sample as a whole, the percentages of interacting objects are 27% for WLRGs and 94% for SLRGs.

more quantitative morphological analysis with a larger sample may in the future uncover larger differences.

Overall, the diversity of morphologies observed in the starburst radio galaxies (and indeed the 2Jy sample as a whole) suggests that they are not solely triggered at a single stage of a particular type of galaxy interaction. This

ties in with recent analysis of the ages of the young stellar populations detected at optical wavelengths in starburst radio galaxies (Tadhunter et al. 2005; Wills et al. 2008; Tadhunter et al. 2010), which suggests that, while some ULIRG-like systems (e.g., PKS 2135-20 and PKS 2314+03) are almost certainly triggered close (< 100 Myr) to the peaks

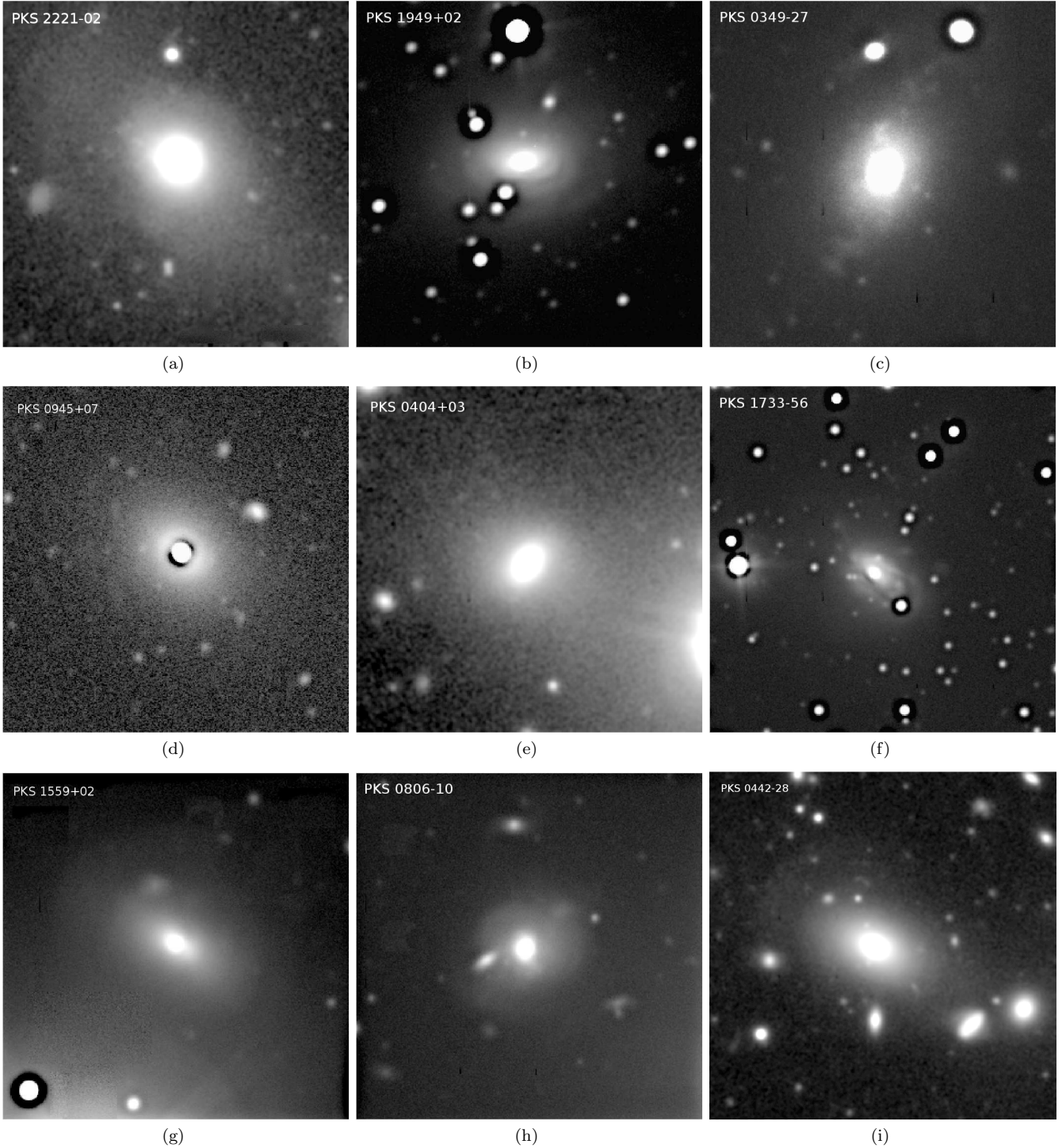


Figure 11. Same as Figure 10 but for nine of the SLRGs with $z < 0.18$ (the box size for PKS 0442-28 is 60×60 arcsec²). There are three more SLRGs with $z < 0.18$ (PKS 1814-63, PKS 2356-61, and PKS 0213-13), which are shown in Figures 5, 6, and 7.

of starburst activity in major, gas-rich mergers, others are triggered in a substantial period (>200 Myr) *after* the main merger-induced starbursts.

6 DISCUSSION

6.1 Comparison with other samples

In this Section we discuss the results found for our complete sample of PRGs in the context of published morphological studies of both radio galaxies and quiescent ellipticals. All of these comparisons are summarized in Table 6.

Work	Objects	Sample	Redshift	μ_V (mag arcsec $^{-2}$)	% features
Malin & Carter (1983)	QE	137	<0.01	$\lesssim 25.5$ -26	~ 10
Tal et al. (2009)	QE	55	<0.01	$\lesssim 27.7$	53-73
van Dokkum (2005)	QE	86	0.1	$\lesssim 28.7^*$	71
SH89	PRGs	72	<0.3	21.0-25.0	~ 50
Dunlop et al. (2003)	RG, RQQ, RLQ	33	0.2	$\lesssim 24.6^*$	**
This work	PRGs	46	0.05-0.7	23.6,(21.3-26.2)*	85

Table 6. Comparison among different morphological studies of quiescent ellipticals (QE), radio galaxies (RGs), PRGs and radio quiet and radio loud QSOs (RQQ and RLQ, respectively). The number of objects in each sample, redshift range or median redshift, median μ_V values or/and range and the percentage of galaxies with peculiar optical morphologies are given. * μ_V values obtained by assuming typical colors of elliptical galaxies from Fukugita et al. (1995) at given redshift. ** Comparable to that of QE of similar redshift and masses analyzed in the same work.

6.1.1 Comparison with other samples of radio galaxies.

Our measured percentage of morphological peculiarities (85%) is higher than the $\sim 50\%$ found by SH89 for a similar sample of PRGs at $z < 0.3$ (see Table 6). The latter authors analyzed ground-based optical images taken using telescopes ranging from 1 to 4 m and detected features at $\mu_V \lesssim 25$ mag arcsec $^{-2}$. For our PRGs, we are detecting features at a median surface brightness depth of $\bar{\mu}_V = 23.6$ mag arcsec $^{-2}$, ranging from 21.3 to 26.2 mag arcsec $^{-2}$, once cosmological dimming, galactic extinction and K-corrections are considered (see Section 5.1.3).

To investigate the reasons for the apparent discrepancy between the detection rates of morphological disturbance reported in H86, SH89 ($\sim 50\%$) and in this work (85%), we have searched for the galaxies that we have in common, and find 14 in total. We detect tidal features in all of them, whereas H86 reported signs of morphological peculiarities in the form of fans, shells, tidal tails, etc. in only six (PKS 2221-02, PKS 0349-27, PKS 0945+07, PKS 1559+02, PKS 1934-63, and PKS 2314+03). By comparing their and our detected features for the latter galaxies, in general we find good agreement for the morphologies of these six galaxies, except for PKS 0945+07. We detect a shell in the case of this galaxy, whereas H86 reported the existence of a tail and a fan, but associated with line-emitting gas (see Appendix A). For the remaining 8 objects, H86 and SH89 did not detect any features. Three of them are the three galaxies presenting dust as the only sign of disturbance in our images (PKS 0915-11, PKS 2211-17 and PKS 1648+05), and for PKS 0035-02, PKS 0213-13, PKS 1949+02, and PKS 2135-14 we detect bridges, shells, tails, fans, and amorphous haloes. The higher percentage of features that we report here is likely due to the higher quality of our GMOS-S images, taken using an 8m telescope and with good seeing conditions (median FWHM $\sim 0.8''$, in contrast with the 1-2'' range of seeing of the H86, SH89 observations), our better pixel sampling (0.146'' pixel $^{-1}$ with GMOS-S, compared with the 0.29''-1.3'' pixel sizes employed by H86, SH89), and the fact that our images go ~ 1 mag deeper.

It is also necessary to consider the results of Dunlop et al. (2003), based on a sample of 33 AGN comprising radio galaxies, radio quiet QSOs (RQQs) and radio loud QSOs (RLQs) at a median redshift of $z=0.2$. They analyzed high spatial resolution HST/WFPC2 images, and showed that all the AGN in their study appear to be hosted

by relatively undisturbed giant elliptical galaxies. Indeed, by comparing with a control sample of quiescent ellipticals in clusters, they concluded that the hosts of radio-loud and radio-quiet AGN are indistinguishable from quiescent ellipticals of similar masses and redshifts. As discussed in Section 1, we believe that the discrepancy between the results presented by Dunlop et al. (2003) and ours is mainly based on the differences in the depth of the observations. As can be seen in Table 6, the features measured by Dunlop et al. (2003) reach a limiting faintness of 24.6 mag arcsec $^{-2}$ in the V-band (assuming typical colors of elliptical galaxies), whereas in our case, we are detecting features as faint as $\mu_V = 26.2$ mag arcsec $^{-2}$, i.e., 1.6 mag fainter.

Thus, as discussed in Section 1, the discrepancy between the previous results and ours is very likely due to the differences in depth of the observations. The high-quality deep Gemini observations presented here show for the first time that the overall majority of PRGs at intermediate redshifts present disturbed morphologies, which are very like the result of galaxy mergers and/or interactions.

6.1.2 Comparison with samples of quiescent elliptical galaxies.

If galaxy interactions are the main triggering mechanism for radio-loud AGN activity in our sample, then we should expect to find the signs of morphological disturbance to be stronger in the radio source host galaxies than in the general population of quiescent (i.e. non-active) early-type galaxies. Fortunately, in the general context understanding the importance of galaxy mergers for the formation of such galaxies, a number of detailed morphological studies have been made of the quiescent elliptical galaxy population in the local Universe (Schweizer 1980; Malin & Carter 1983; van Dokkum 2005; Sikkema et al. 2007; Tal et al. 2009).

Perhaps the most relevant study – both in terms of its surface brightness depth and its general approach to morphological classification – is that by Malin & Carter (1983). They used visual inspection of deep photographic images to detect shell and ripple features in $\sim 10\%$ of nearby elliptical galaxies in the RC2 catalogue with declinations $\delta < -17^\circ$. Importantly, the limiting depth of their observations ($\mu_V \lesssim 25.5 - 26$ mag arcsec $^{-2}$) is similar to the effective depth reached by our Gemini observations of the 2Jy sample. Clearly, the rate of morphological disturbance found by Malin & Carter (1983) is significantly lower than the one

we find for the 2Jy sample, even if we only make the comparison with the lowest redshift bin (Δz_1) of our PRGs, which contains a number of relatively undisturbed WLRG objects (see section 5.2). Unfortunately, Malin & Carter (1983) give only the limiting surface brightness for their survey as a whole, so a more detailed comparison between the surface brightnesses of the detected features is not possible.

More recently, there have been two CDD-based studies of nearby elliptical galaxies that reach significantly fainter surface brightness limits. First, van Dokkum (2005) reported that 71% of a sample of 86 colour- and morphology-selected bulge-dominated early-type galaxies at a median redshift of $z = 0.1$ show morphological evidence of broad fans, tails of ripples at very faint levels of surface brightness: $\mu_V < 28.7 \text{ mag arcsec}^{-2}$ (assuming typical colours for elliptical galaxies at $z=0.1$ from Fukugita et al. 1995). A more recent study by Tal et al. (2009) has presented an analysis of the optical morphologies of a complete sample of 55 luminous and nearby elliptical galaxies ($z < 0.1$). Reaching a limiting depth of $\mu_V < 27.7 \text{ mag arcsec}^{-2}$, they detect signs of morphological disturbance in $\sim 53\text{--}73\%$ (depending on the criterion used) of their sample. Clearly, the rates of morphological disturbance detected in these recent, CDD-based studies approach those we find in the radio galaxies in the 2Jy sample. However, it is notable that their limiting surface brightnesses are much fainter than we achieve for the 2Jy radio galaxies: 2.5 and 1.5 magnitudes fainter in the cases of van Dokkum (2005) and Tal et al. (2009) respectively. Therefore it is not clear that the comparison is reasonable.

Finally we note that there are some important caveats to bear in mind when making the comparison with the existing studies of quiescent elliptical galaxies. First, an “ideal” comparison sample would be matched in galaxy mass, environment, redshift and depth/resolution of observations; clearly no such sample exists at present. Second, emission line contamination might affect the comparison. For example, any neutral gas present in quiescent elliptical galaxies that falls below the detection limits of existing HI 21cm surveys and is not visible at optical wavelengths (because it is not ionized), might be rendered visible by AGN illumination in the radio-loud AGN population.

Although none of the three comparison samples considered above is completely ideal, all show a strong overlap with the 2Jy sample in terms of the absolute magnitudes and environments of the host galaxies. Any bias would likely be in the direction that the radio galaxy hosts are more luminous than the general quiescent elliptical galaxy population covered by the comparison samples⁶. Therefore, if radio galaxies were not triggered by galaxy interactions, we would require a strong positive correlation between luminosity and degree of morphological disturbance, in order to explain the fact that the 2Jy sample displays a higher rate of disturbance than the sample considered by Malin & Carter (1983). As far as we are aware, no such correlation exists.

In terms of emission line contamination, even if we make the most pessimistic assumptions about the degree of emission line contamination (see section 5.1.2), the rate of morphological disturbance due to genuine continuum-emitting structures in the 2Jy sample still comfortably exceeds that of the Malin & Carter (1983) sample.

7 CONCLUSIONS

We have analyzed deep GMOS-S/Gemini optical broadband imaging for a complete sample of southern PRGs at intermediate redshifts ($0.05 < z < 0.7$). We visually classify their morphologies, and divide the sample into five groups, depending on the detected features. In order to confirm the detections, we made use of three different data analysis techniques with the purpose of enhancing the morphological features. Our major results are as follows:

- The high-quality observations presented here show for the first time that 85% of our sample of PRGs at intermediate redshifts present peculiar morphologies at relatively high levels of surface brightness ($\bar{\mu}_V = 23.6 \text{ mag arcsec}^{-2}$). If we do not consider dust as a sign of morphological disturbance, then 78% present peculiarities. In any case, this fraction of distorted morphologies is much higher than for radio quiet ellipticals at the same sample brightness level and also for other samples of PRGs.
- The morphological peculiarities of the galaxies include tails, fans, bridges, shells, dust lanes, irregular features, amorphous haloes, and multiple nuclei. We propose that these features are the result of the merger or close encounter of galaxies in pairs or groups.
- The results for more than one-third of the sample are consistent with the galaxies being observed after the first peri-center passage but before the final coalescence of the merging nuclei. It is clear that, if radio galaxies are indeed triggered in galaxy mergers, it does not happen at a unique phase of the merger. Moreover, since we do not know the relative velocities of the galaxies, it is not possible to rule out the idea that the activity in some galaxies has been triggered in galaxy encounters that will not eventually lead to a merger.
- By dividing the sample in WLRGs and SLRGs we find that 55% of the former show peculiarities in their optical morphologies, contrary to the SLRGs, of which at least 94% present any sign of disturbance. Indeed, the percentage of distorted WLRGs decreases down to 27% if we do not consider dust as a sign of morphological disturbance. Based on these results, the majority of WLRGs would be fuelled/triggered by Bondi accretion of hot gas. However, the evidence for interactions and dust in a fraction of them indicates that the cold-gas accretion cannot be ruled out.
- For those WLRGs which do not show any evidence of morphological disturbance, we propose two possible scenarios to explain the lack of any sign of past interactions. Either they are fuelled by Bondi accretion of hot gas from their X-ray coronae or they are the result of dry-mergers or gas-poor interactions.
- We find that 92% of the starburst radio galaxies in the sample present peculiar morphologies, following the same trend as the total and SLRG samples. There are no significant differences between the optical morphologies of star-

⁶ Whereas the radio galaxy hosts are generally hosted by giant elliptical galaxies, at the upper end of the E-galaxy luminosity function (typically $L > 2L_*$; Dunlop et al. 2003), the RC2 catalogue that forms the basis of Malin & Carter (1983) study samples down to much lower optical luminosities.

burst and non-starburst galaxies, neither in the rate of detected features, nor in their surface brightnesses. The only possible distinction between the two groups is the lower proportion of identified shells in the former.

- By comparing with different samples of quiescent ellipticals from the literature, we conclude that the percentage of morphological disturbance that we find here for PRGs greatly exceeds those found for quiescent ellipticals when similar surface brightness limits are considered.

APPENDIX A: NOTES ON INDIVIDUAL OBJECTS

Below, we comment individually on the optical morphologies of the galaxies in our sample, based on our GMOS-S images. Details on the possible emission-line contamination in the detected features are also given, based on the comparison with the K-band data presented in (Inskip et al. 2010), and with optical long-slit spectra and narrow-band images of the galaxies from various published and unpublished sources. The quoted surface brightnesses have been corrected to the rest frame V-band, as described in Section 5.1.3 of the main body of the text. All the images referred to are presented in the electronic edition of the journal (Figures B1 to B46).

A1 PKS 0620-52.

This WLRG is the closest object in our sample, and it has been found to show clear evidence for a YSP (Wills et al. 2004). Tadhunter et al. (2010) analyzed new spectra for this source, determining an upper limit of 0.9 Gyr for the age of the YSP. Our GMOS-S image (Figure B1) does not reveal any evidence for morphological disturbance, apart from a relatively high incidence of companion galaxies, as expected for a galaxy at the centre of a rich cluster. A cluster environment for this radio galaxy is further supported by the existence of a moderately-luminous X-ray halo (Siebert et al. 1996; Trussoni et al. 1999). Statistically, it is more difficult to detect tidal features such as shells or broad fans in regions of high galaxy density, since the tidal effects rapidly disrupt these features.

A2 PKS 0625-53.

This WLRG is hosted by the eastern component of a dumbbell system in a rich galaxy environment. Our Gemini image (Figure B2) shows a broad bridge linking the two galaxies, which are separated by a distance of ~ 19 kpc, have highly distorted isophotes, and are clearly interacting. The same morphology is found in the NIR images analyzed in Inskip et al. (2010), who did not detect strong nuclear point source component in either object. Also noticeable in our GMOS-S image is the degree of distortion in the two galaxy companions located to the NW of the dumbbell system in Figure B2a.

A3 PKS 0915-11 (3C218, Hydra A).

Situated in the Hydra cluster of galaxies, this FRI is one of the most powerful radio sources in the local universe. Its optical spectrum (WLRG) show weak emission lines, along

with absorption lines and a continuum SED that provide evidence for a young stellar population of age ~ 0.05 Gyr (Aretxaga et al. 2001; Wills et al. 2004; Holt et al. 2007). Our GMOS-S r' -band image (Figure B3) shows an extended diffuse halo similar to that of PKS 0620-52, which is typical of central cluster galaxies; it also reveals for the first time a dust lane of diameter 6 kpc crossing the galaxy nucleus. This dust lane appears to be aligned with the rotating disk structure detected by Melnick et al. (1997).

A4 PKS 0625-35 (OH-342).

This low-redshift WLRG does not reveal any morphological peculiarity associated with a merger or interaction in our Gemini image (Figure B4). The only feature that we detected is a one-sided jet pointing to the SE, which is also found by Inskip et al. (2010) in their residual NIR image. The detection of this jet supports the classification of this object as a BL-Lacertae (BL-Lac) by Wills et al. (2004).

A5 PKS 2221-02 (3C445).

This BLRG shows a very broad and asymmetric $H\alpha$ profile in the optical spectrum first reported by Osterbrock et al. (1975). In the NIR, its morphology appears dominated by a nuclear point source, and the host galaxy is well-reproduced by a de Vaucouleurs elliptical in both the NIR (Inskip et al. 2010) and the optical (Govoni et al. 2000). Our deep Gemini image (Figure B5) reveals the spectacular morphology of this galaxy, which is clearly interacting with a close companion that appears obviously distorted in the direction of the radio galaxy host. The separation of the radio source and the companion galaxy is ~ 37 kpc. The radio galaxy shows a broad *fan* of surface brightness $\mu_V = 25.6$ mag arcsec $^{-2}$ towards the SW that is co-aligned with the axis of the double galaxy system, and a *shell* towards the East with $\mu_V = 25.3$ mag arcsec $^{-2}$. The optical morphology of this galaxy is described in H86. They also identify the *fan*, as well as a bright tail extending out from the galaxy center for ~ 10 kpc to the SW, which they identify as a strong source of emission lines. In our median-filtered image this feature appears more like a series of blobs that curve to the SW of the nucleus. Long-slit spectra of this source (Tadhunter et al. 1986) demonstrate that the flux in the outer distorted structure is not dominated by emission lines.

A6 PKS 1949+02 (3C403).

This NLRG/FRII galaxy with an X-shaped radio morphology (Black et al. 1992) was observed in the optical with HST by Martel et al. (1999) and de Koff et al. (2000), who reported the existence of dust lanes and a low-surface brightness halo with a sharp boundary surrounding the central region at a radius of $\sim 2.5''$. Our Gemini image (Figure B6) confirm the latter feature, and, for the first time, also reveal an extraordinary series of concentric arc/shell features extending to a maximum radius of ~ 12 kpc to the West, and ~ 20 kpc to the South. The brightest of these shell features has a corrected surface brightness of $\mu_V = 22.6$ mag arcsec $^{-2}$. The K-band model-subtracted residual images presented in Inskip et al. (2010) reveal hints of

the shells, indicating their continuum-emitting nature. Our long-slit spectra confirm that the outer arc and shell features are not dominated by emission line radiation. H86 also studied the optical morphology of the galaxy, but did not report any type of disturbance.

A7 PKS 1954-55.

This WLRG/FRI galaxy is located in a rich environment. The presence of a bright star close (in projection) to the nucleus precludes detailed examination of the morphology of the central regions of the galaxy, but our Gemini image (Figure B7) shows no sign of morphological disturbance in its halo, consistent with the earlier results of Fasano et al. (1996). The galaxy belongs then to the group of WLRGs in our sample which do not present evidence for mergers/interactions.

A8 PKS 1814-63.

This NLRG/GPS has been found to show starburst activity in the MIR/FIR, based on its FIR excess and strong PAH features (Dicken et al. 2009, 2010). Our GMOS-S optical image (Figure B8), which shows a straight dust lane of diameter ~ 20 kpc along with highly elongated, disk isophotes, is consistent with the morphological classification of this system as an S0 or Sa galaxy viewed close to edge-on. However, the outer disk of the galaxy is clearly highly distorted. Due to the presence of a bright star close to the galaxy nucleus we took two different sets of images with short and long exposure time (see Table 2). The first allows us to unveil details of the nuclear region, avoiding star saturation, whereas the second longer exposure time set reveals more details of the irregular features in the outer parts of the galaxy. Similar features (a faint extended disk feature and a possible dust lane) are observed in the model-subtracted K-band image analysed by Inskip et al. (2010). Long-slit spectra of this galaxy confirm that emission line contamination is not a serious issue for the outer distorted features. This source will be the subject of a detailed study of its optical and radio properties (Holt et al. 2010).

A9 PKS 0349-27.

PKS 0349-27 shows one of the most spectacular morphologies of the sample in our GMOS-S image (Figure B9). The galaxy was studied by H86, who analysed narrow-band [O III] $\lambda 5007$ and broad V-band images. They reported the existence of two close companion galaxies at 26 and 20 kpc towards the East and NE, respectively. In their images (both narrow- and broad-band) they detected a bridge linking the radio galaxy with the eastern companion located at 26 kpc and a tail-like structure pointing to the opposite direction and extending up to 20 kpc. According to the study of the gas kinematics of this system presented by Danziger et al. (1984), these features are very likely the result of an interaction with the eastern galaxy companion, despite the fact that they are line-emitting gas features. Our deep GMOS-S image shows in much more detail the scenario of this interaction. We confirm the existence of the structures detected by H86, and measure a surface brightness for the

bridge linking the radio galaxy with the eastern companion of $\mu_V = 25.5$ mag arcsec $^{-2}$. In addition, we also detect a more extended, and fainter, bridge linking the radio galaxy with the clearly distorted galaxy at 83 kpc to the West ($\mu_V = 26.5$ mag arcsec $^{-2}$). The latter bridge feature was also detected by Hansen et al. (1987) in their deep H α + [NII] image, at a surface brightness level which suggests that much of the emission from the bridge detected in our GMOS-S image could be emission line, rather than continuum radiation. Whereas Hansen et al. (1987) classified the distorted galaxy at the end of the larger bridge as an elliptical, it is clearly revealed as a disk galaxy in our GMOS-S image. The median-filtered image also reveals the presence of a faint shell extending ~ 10 kpc to the West of the radio galaxy nucleus.

A10 PKS 0034-01 (3C15).

This WLRG has a radio morphology that is intermediate between FRI and FRII classes (Morganti et al. 1999). The only feature that we detect in our GMOS-S image of this object (Figure B10) is the optical synchrotron jet reported for the first time in Martel et al. (1998). It extends to a projected distance of 7.5 kpc ($\sim 40''$) in the NW direction. The jet is also detected in the K-band images presented in Inskip et al. (2010). WFPC2/HST images of this source reveal subarcsecond-scale features including a dust lane and three emission filaments or arms (Martel et al. 1998; Sparks et al. 2000). These latter features are not resolved in our GMOS-S image.

A11 PKS 0945+07 (3C227).

This BLRG/FRII is studied in detail by Prieto et al. (1993), who found spectacular extended emission line structures. Also, the optical morphology of this system was studied by H86, and they reported the detection of several knots and tails which very likely correspond to line-emitting gas. Our GMOS-S image (Figure B11) does not reveal any of these features, but it shows a shell of $\mu_V = 24.4$ mag arcsec $^{-2}$ ~ 7 kpc to the NW of the nucleus. In fact, emission line contamination of the shell is not a serious issue because strong emission lines do not fall in the r' filter employed in our observations. Indeed, this is confirmed by the presence of this shell in the K-band images of this galaxy (Inskip et al. 2010).

A12 PKS 0404+03 (3C105).

The presence of a very bright star close (in projection) to this NLRG/FRII, along with the high Galactic dust extinction measured for this field ($A_V > 1$), mean that our observations of this source are less sensitive to low surface brightness features than for the other objects in our sample. Nonetheless, our processed images (Figure B12) reveal hints of a faint shell towards the NE.

A13 PKS 2356-61.

The optical morphology of this NLRG, as shown in our GMOS-S image, appears to be full of features which are very

likely the result of a past merger/interaction (Figure B13). At shorter scales, we detect one arc-like irregular feature of depth $24.9 \text{ mag arcsec}^{-2}$ in the V-band at the northern side of the galaxy center. There is also a shell towards the south of the galaxy, and a fainter one to the NE ($\mu_V=25.1$ and $25.6 \text{ mag arcsec}^{-2}$ respectively). Further from the brighter shell there is also a broad fan/shell in the same direction, at a $25.8 \text{ mag arcsec}^{-2}$ depth level. Finally, at ~ 82 and 118 kpc distance from the galaxy center, there are two faint arcs towards the NW and SW, respectively. Note that the shell features detected in this galaxy are more irregular in appearance than the sharp shells detected in other objects in our sample (e.g., PKS 1559+02 and PKS 0442-28) and in the nearby ellipticals studied by Malin & Carter (1983). Emission line contamination is not a serious issue in the case of this galaxy because strong emission lines do not fall in the r' filter employed in our observations.

A14 PKS 1733-56.

This BLRG/FRII, with evidence for starburst activity provided by its FIR excess and strong PAH features in its MIR spectrum (Dicken et al. 2009, 2010), lies in a relatively crowded field. Its optical morphology, as revealed by our GMOS-S image (Figure B14), is highly disturbed, showing at least two tidal tails: a shorter one pointing to the West and a longer one to the SE both having $\mu_V=23.6 \text{ mag arcsec}^{-2}$. We also detect several arc-like irregular features, including a smooth, inner one (of $\mu_V=23.6 \text{ mag arcsec}^{-2}$) up to 6.5 kpc in the SE direction and a larger one of $\mu_V=24 \text{ mag arcsec}^{-2}$ extended up to 11.6 kpc to the NW. It is likely that at least part of the complex structure visible in the central regions of the galaxy is due to obscuration by a complex system of dust lanes. The brightest inner arc-like irregular structure is detected in the K-band, model-subtracted images presented by Inskip et al. (2010), who also claim that the residuals from the subtraction display an excess of emission aligned with the major axis of the galaxy. In the outermost part of the radio galaxy host we also detect an interlocking series of fainter shells that extent to a maximum radius of $\sim 25 \text{ kpc}$ to the SE and $\sim 17 \text{ kpc}$ to the South. We measure a surface brightness of $\mu_V=24.4$ and $24.0 \text{ mag arcsec}^{-2}$ for these outer shells, respectively. Emission line contamination is not a serious issue in our GMOS-S image, since strong emission lines do not fall in the r' -band filter used for the observations. Based on integral-field spectroscopic observations, Bryant & Hunstead (2002) found evidence for a disturbed morphology, disrupted gas rotation, and patchy starburst emission for this source. They claimed that the most plausible explanation for all of these features is an interaction or merger with a SE companion from which the radio galaxy would be accreting gas, but they did not find such a merging galaxy in the DSS-II and SuperCOSMOS images. Our deeper GMOS-S image does not show any merging candidate either.

A15 PKS 1559+02 (3C327).

The WFPC2/HST images of this NLRG/FRII source reveal a bifurcated dust lane structure extending $\sim 3 \text{ kpc}$ to the NE of the galaxy nucleus, with the radio axis lying roughly

perpendicular to the dust lanes. The nuclear structure, as revealed by the HST image, appears to be complex and possibly double (de Koff et al. 1996, 2000). The presence of a bright star close to the galaxy complicates its morphological classification. However, by looking at our processed images (*unsharp-masked* and specially *smoothed galaxy-subtracted*; Figure B15) the presence of dust lanes becomes clear. The galaxy nucleus appears double as well, but it is difficult to say whether is intrinsically double or just apparently divided by the dust lane. On larger scales the GMOS-S image reveals a system of sharply-defined shells at radii of ~ 16 and 30 kpc to the SE, and ~ 14 and 22 kpc to the NW; these sharply-defined shell features are reminiscent of the systems of shells detected around some elliptical galaxies in the nearby Universe by Malin & Carter (1983). We measured surface brightnesses of $\mu_V=23.2$ and $23.6 \text{ mag arcsec}^{-2}$ for the inner and outer shells, respectively. The larger of the shells to the SE was also detected by H86, while Inskip et al. (2010) detected the inner shell to the SE (16 kpc radial distance from the nucleus) in the K-band, claiming that an elongated tidal feature appears to be connecting the galaxy nucleus with a satellite object to the South. Emission line contamination can be ruled out, since strong emission lines do not fall in the r' filter used for the observations.

A16 PKS 0806-10 (3C195).

The GMOS-S image of this NLRG/FRII (Figure B16) shows a clearly disturbed morphology, including features such as a broad fan towards the East ($\mu_V=23.4 \text{ mag arcsec}^{-2}$), a bright shell to NW, and a fainter shell towards the West ($\mu_V=23.3$ and $24.6 \text{ mag arcsec}^{-2}$, respectively). The *unsharp-masked* image also show several bright knots of emission closer to the galaxy center (see Figure B16a). Emission line contamination of the features is not a serious issue here because strong emission lines do not fall in the r' -band filter employed in our observations. Inskip et al. (2010) also report the detection of the NW shell (or arc-like feature) in their K-band images. They claim also that the galaxy is possibly interacting with the small disk galaxy companion at $\sim 10 \text{ kpc}$ East. Finally, based in optical imaging of the galaxy using the Canada-France-Hawaii Telescope (CFHT), Hutchings et al. (1988) reported that the radio galaxy appears asymmetrical, and probably undergoing an interaction, from the high concentration of faint objects located within a $20''$ radius from the galaxy center.

A17 PKS 1839-48.

This WLRG/FRI galaxy is the brightest member of a group or cluster, with its spectrum presenting several absorption lines typical of early-type galaxies, but no strong emission lines (Tadhunter et al. 1993). Our GMOS-S image (Figure B17) shows an apparent secondary nucleus within a 5.6 kpc radius to the SE, a bright arc-like shell $\sim 7 \text{ kpc}$ to the NW, and a tentative narrow and sharp tail NE. It is also possible that the radio galaxy is interacting with the two galaxies aligned along the SW direction, since at least one them appears clearly disturbed. Emission line contamination can be ruled out, since strong emission lines do not fall in the filter used. The bright and sharp shell-like feature described

above appears different to the shells/arcs detected for other galaxies in our sample. Indeed, considering that PKS 1839-48 is a massive galaxy immersed in a rich cluster, we cannot discard the possibility of this arc/shell being the result of gravitational lensing.

A18 PKS 0043-42.

This WLRG/FRII appears to be located in the center of a group or cluster, surrounded by an extended diffuse halo (Figure B18). There is faint companion located ~ 8 kpc NE of the galaxy center. However, the lack of any other features and of galaxy distortion in this direction prevents us from classifying the radio galaxy as a double nucleus system, based on its optical morphology. However, from the K-band image presented in Inskip et al. (2010), the authors reported a central isophotal twist and an excess of emission along the NS direction. They claimed that both are likely to be associated either to the presence of a dust lane or to the apparent interaction with the companion object ~ 15 kpc to the North. Indeed, the residuals in the model-subtracted image reported by Inskip et al. (2010) show a bridge-like structure linking with the northern companion. Although we have classified the radio galaxy as undisturbed, by looking at our *smoothed galaxy-subtracted* optical image (see Figure B18a), it is possible to unveil the existence of a bridge linking with the small galaxy at the north.

A19 PKS0213-13 (3C62).

The GMOS-S image of this NLRG/FRII galaxy (Figure B19) reveals one of the most clear systems of shells in our sample. We measured a surface brightness of $\mu_V = 24.7$ mag arcsec $^{-2}$ for the brighter shell (~ 20 kpc to the North) and 25.1 mag arcsec $^{-2}$ for the eastern and outer shell (~ 27 kpc from the nucleus). Our *unsharp-masked* image also shows the presence of a narrow and sharp tidal tail to the SW (see Figure B19a). The galaxy morphology of 3C62 was also studied by H86, but they did not report the existence of any feature. Our long-slit spectrum of this galaxy shows that emission line contamination is not a serious issue for the shell structure to the NE.

A20 PKS 0442-28.

This NLRG/FRII galaxy shows a faint, but sharply defined shell ~ 50 kpc to SW of its nucleus in our GMOS-S image (Figure B20). This shell has a surface brightness $\mu_V = 25.7$ mag arcsec $^{-2}$. There are several galaxies within $\sim 20''$, any of them possibly interacting with the radio galaxy. There are neither optical long-slit spectra nor infrared data suitable for assessing the degree of emission line contamination of this shell.

A21 PKS2211-17 (3C444).

This WLRG/FRII is in the center of a cluster, and its optical morphology was studied by H86 in the past, but their optical images did not reveal any features. In our GMOS-S image (Figure B21) the galaxy appears surrounded by the diffuse halo typical of central cluster galaxies, and also shows

hints of a broad fan or shells towards the NE. By looking at our processed images, we also detect a knotty sub-structure in the near-nuclear regions of the galaxy, which may be due to patchy dust obscuration. Evidence for a dust lane is also found in the model-subtracted NIR image of Inskip et al. (2010). The NIR data also reveal an excess of diffuse emission towards the East, coinciding with our tentative detection of a fan or a shell. This source is one of the three galaxies in our sample with dust as the only feature with secure detection.

A22 PKS 1648+05 (3C348, Herc A).

This WLRG/FRI source is at the center of a cooling flow cluster of galaxies at $z=0.154$. A recent analysis of Chandra X-ray data showed that the cluster has cavities and a shock front associated with the radio source (Nulsen et al. 2005). H86 did not report the existence of any feature for this galaxy from their optical imaging. However, our Gemini data (Figure B22) reveal patchy dust features crossing the galaxy nucleus in a roughly East-West direction, out to a radius of ~ 6.5 kpc to the East. Note that de Koff et al. (1996) and Baum et al. (1996) have used the HST to detect fine dust features in the nuclear regions of this galaxy, and they claim that the dust is distributed as two interlocking rings. Unfortunately our Gemini observations do not have sufficient spatial resolution to allow us to confirm the ring-like morphology of the near-nuclear dust.

A23 PKS 1934-63.

This compact NLRG/GPS source is hosted in a double and highly disturbed system. Our optical image (Figure B23) shows two bright nuclei separated by ~ 9 kpc, embedded in a common and irregular envelope. Two tidal tails extending towards the SW from the radio galaxy and to the North from its companion are detected with surface brightnesses of 23.1 and 23.4 mag arcsec $^{-2}$, respectively. All the previous features were also detected by H86 with the same μ_V values. They observed the radio galaxy and companion in both B and V bands, reporting an integrated color of $B-V=1.25$, which is ~ 0.3 mag bluer than the normal color of elliptical galaxy at $z=0.2$ (Fukugita et al. 1995). Although much of the blue light excess in this source is likely to be due to AGN-related continuum components such as scattered light and nebular continuum (see object-specific discussion in Tadhunter et al. 1994 and Tadhunter et al. 2002), evidence for on-going star formation activity in this source is provided by the detection of PAH emission features at MIR wavelengths by Dicken et al. (2010). Note that presence of the tidal features described here is also reported in the K-band imaging study of Inskip et al. (2010), indicating their continuum-emitting nature. Our long-slit spectra also confirm that the companion galaxy and its associated tidal tail are dominated by continuum emission.

A24 PKS 0038+09 (3C18).

This BLRG/FRII at $z=0.19$ is found to have about two thirds of its K-band flux in the nuclear unresolved component (Inskip et al. 2010). The galaxy appears to be in

a dense environment, with several companions within $\sim 20''$. Our GMOS-S image (Figure B24) reveals a faint and long tidal tail of surface brightness $\mu_V = 26.2$ mag arcsec $^{-2}$ extending up to 40 kpc to the NW — this is the faintest tidal feature detected in our imaging survey. The galaxy was observed with a seeing of FWHM $\sim 1''$, which makes it difficult to identify other possible signs of disturbance. In the K-band images shown in Inskip et al. (2010), the galaxy appears elongated in the direction of the tidal tail. However, due to the faintness of the latter feature, it is not clearly detected in the NIR. Our long-slit spectrum of the galaxy does not allow us to confirm/discard the emission-line nature of this tail.

A25 PKS 2135-14.

The optical image of this QSO/FRII (Figure B25) shows a disk galaxy companion at ~ 18 kpc SE and a close-in companion, or secondary nucleus, at a distance of 6 kpc. However, analysis of its spectrum showed that the latter object is actually a foreground star (Canalizo & Stockton 1997). Our GMOS-S image reveals a very disturbed morphology, including a shell in the West side of the quasar nucleus, which is embedded in an amorphous halo, and a faint tidal tail pointing to the SE. This tidal tail, which in the original image extends up to ~ 36 kpc and has a surface brightness of $\mu_V = 24.2$ mag arcsec $^{-2}$, is very likely the brightest part of a bridge linking the radio galaxy and the disturbed galaxy at ~ 134 kpc to the SE. However, the bridge is only detected in our *median-filtered image* (see Figure B25b), and thus we do not consider it as a secure morphological classification of a feature in the galaxy. The galaxy morphology was also studied by H86, but they did not report the detection of any feature. The results on the determination of the continuum or line-emitting nature of the detected features are inconclusive based on long-slit spectra (Tadhunter et al. 1998).

A26 PKS 0035-02 (3C17).

This BLRG/FRII appears clearly disturbed in our optical image (Figure B26). The radio galaxy shows a bridge linking with a companion galaxy ~ 46 kpc to the South. We also detected a fan of $\mu_V = 25.1$ mag arcsec $^{-2}$ towards the NW.

H86 did not report the detection of any feature for this galaxy. The residuals from the model subtraction of the K-band image reported in Inskip et al. (2010) display an excess of emission extending linearly from the NE to the SW, which roughly coincides with the direction of the bridge linking with the companion galaxy. This confirms the continuum-emitting nature of the bridge.

A27 PKS 2314+03 (3C459).

This NLRG/FRII with strong evidence for a YSP at both optical (Wills et al. 2008) and MIR/FIR wavelengths (Dicken et al. 2009, 2010), is classified as ULIRG based on its FIR luminosity, and appears clearly disturbed in our GMOS-S image (Figure B27). We detect two broad and symmetrical fans of $\mu_V = 23.6$ (South) and 23.3 (East) mag arcsec $^{-2}$, extending to a maximum distance of ~ 33 kpc

to the South of the nucleus, and giving an overall butterfly-like appearance. The southern fan shows some bright knots. Pointing to the North, we detect a faint tail in our processed images. This galaxy is included in the H86 sample of PRGs, and they also detected the two fans in their optical images. Our VLT spectra demonstrate that the fan features are dominated by continuum rather than emission line radiation.

A28 PKS 1932-46.

This BLRG/FRII appears to be a member of a small interacting group of galaxies which includes a starburst galaxy at a similar redshift at ~ 100 kpc to the NE (Inskip et al. 2007). Optical spectroscopy of the radio galaxy reveals an extended population of very young (< 10 Myr) stars in the galaxy halo (Villar-Martín et al. 2005; Holt et al. 2007). Our Gemini image (Figure B28) shows an extremely disturbed morphology, including two symmetrical fans towards North and East ($\mu_V = 23.6$ and 23.5 mag arcsec $^{-2}$, respectively), very similar to those detected in PKS 2314+03. The galaxy is embedded in an amorphous halo showing some bright knots. But the most spectacular feature is an extraordinary series of arc-like irregular features up to ~ 70 kpc distance from the galaxy center, which almost connect with the highly disturbed starburst galaxy mentioned above. Our long-slit spectra demonstrate that the latter arcs emit a combination of continuum and line radiation, and are not solely due to emission line contamination.

A29 PKS 1151-34.

The presence of a YSP in this QSO/CSS is indicated by the presence of PAH features in its Spitzer MIR spectrum (Dicken et al. 2010). Our GMOS-S image (Figure B29) reveals a spectacular extended structure for this system, with a prominent tidal tail/arc feature ~ 34 kpc to the NW that connects to a compact secondary nucleus ~ 27 kpc to the North of the quasar, as well as a broad fan of emission extending ~ 38 kpc to the East of the nucleus. The overall morphology of the extended structure to the N-NW suggests that the quasar host galaxy is strongly interacting with a late-type spiral galaxy (possibly a barred spiral galaxy). Since the spiral structure of the interacting galaxy is reasonably coherent (although somewhat asymmetric), it appears that we are observing the system around the first peri-centre of the interacting galaxies, rather than in the final stages of a merger as the nuclei coalesce. For this galaxy there are neither optical spectra nor infrared data suitable for assessing the degree of emission line contamination of the detected features.

A30 PKS 0859-25.

The source PKS 0859-25, which is immersed in a relatively crowded field, appears in our GMOS-S image as a double nucleus system including the radio galaxy nucleus and a faint component ~ 6 kpc the SW (Figure B30). This morphological classification is confirmed by the NIR observations and analysis presented by Inskip et al. (2010).

A31 PKS 2250-41.

This NLRG is likely lying within a group, and possibly interacting with one or even more objects according to the detailed analysis presented by Inskip et al. (2008) using imaging and spectroscopy in the optical and NIR. The presence of a YSP is confirmed by the presence of PAH features in the Spitzer MIR spectrum of this source (Dicken et al. 2010). The disk galaxy at 47 kpc to the NE of the radio source is at an almost identical redshift to PKS 2250-41 (Inskip et al. 2008), and appears clearly disturbed in the direction of the radio galaxy. Our i' -band GMOS-S image (Figure B31) reveals a faint bridge linking with this NE companion, and a shorter one linking the radio galaxy with the smaller galaxy at 27 kpc towards the SW. The galaxy was observed in using the i' -band filter in order to avoid contamination with the extended [O III] λ 5007 Å line emission, which we know is very prominent from optical spectra (Tadhunter et al. 2002). Indeed, the long-slit spectrum of the galaxy shows that emission line contamination is not a serious issue for all the peculiar features detected. Finally, it is possible to distinguish a faint arc-like tail extending to the West from the small galaxy companion and a fan towards the East of the radio galaxy.

A32 PKS 1355-41.

This QSO at redshift $z=0.31$ has the best seeing among all the GMOS-S observations presented here (FWHM $\sim 0.4''$). This fact is clearly reflected in the high-quality of the images and the level of detail of the identified features (Figure B32). There is a sharp shell feature ~ 24 kpc to the SE of the quasar and covering an angle of $\sim 60^\circ$, along with a bright and sharp tail extending up to ~ 22 kpc to the SE along PA $=121^\circ$ and pointing towards the arc. Although the latter feature is closely aligned with the axis of the large-scale radio structure (PA $=125^\circ$), the high frequency radio map presented in Dicken et al. (2008) shows no sign of any radio emission from the tail that might suggest that it is non-thermal in nature. For this galaxy, there are neither optical long-slit spectra nor infrared data suitable for assessing the degree of emission line contamination of the detected features.

A33 PKS 0023-26.

This NLRG/CSS source appears to lie within a dense cluster environment. Indeed, the two galaxies to either side (at 25 kpc SW and 33 kpc NE) have similar redshifts to the radio galaxy host (Tadhunter et al. 2010). In our GMOS-S image (Figure B33), all three galaxies appear embedded in a common envelope, which has amorphous appearance close to the radio galaxy, and is possibly crossed by dust lanes. The presence of dust here is consistent with the detection of a YSP in the optical spectrum of the radio galaxy (Holt et al. 2007), and the FIR excess revealed by Spitzer (Dicken et al. 2009). Our optical spectrum of the galaxy confirms that emission line contamination is not a serious issue for this amorphous halo.

A34 PKS 0347+05.

The WLRG/FRII PKS 0347+05 is part of a spectacular interacting system, which includes a QSO/Seyfert 1 nucleus ~ 26 kpc to the SW of the radio galaxy host itself (Figure B34). This object provides some of the best evidence for the triggering of radio/AGN activity as a result of a galaxy interaction in our sample. In addition, Spitzer MIR and FIR data for the WLRG reveal the presence of a YSP, based on the detection of a FIR excess (Dicken et al. 2009) and strong PAH features (Dicken et al. 2010). Our GMOS-S image shows a bridge linking the two interacting galaxies, and at least three tidal tails extending to the SW of the system. The closest tail to the QSO is the brightest, presenting a bright knot at the closest edge. The presence of dust features close to the radio galaxy is also clear, and consistent with a star-forming region. Long-slit spectra of the galaxy show that emission line contamination is not a serious issue for most of the peculiar features detected in this system. This object will be the subject of a detailed study of its combined optical, infrared, and radio properties (Ramos Almeida et al., in prep.).

A35 PKS 0039-44.

The nucleus of this NLRG appears to be double in our GMOS-S optical image (separation ~ 4 kpc; see inset in Figure B35). Shell features are detected ~ 16 kpc to the NW ($\mu_V=23.3$ mag arcsec $^{-2}$) and ~ 16 and ~ 27 kpc ($\mu_V=23.3$ and 24.1 mag arcsec $^{-2}$ respectively) to the SE of the nucleus. Although we do not consider it for the morphological classification of PKS 0039-44, it is possible to unveil a faint tail pointing to the star-like companion at ~ 70 kpc to the West. This tentative tail appears co-aligned with the system of shells. Dust seems to be also present in the galaxy nucleus. Emission line contamination cannot be ruled out based on long-slit spectra for the case of the shells and the tail. However, our spectra show that the apparent secondary nucleus is likely to be dominated by [O III] λ 5007 Å emission line radiation.

A36 PKS 0105-16 (3C32).

Our GMOS-S i' -band image of this NLRG/FRII (Figure B36) reveals a bridge of $\mu_V=24.6$ mag arcsec $^{-2}$ that appears to link the radio galaxy host with an early-type galaxy of similar brightness ~ 70 kpc NW. Emission line contamination of the detected feature cannot be ruled out based on the existing long-slit spectra.

A37 PKS 1938-15.

This BLRG/FRII lies in a very dense environment, and in our optical image appears to have several diffuse companions within a $10''$ radius (Figure B37). We detect a tail/fan of $\mu_V=23.2$ mag arcsec $^{-2}$ extending up to 20 kpc to the NE of the radio galaxy. It also looks very probable that PKS 1938-15 is interacting with the companion lying at 18 kpc to the East. There are neither optical long-slit spectra nor infrared data suitable for assessing the degree of emission line contamination of the detected features in this galaxy.

A38 PKS 1602+01 (3C327.1).

This BLRG/FRII at redshift $z=0.46$ shows several signs of interaction in our i' -band GMOS-S image (Figure B38). Towards the North of the galaxy nucleus we detect a bright and smooth fan of $\mu_V=21.34$ mag arcsec $^{-2}$. On the opposite side there is a shell of $\mu_V=23.3$ mag arcsec $^{-2}$. Finally, and immersed in the shell envelope, we detect a sharp knot-like feature that extends up to 23 kpc and that is closely aligned (PA=148°) with the inner axis of the radio jet (PA=145°; see radio images in Morganti et al. 1999). At a distance of 18 kpc from the nucleus, the latter feature is close to, but does not exactly coincide with the third knot in the radio jet leading to the South of the nucleus. The WFPC2/HST images of this galaxy only revealed an elliptical nucleus with a faint halo of emission surrounding it (de Koff et al. 1996). For this galaxy, there are neither optical long-slit spectra nor infrared data suitable for assessing the degree of emission line contamination of the detected features.

A39 PKS 1306-09.

Our GMOS-S image (Figure B39) reveals a secondary nucleus for this NLRG/CSS source, which is also detected in the residuals of the model-subtracted K-band image analyzed by Inskip et al. (2010). The galaxy lies in a group of galaxies. From both the optical and NIR data, the radio galaxy is very likely undergoing interactions with other objects in the group. In addition to the double nucleus, we detect a sharply-defined shell ~ 20 kpc to SE of the radio galaxy, of surface brightness $\mu_V=24.5$ mag arcsec $^{-2}$.

A40 PKS 1547-79.

We classify this BLRG/FRII as a double nucleus system, since the radio source has a fainter companion ~ 9 kpc to the South of the nucleus, as revealed by our GMOS-S image (Figure B40). In addition, our GMOS-S optical image reveals a tidal tail extending ~ 27 kpc to the NE of the galaxy center of surface brightness $\mu_V=24.3$ mag arcsec $^{-2}$. In both the optical and the NIR, PKS 1547-79 appears as a clear interacting system, surrounded by several diffuse companions. Note that the companion galaxy ~ 46 kpc to the West of the radio galaxy host has weak emission lines that suggest a similar redshift to PKS1547-79. On the other hand, the much brighter early-type galaxy ~ 70 kpc to the East, which also shows some signs of morphological disturbance, is at a much lower redshift. The continuum-emitting nature of the tidal tail of PKS1547-79 cannot be either confirmed or discarded based on existing long-slit spectra (Tadhunter et al. 1998), but the secondary nucleus is detected in the NIR (Inskip et al. 2010).

A41 PKS 1136-13.

Our GMOS-S image of this QSO/FRII at redshift $z=0.55$ (Figure B41) reveals the optical counterpart of a radio jet extending up to 60 kpc in the NW from the radio galaxy (Uchiyama et al. 2007). We also detect a shorter tidal tail pointing to the West of the quasar, for which we measure a surface brightness of $\mu_V=22.6$ mag arcsec $^{-2}$. It is also possible to unveil another tail SE of the nucleus. The lack of

either optical long-slit spectra or infrared data suitable for assessing the degree of emission line contamination of the detected features prevents us from confirming whether the extended structures are dominated by continuum radiation.

A42 PKS 0117-15 (3C38).

Our optical image of this NLRG/FRII, taken in excellent seeing conditions (FWHM=0.5''), shows a high-surface-brightness triple nucleus system of ~ 9 kpc diameter co-aligned along PA=8° (Figure B42). In addition, we detect a shell on the western side of the radio galaxy extending up to 21 kpc, for which we measure a surface brightness of $\mu_V=25.1$ mag arcsec $^{-2}$, as well as an arc-like structure (identified as "I" in Table 1) of $\mu_V=21.3$ mag arcsec $^{-2}$ and a companion galaxy ~ 9 kpc and ~ 17 kpc to the NE of the central nucleus respectively. Interestingly, the NE arc shows a gap close to its interception with the axis of the large scale radio structure (PA=35°). This suggests a possible interaction between the arc and the radio jet. However, although the central triple structure shows some resemblance with the structures found closely aligned with the radio axes of some high redshift radio galaxies (e.g. McCarthy et al. 1987; Best et al. 1996) it is, in fact, significantly misaligned from the radio axis by 27 degrees. Therefore, it is uncertain whether the latter structure is due to jet/cloud interactions. Dust features between the triple system components are tentatively detected in our processed images. The results on the degree of emission line contamination of the detected features are inconclusive, based on our existing long-slit spectra. Clearly, further optical spectroscopic and NIR imaging observations are required to determine whether the central triple structure is stellar in nature, or represents a manifestation of the "alignment effect" frequently observed in high redshift radio galaxies.

A43 PKS 0252-71.

The NLRG/CSS galaxy PKS 0252-71 appears to be surrounded by an amorphous halo which points towards a fainter companion galaxy at ~ 33 kpc to the South, thus indicating a possible interaction between the galaxies (Figure B43). Note that the bright object $\sim 3''$ to the SE of the radio galaxy host is a star. Unfortunately, the relatively poor seeing of this image (FWHM=1'') prevents a clear detection of other possible signs of disturbance.

A44 PKS 0235-19 (OD-159).

Our GMOS-S image of this BLRG/FRII at redshift $z=0.62$ (Figure B44) shows tidal tails of similar surface brightness to both the NE and SW of the nucleus along PA=52°, with a maximum extent of ~ 15 kpc to the NE ($\mu_V=22.2$ and 22.4 mag arcsec $^{-2}$ for the NE and SW tails, respectively). Apart from the tidal tails, another interpretation of the observed structures is that they represent a warped disk structure with the BLRG nucleus at its centre. The tail/disk structure is significantly mis-aligned by 42 degrees from the axis of the large scale radio structure (PA=94°). Although we do not consider it for the morphological classification of the galaxy, there is tentative evidence for a bridge linking the

radio galaxy with the smaller galaxy 165 kpc to the NE. The bridge appears as a elongation of the NE tidal tail, but much fainter. Our long-slit spectra of this galaxy suggest that line contamination may be a serious issue for the tail/disk structure.

A45 PKS 2135-20 (OX-258).

Our optical image of this BLRG/CSS (Figure B45) shows a broad fan on the northern side of the radio galaxy, of surface brightness $\mu_V=23.5$ mag arcsec $^{-2}$. This feature is very likely the result of a past interaction, consistent with the detection of a YSP in the nuclear region of this galaxy from optical spectroscopy (Holt et al. 2007), FIR excess (Dicken et al. 2009), and the detection of strong PAH features (Dicken et al. 2010). The results regarding the continuum or line-emitting nature of this fan are inconclusive based on our long-slit spectra. Note that PKS2135-20 is one of the only two galaxies (the other is PKS 2314+03) in our sample that would be classified as ULIRGs based on their MIR and FIR luminosities.

A46 PKS 0409-75.

This NLRG/FRII with evidence for a YSP based on its optical spectrum (Holt et al. 2007), FIR excess and infrared colours (Dicken et al. 2009), is the most distant object in our sample. Our GMOS-S i' -band image reveals a secondary nucleus of similar brightness to the radio galaxy ~ 8 kpc to the East along PA=84° (Figure B46). Note that the axis of the double nucleus is misaligned by ~ 40 degrees from the axis of the large-scale radio structure (PA=124°). The double nucleus system lies in a crowded field, and there are several galaxies within a 20'' radius. Although the system looks disturbed, unfortunately the high value of the seeing measured for this image (FWHM=1.15'') prevents any more detailed morphological classification. The continuum or line-emitting nature of the secondary nucleus is uncertain based on long-slit spectra of this source.

ACKNOWLEDGMENTS

CRA acknowledges financial support from STFC PDRA (ST/G001758/1). KJI is supported through the Emmy Noether programme of the German Science Foundation (DFG). This work is based on observations obtained at the Gemini Observatory, which is operated by the Association of Universities for Research in Astronomy, Inc., under a cooperative agreement with the NSF on behalf of the Gemini partnership: the National Science Foundation (United States), the Science and Technology Facilities Council (United Kingdom), the National Research Council (Canada), CONICYT (Chile), the Australian Research Council (Australia), Ministério da Ciência e Tecnologia (Brazil), and Ministerio de Ciencia, Tecnología e Innovación Productiva (Argentina). The Gemini programs under which the data were obtained are GS-2008B-Q-44 and GS-2009A-Q-54. This research has made use of the NASA/IPAC Extragalactic Database (NED) which is operated by the Jet Propulsion Laboratory, California Institute of Technology, under contract with the National Aeronautics and Space

Administration. C.R.A. acknowledges Pieter van Dokkum, and Rubén Díaz for their valuable help. We finally acknowledge useful comments from the anonymous referee.

REFERENCES

- Allen, S. W., Dunn, R. J. H., Fabian, A. C., Taylor, G. B., Reynolds, C. S. 2006, MNRAS, 372, 21
- Aretxaga, I., Terlevich, E., Terlevich, R. J., Cotter, G., Díaz, A. I. 2001, MNRAS, 325, 636
- Balmaverde, B., Baldi, R. D., Capetti, A. 2008, A&A, 486, 119
- Barnes, J. E., Hernquist, L. 1996, ApJ, 471, 115
- Baum, S. A., O'Dea, C. P., de Koff, S., Sparks, W., Hayes, J. J. E., Livio, M., Golombek, D. 1996, ApJ, 465, L5
- Baum, S. A., Heckman, T., van Breugel, W. 1992, ApJ, 398, 208
- Bell, E. F., Naab, T., McIntosh, D. H., et al. 2006, ApJ, 640, 241
- Bendo, G. J., Barnes, J. E. 2000, MNRAS, 316, 315
- Bennert, N., Canalizo, G., Jungwiert, B., Stockton, A., Schweizer, F., Peng, C. Y., Lacy, M. 2008, ApJ, 677, 846
- Best, P. N., Kaiser, C. R., Heckman, T. M., Kauffmann, G. 2006, MNRAS, 368, L67
- Best, P. N., Longair, M. S., Rottgering, H. J. A. 1996, MNRAS, 280, L9
- Black, A. R. S., Baum, S. A., Leahy, J. P., Perley, R. A., Riley, J. M., Scheuer, P. A. G., 1992, MNRAS, 256, 186
- Borne, K. D., Hoessel, J. G. 1985, BAAS, 17, 601
- Borne, K. D. 1984, ApJ, 287, 503
- Bremer, M. N., Fabian, A. C., Crawford, C. S. 1997, MNRAS, 284, 213
- Bryant, J. J., Hunstead, R. W. 2002, MNRAS, 337, 861
- Buttiglione, S., Capetti, A., Celotti, A., Axon, D. J., Chisaberge, M., Macchetto, F. D., Sparks, W. B. 2010, A&A, 509, 6
- Buttiglione, S., Capetti, A., Celotti, A., et al. 2009, A&A, 495, 1033
- Canalizo, G., Bennert, N., Jungwiert, B., Stockton, A., Schweizer, F., Lacy, M., Peng, C. 2007, ApJ, 669, 801
- Canalizo, G., Stockton, A. 1997, ApJ, 480, L5
- Cardelli, J.A., Clayton, G.C., Mathis, J. 1989, ApJ, 345, 245
- Cattaneo, A., Faber, S. M., Binney, J., et al. 2009, Nature, 460, 213
- Cattaneo, A., Combes, F., Colombi, S., Bertin, E., Melchior, A.-L. 2005, MNRAS, 359, 1237
- Colbert, J. W., Mulchaey, J. S., Zabludoff, A. I. 2001, AJ, 121, 808
- Combes, F., Rampazzo, R., Bonfanti, P. P., Prugniel, P., Sulentic, J. W. 1995, A&A, 297, 37
- Conselice, C. J., Bershadsky, M. A., Dickinson, M., Papovich, C. 2003, AJ, 126, 1183
- Cox, T. J., Jonsson, P., Primack, J. R., Somerville, R. S. 2006, MNRAS, 373, 1013
- Danziger, I. J., Fosbury, R. A. E., Boksenberg, A., Goss, W. M., Bland, J. 1984, MNRAS, 208, 589
- de Koff, S. 2000, ApJs, 129, 33
- de Koff, S. 1996, ApJs, 107, 621
- Dicken, D., Tadhunter, C., Axon, D., et al. 2010, ApJ, submitted

- Dicken, D., Tadhunter, C., Axon, D., Morganti, R., Inskip, K. J., Holt, J., González Delgado, R., Groves, B. 2009, *ApJ*, 694, 268
- Dicken, D., Tadhunter, C., Morganti, R., Buchanan, C., Oosterloo, T., Axon, D. 2008, *ApJ*, 678, 712
- di Matteo, P., Combes, F., Melchior, A.-L., Semelin, B. 2007, *A&A*, 468, 61
- Di Matteo, T., Springel, V., Hernquist, L. 2005, *Nature*, 433, 604
- di Serego Alighieri, S., Danziger, I. J., Morganti, R., Tadhunter, C. N. 1994, *MNRAS*, 269, 998
- Dunlop, J. S., McLure, R. J., Kukula, M. J., Baum, S. A., O'Dea, C. P., Hughes, D. H. 2003, *MNRAS*, 340, 1095
- Dunlop, J. S., Peacock, J. A. 1990, *MNRAS*, 247, 19
- Dupraz, C., Combes, F. 1986, *A&A*, 166, 53
- Edge, A. C., Oonk, J. B. R., Mittal, R., et al. 2010, *A&A*, 518, L47
- Edge, A. C., Ivison, R. J., Smail, Ian, Blain, A. W., Kneib, J.-P. 1999, *MNRAS*, 306, 599
- Fabian, A. C., Sanders, J. S., Taylor, G. B., Allen, S. W., Crawford, C. S., Johnstone, R. M., Iwasawa, K. 2006, *MNRAS*, 366, 417
- Fabian, A. C., Johnstone, R. M., Daines, S. J. 1994, *MNRAS*, 271, 737
- Fasano, G., Falomo, R., Scarpa, R. 1996, *MNRAS*, 282, 40
- Feldmann, R., Mayer, L., Carollo, C. M. 2008, *ApJ*, 684, 1062
- Ferrarese, L., Merritt, D. 2000, *ApJ*, 539, L9
- Frei, Z., Gunn, J. E. 1994, *AJ*, 108, 1476
- Fukugita, M., Ichikawa, T., Gunn, J. E., Doi, M., Shimasaku, K., Schneider, D. P. 1996, *AJ*, 111, 1748
- Fukugita, M., Shimasaku, K., Ichikawa, T. 1995, *PASP*, 107, 945
- Gebhardt, K., Bender, R., Bower, G., et al. 2000, *ApJ*, 539, L13
- Ghisellini, G., Celotti, A. 2001, *A&A*, 379, L1
- Govoni, F., Falomo, R., Fasano, G., Scarpa, R. 2000, *A&A*, 353, 507
- Greene, J. E., Ho, L. C. 2006, *ApJ*, 641, L21
- Grogin, N. A., Conselice, C. J., Chatzichristou, E., et al. 2005, *ApJ*, 627, L97
- Hansen, L., Jorgensen, H. E., Norgaard-Nielsen, H. U. 1995, *A&AS*, 297, 13
- Hansen, L., Jorgensen, H. E., Norgaard-Nielsen, H. U. 1987, *A&AS*, 71, 465
- Hardcastle, M. J., Evans, D. A., Croston, J. H. 2007, *MNRAS*, 376, 1849
- Heckman, T. M., Smith, E. P., Baum, S. A., van Breugel, W. J. M., Miley, G. K., Illingworth, G. D., Bothun, G. D., Balick, B. 1986, *ApJ*, 311, 526
- Hernquist, L., Spergel, D. L. 1992, *ApJ*, 399, L117
- Hoessel, J. G. 1980, *ApJ*, 241, 493
- Holt, J., Morganti, R., et al. 2010, *MNRAS*, in prep.
- Holt, J., Tadhunter, C. N., González Delgado, R. M., Inskip, K. J., Rodríguez Zaurín, J., Emonts, B. H. C., Morganti, R., Wills, K. A. 2007, *MNRAS*, 381, 611
- Hook, I., Jørgensen, I., Allington-Smith, J. R., Davies, R. L., Metcalfe, N., Murowinski, R. G., Crampton, D. 2004, *PASP*, 116, 425
- Hopkins, P. F., Cox, T. J., Kereš, D., Hernquist, L. 2008a, *ApJs*, 175, 390
- Hopkins, P. F., Hernquist, L., Cox, T. J., Kereš, D. 2008b, *ApJs*, 175, 356
- Hutchings, J. B., Johnson, I., Pyke, R. 1988, *ApJs*, 66, 361
- Inskip, K. J., Tadhunter, C. N., Morganti, R., Holt, J., Ramos Almeida, C., Dicken, D. 2010, *MNRAS*, in press, arXiv:1005.2195
- Inskip, K. J., Villar-Martín, M., Tadhunter, C. N., Morganti, R., Holt, J., Dicken, D. 2008, *MNRAS*, 386, 1797
- Inskip, K. J., Tadhunter, C. N., Dicken, D., Holt, J., Villar-Martín, M., Morganti, R. 2007, *MNRAS*, 382, 95
- Kauffmann, G., Haehnelt, M. 2000, *MNRAS*, 311, 576
- Kawata, D., Mulchaey, J. S., Gibson, B. K., Sánchez-Blázquez, P. 2006, *ApJ*, 648, 969
- Leahy, J. P., Muxlow, T. W. B., Stephens, P. W. 1989, *MNRAS*, 239, 401
- Le Fèvre, O., Abraham, R., Lilly, S. J., et al. 2000, *MNRAS*, 311, 565
- Lotz, J. M., Jonsson, P., Cox, T. J., Primack, J. R. 2008, *MNRAS*, 391, 1137
- Madau, P., Ferguson, H. C., Dickinson, M. E., Giavalisco, M., Steidel, C. C., Fruchter, A. 1996, *MNRAS*, 283, 1388
- Malin, D. F., Carter, D. 1983, *ApJ*, 274, 534
- Martel, A. R., Baum, S. A., Sparks, W. B. et al. 1999, *ApJS*, 122, 81
- Martel, A. R., Sparks, W. B., Macchetto, D., et al. 1998, *ApJ*, 496, 203
- McCarthy, P. J., van Breugel, W., Spinrad, H., Djorgovski, S. 1987, *ApJ*, 321, L29
- McGaugh, S. S., Bothun, G. D. 1990, *AJ*, 100, 1073
- McIntosh, D. H., Guo, Y., Hertzberg, J., Katz, N., Mo, H. J., van den Bosch, F. C., Yang, X. 2008, *MNRAS*, 388, 1537
- Melnick, J., Gopal-Krishna, Terlevich, R. 1997, *A&A*, 318, 337
- Mihos, J. C., Hernquist, L. 1996, *ApJ*, 464, 641
- Morganti, R., Oosterloo, T., Tadhunter, C. N., Aiudi, R., Jones, P., Villar-Martín, M. 1999, *A&AS*, 140, 355
- Morganti, R., Oosterloo, T. A., Reynolds, J. E., Tadhunter, C. N., Migenes, V. 1997, *MNRAS*, 284, 541
- Morganti, R., Killeen, N. E. B., Tadhunter, C. N. 1993, *MNRAS*, 263, 1023
- Naab, T., Khochfar, S., Burkert, A. 2006, *ApJ*, 636, L81
- Naab, T., Burkert, A. 2003, *ApJ*, 597, 893
- Naab, T., Burkert, A., Hernquist, L. 1999, *ApJ*, 523, L133
- Nulsen, P. E. J., Hambrick, D. C., McNamara, B. R., Rafferty, D., Birzan, L., Wise, M. W., David, L. P. 2005, *ApJ*, 625, L9
- Osterbrock, D. E., Koski, A. T., Phillips, M. M. 1975, *ApJ*, 197, L41
- Patton, D. R., Pritchet, C. J., Carlberg, R. G., et al. 2002, *ApJ*, 565, 208
- Peng, E. W., Ford, H. C., Freeman, K. C., White, R. L. 2002, *AJ*, 124, 3144
- Prieto, M. A., Walsh, J. R., Fosbury, R. A. E., di Serego Alighieri, S. *MNRAS*, 263, 10
- Quinn, P. J. 1984, *ApJ*, 279, 596
- Rodríguez Zaurín, J., Tadhunter, C. N., González Delgado, R. M. 2010, *MNRAS*, 403, 1317
- Rodríguez Zaurín, J., Tadhunter, C. N., González Delgado, R. M. 2009, *MNRAS*, 400, 1139
- Roche, N., Eales, S. A. 2000, *MNRAS*, 317, 120
- Rogers, B., Ferreras, I., Kaviraj, S., Pasquali, A., Sarzi, M. 2009, *MNRAS*, 399, 2172

Sanders, D. B., Mirabel, I. F. 1996, ARA&A, 34, 749
 Schlegel, D. J., Finkbeiner, D. P., & Davis, M. 1998, ApJ, 500, 525
 Schweizer, F. 1980, ApJ, 237, 303
 Siebert, J., Brinkmann, W., Morganti, R., Tadhunter, C. N., Danziger, I. J., Fosbury, R. A. E., di Serego Alighieri, S. 1996, MNRAS, 279, 1331
 Sikkema, G., Carter, D., Peletier, R. F., Balcells, M., Del Burgo, C., Valentijn, E. A. 2007, A&A, 467, 1011
 Smith, E. P., Heckman, T. M. 1989, ApJ, 341, 658
 Somerville, R. S., Hopkins, P. F., Cox, T. J., Robertson, B. E., Hernquist, L. 2008, MNRAS, 391, 481
 Sparks, W. B., Baum, S. A., Biretta, J., Macchetto, F. D., Martel, A. R. 2000, ApJ, 542, 667
 Springel, V., Di Matteo, T., Hernquist, L. 2005, MNRAS, 361, 776
 Tadhunter, C., Holt, J., González Delgado, R., et al. MNRAS, in prep.
 Tadhunter, C., Robinson, T. G., González Delgado, R. M., Wills, K., Morganti, R. 2005, MNRAS, 356, 480
 Tadhunter, C., Dickson, R., Morganti, R., Robinson, T. G., Wills, K., Villar-Martín, Hughes, M. MNRAS, 330, 977
 Tadhunter, C. N., Morganti, R., Robinson, A., Dickson, R., Villar-Martín, M., Fosbury, R. A. E. 1998, MNRAS, 298, 1035
 Tadhunter, C. N., Shaw, M. A., Morganti, R. 1994, MNRAS, 271, 807
 Tadhunter, C. N., Morganti, R., di Serego-Alighieri, S., Fosbury, R. A. E., Danziger, I. J. 1993, MNRAS, 263, 999
 Tadhunter, C. N., Fosbury, R. A. E., Quinn, P. J. 1989, MNRAS, 240, 225
 Tadhunter, C. N. 1986, PhD thesis, Univ. Sussex
 Tal, T., van Dokkum, P. G., Nelán, J., Bezanson, R. 2009, AJ, 138, 1417
 Toomre, A., Toomre, J. 1972, ApJ, 178, 623
 Trussoni, E., Vagnetti, F., Massaglia, S., et al. 1999, A&A, 348, 437
 Uchiyama, Y., Urry, C. M., Coppi, P., et al. 2007, ApJ, 661, 719
 van Dokkum, P. G. 2005, ApJ, 130, 2647
 van Dokkum, P. G., Franx, M. 1995, AJ, 110, 2027
 Veilleux, S., Kim, D.-C., Sanders, D. B. 2002, ApJS, 143, 315
 Villar-Martín, M., Tadhunter, C. N., Morganti, R., Holt, J. 2005, MNRAS, 359, L5
 Wall, J. V., Peacock, J. A. 1985, MNRAS, 216, 179
 Wills, K. A., Tadhunter, C., Holt, J., González Delgado, R., Inskip, K. J., Rodríguez Zaurín, J., Morganti, R. 2008, MNRAS, 385, 136
 Wills, K. A., Morganti, R., Tadhunter, C. N., Robinson, T. G., Villar-Martín, M. 2004, MNRAS, 347, 771

subtraction), and present here the results for the two techniques in which the features appear most clearly. The PRGs are placed at the centre of each field (Figures B1 to B46), unless otherwise indicated.

APPENDIX B: ONLINE-ONLY PROCESSED IMAGES

Here we present our processed Gemini GMOS-S images for all the galaxies in the sample, ordered by redshift, as in Tables 1, 2, and 3 and in Appendix A. We tried the three techniques described in Section 4 with all the galaxies (namely, *Image filtering*, *Unsharp-masking*, and *Smoothed galaxy*

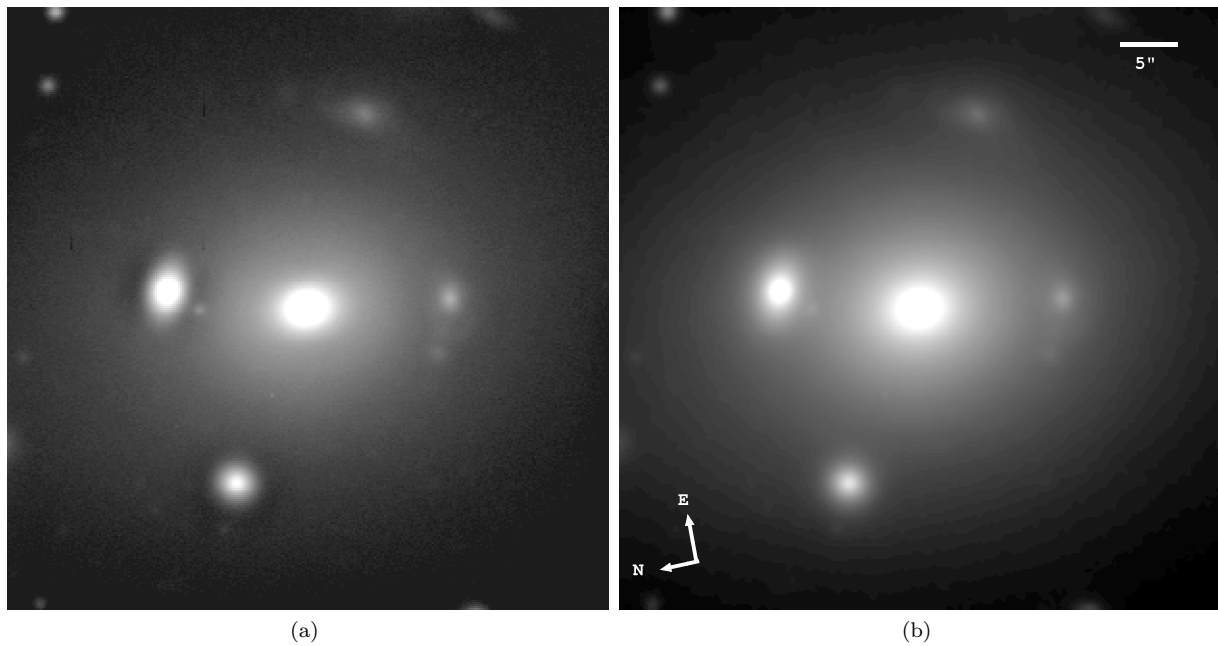


Figure B1. PKS 0620-52. (a) Unsharp-masked image. (b) Median filtered image.

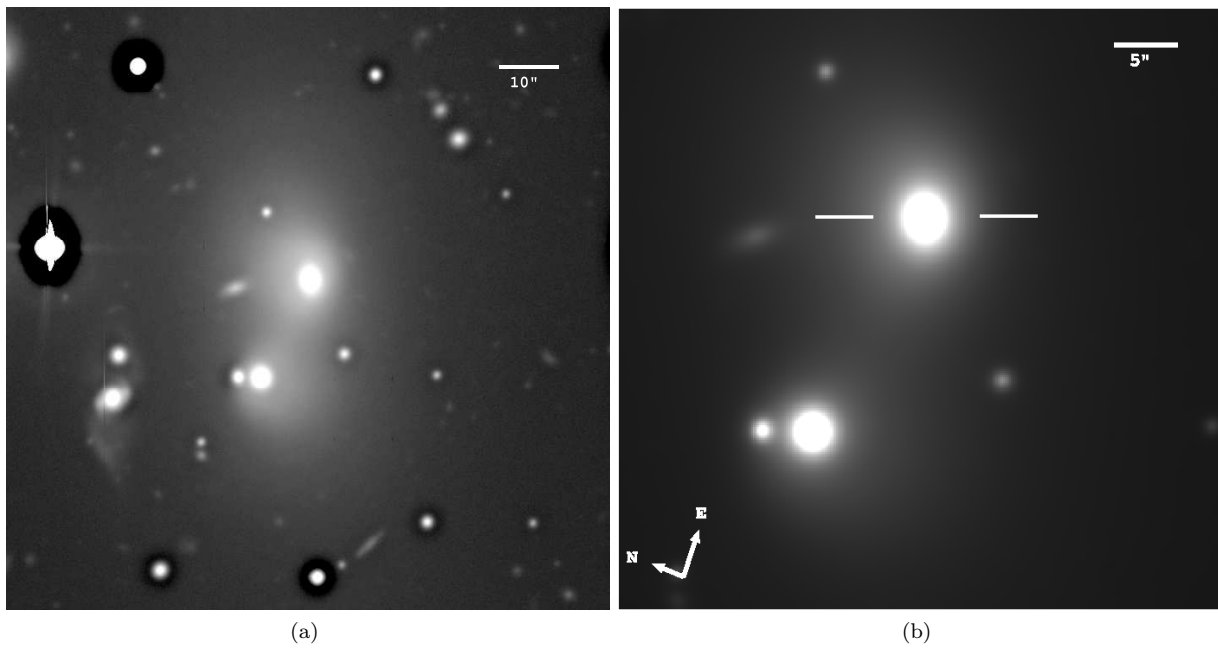


Figure B2. PKS 0625-53. (a) Unsharp-masked image. (b) Median filtered image.

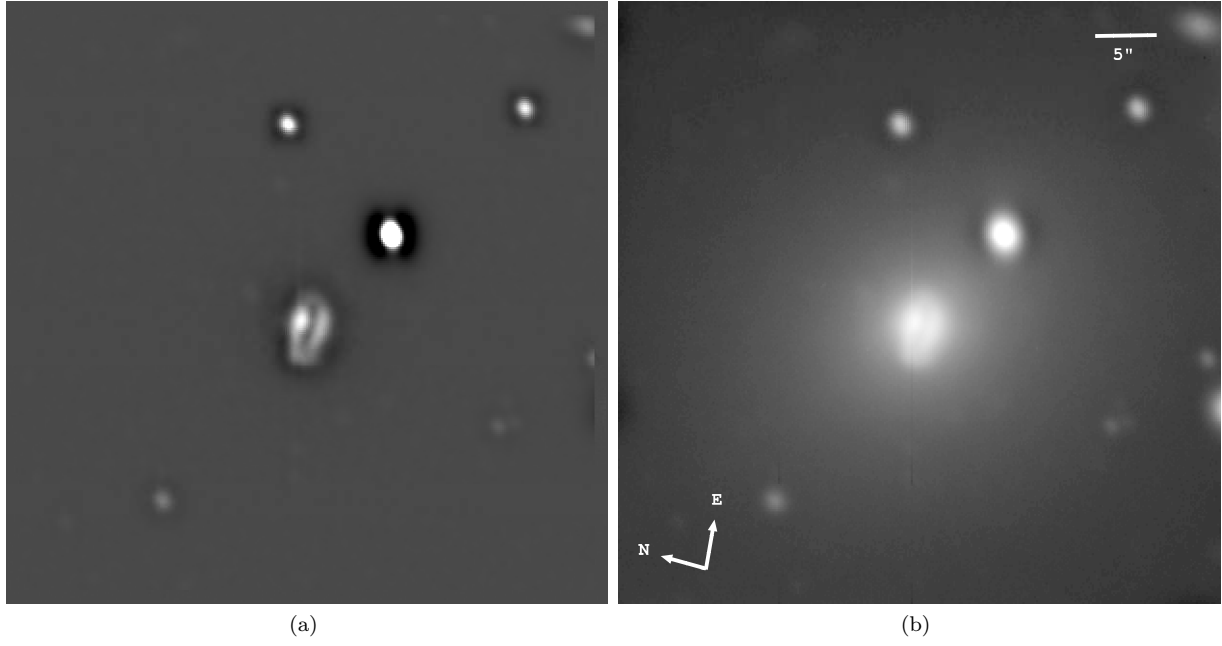


Figure B3. PKS 0915-11. (a) Smooth galaxy-subtracted image. (b) Unsharp-masked image.

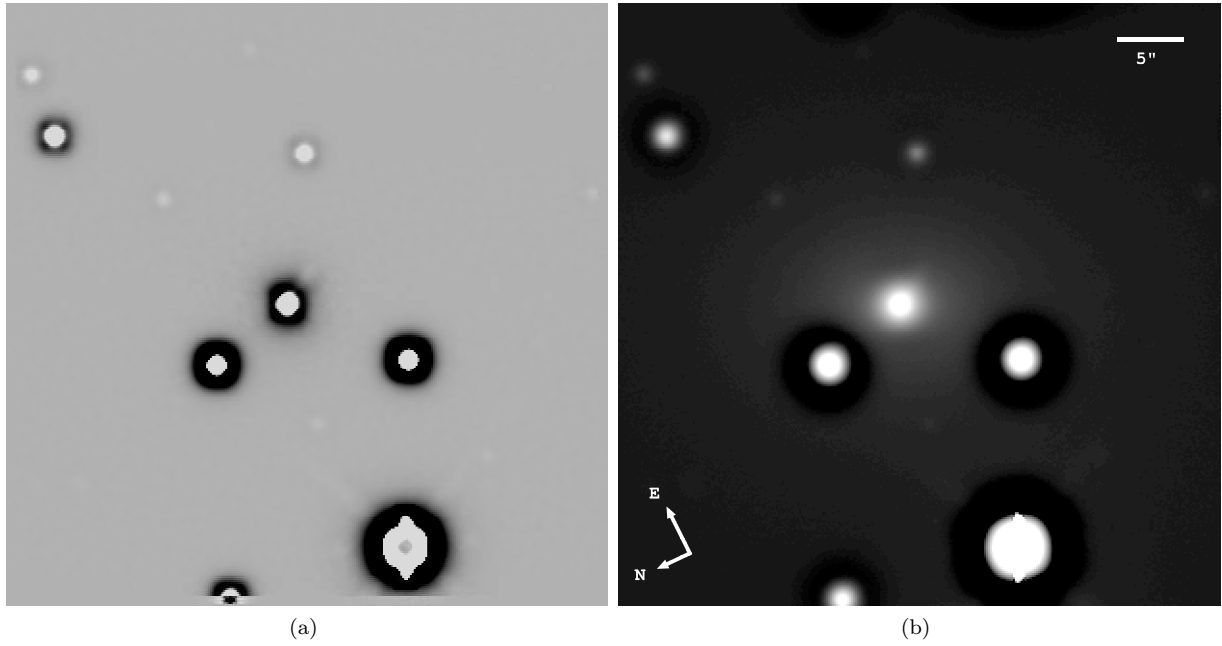


Figure B4. PKS 0625-35. (a) Smooth galaxy-subtracted image. (b) Unsharp-masked image.

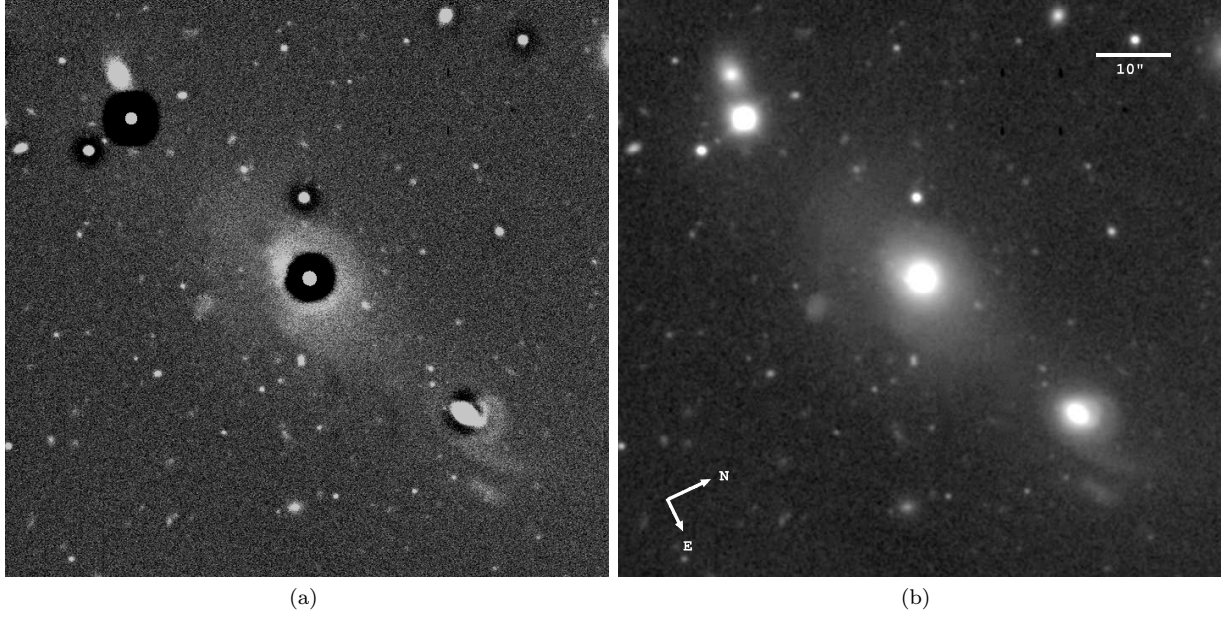


Figure B5. PKS 2221-02. (a) Unsharp-masked image. (b) Median filtered image.

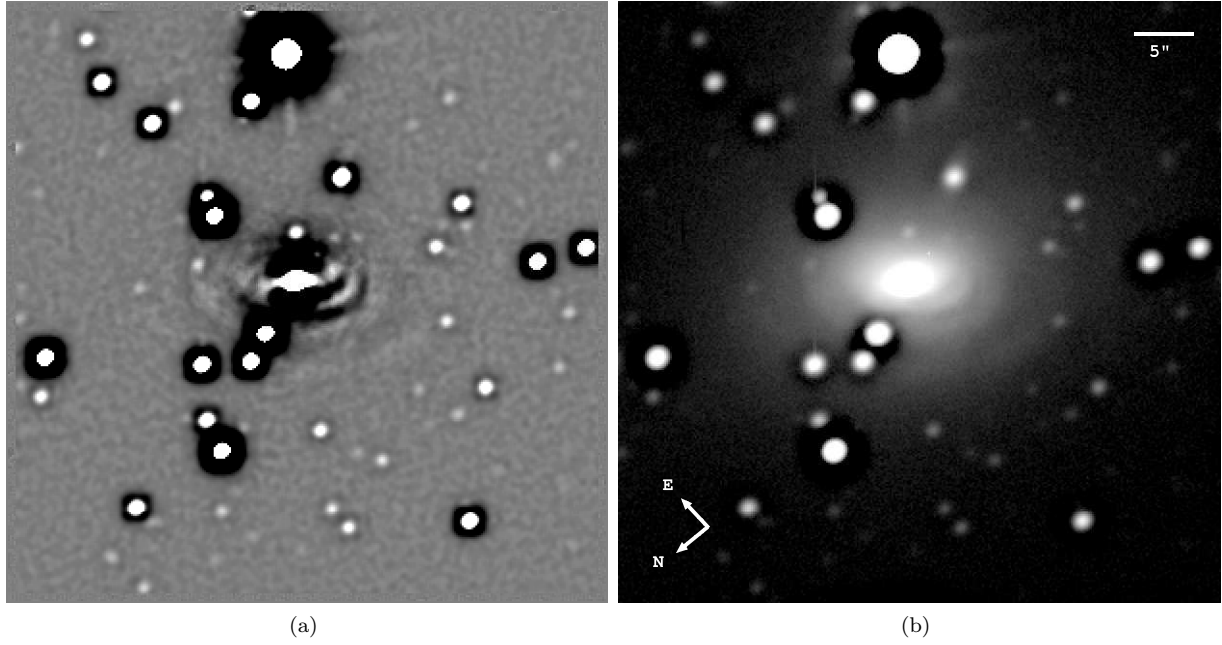


Figure B6. PKS 1949+02. (a) Smooth galaxy-subtracted image. (b) Unsharp-masked image.

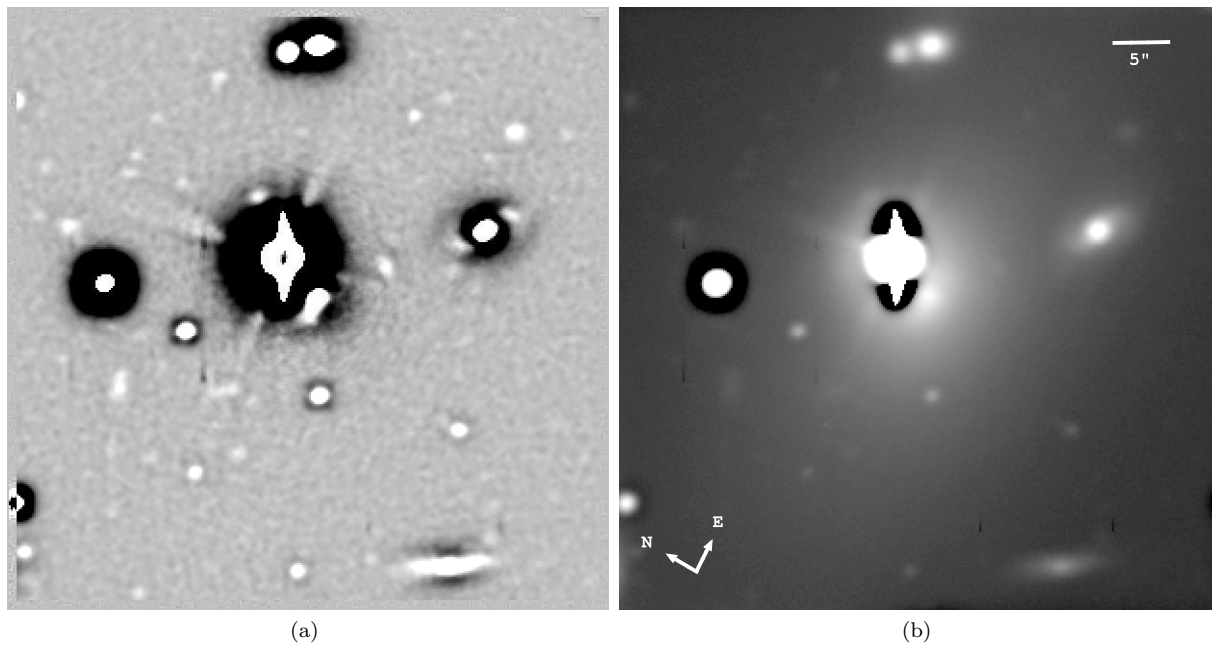


Figure B7. PKS 1954-55. (a) Smooth galaxy-subtracted image. (b) Unsharp-masked image.

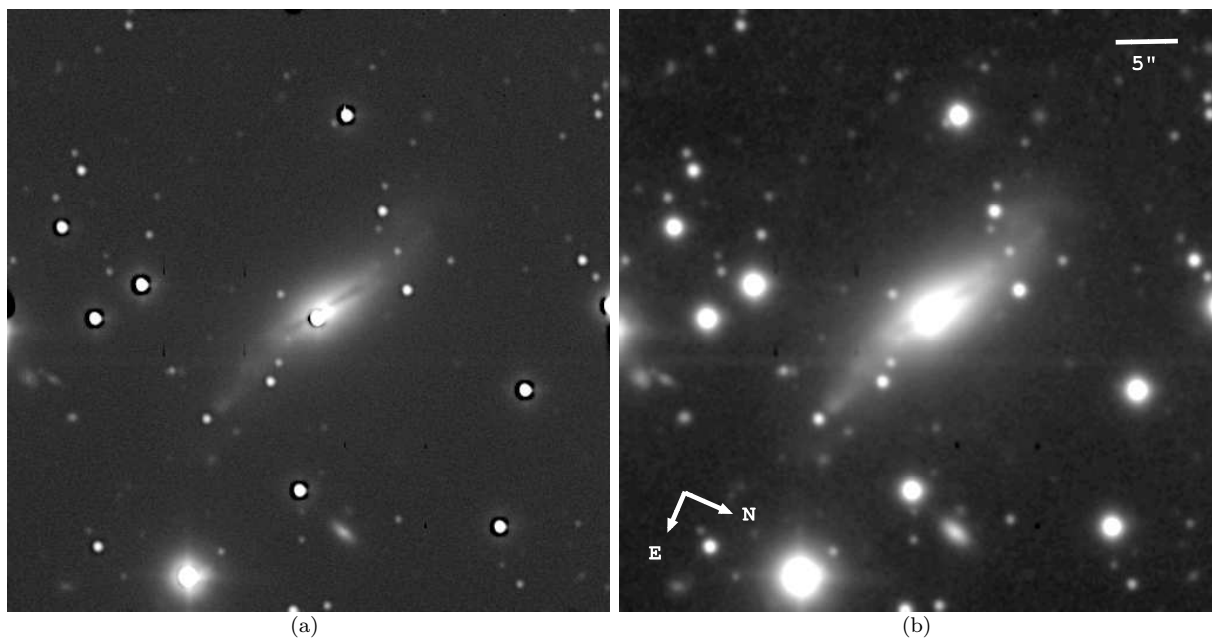


Figure B8. PKS 1814-63. (a) Unsharp-masked image. (b) Median filtered image.

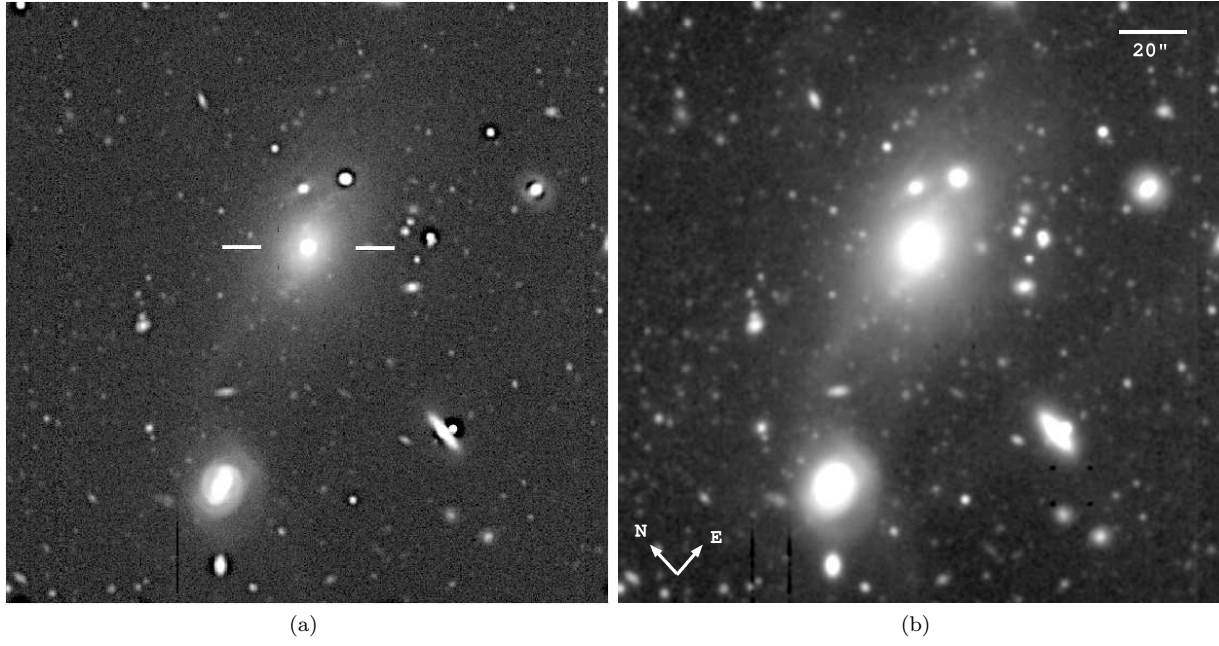


Figure B9. PKS 0349-27. (a) Unsharp-masked image. (b) Median filtered image.

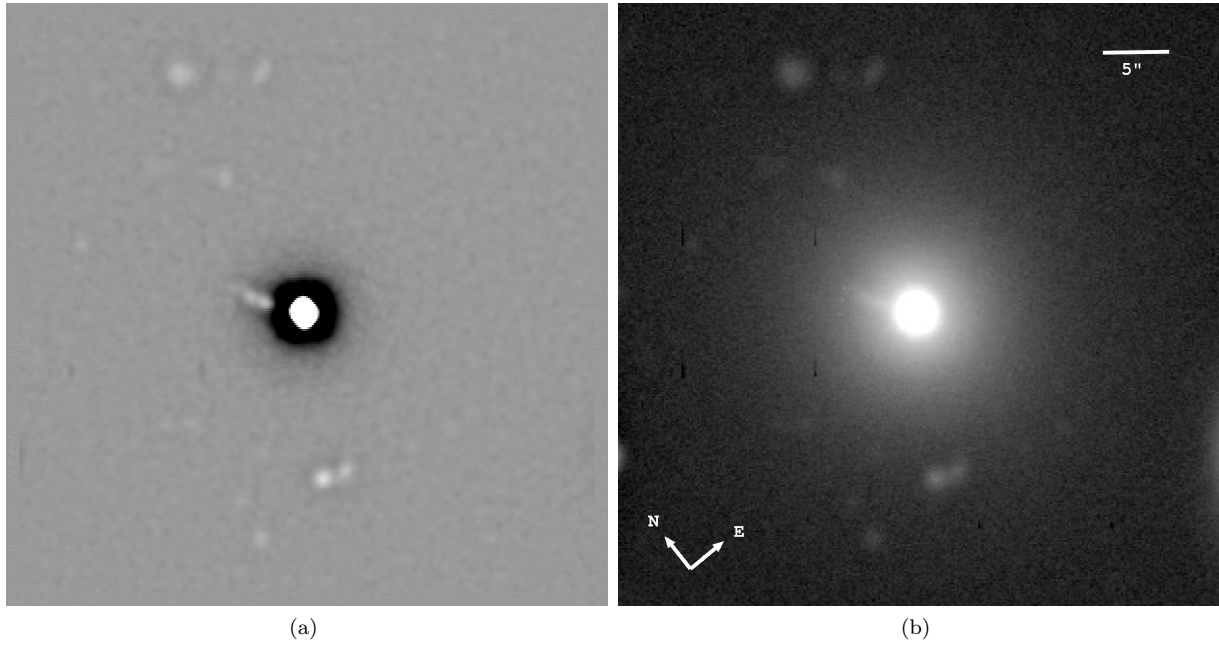


Figure B10. PKS 0034-01. (a) Smooth galaxy-subtracted image. (b) Unsharp-masked image.

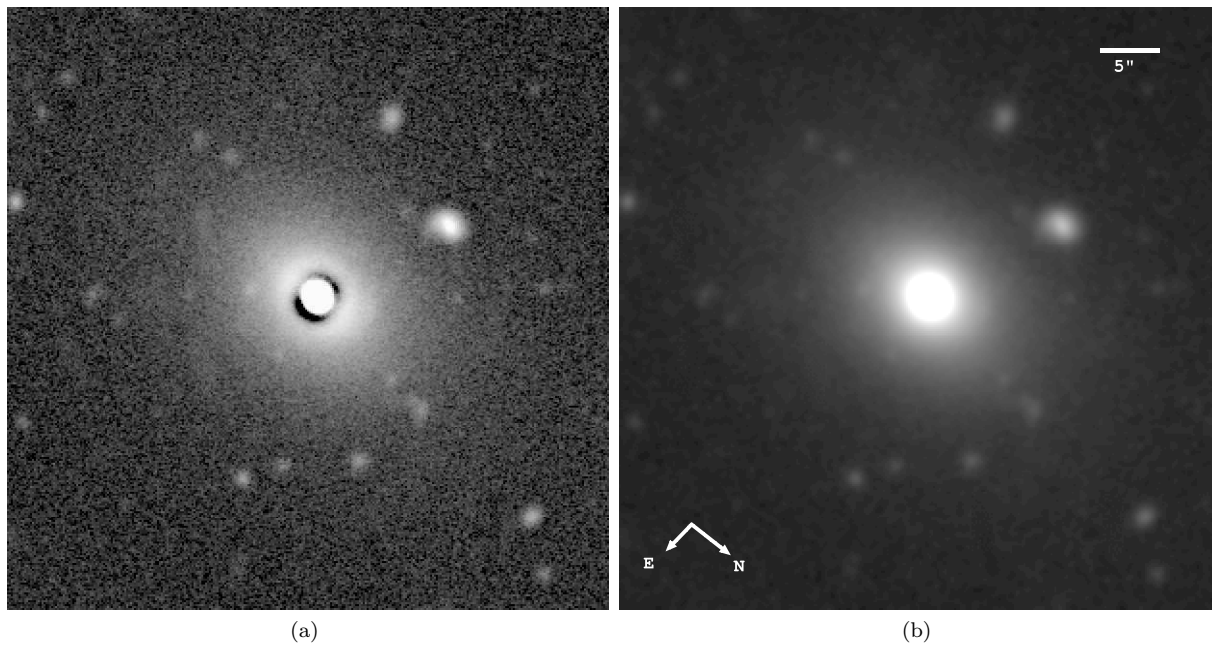


Figure B11. PKS 0945+07. (a) Unsharp-masked image. (b) Median filtered image.

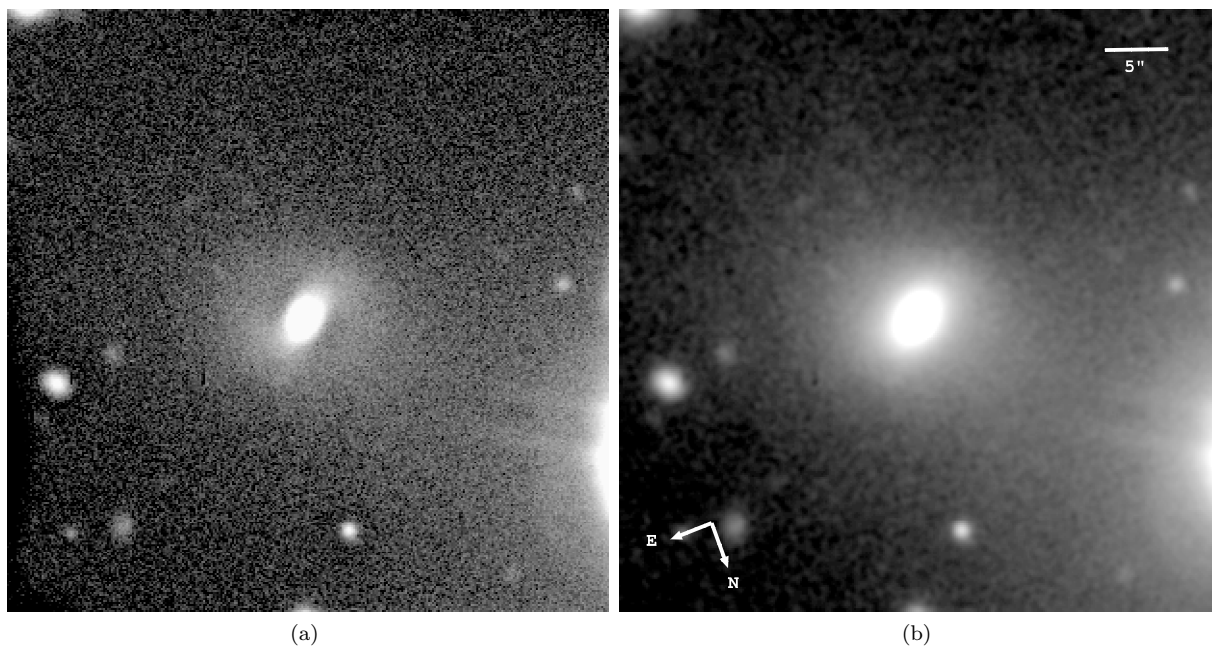


Figure B12. PKS 0404+03. (a) Unsharp-masked image. (b) Median filtered image.

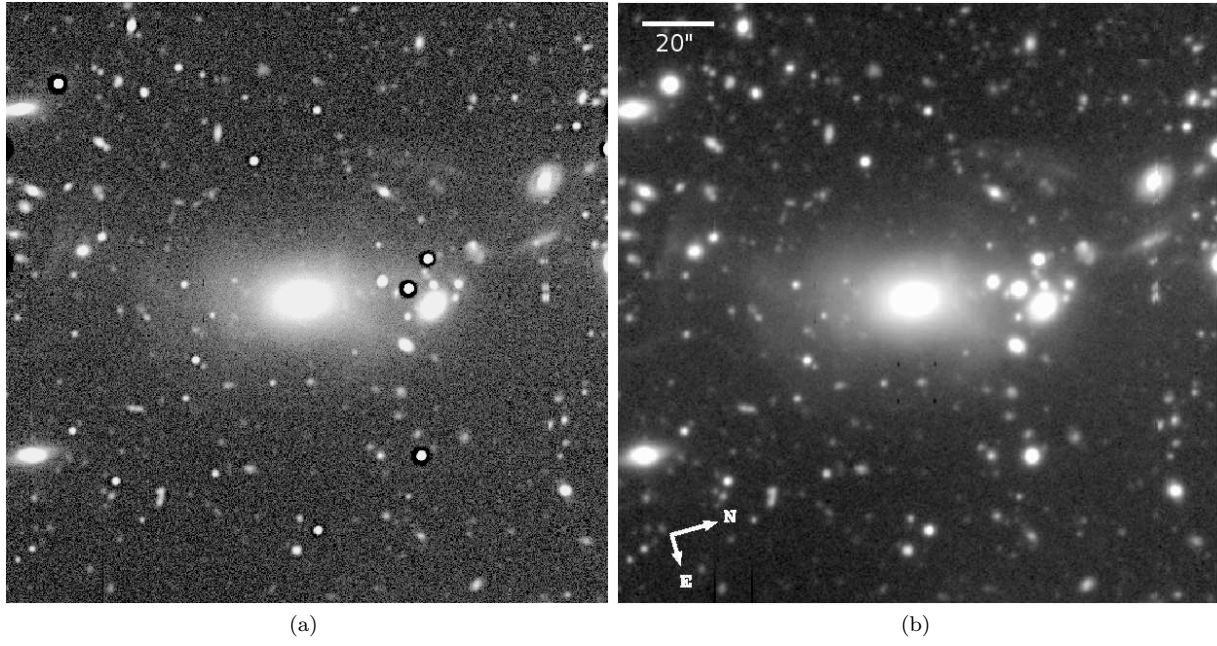


Figure B13. PKS 2356-61. (a) Unsharp-masked image. (b) Median filtered image.

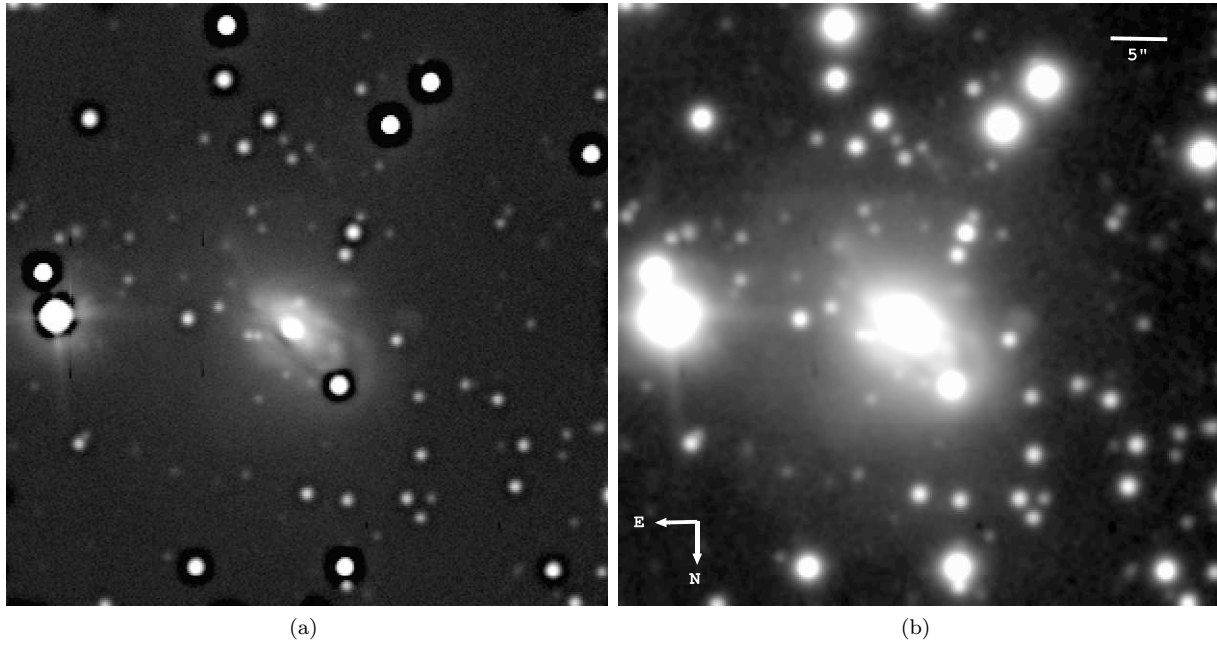


Figure B14. PKS 1733-56. (a) Unsharp-masked image. (b) Median filtered image.

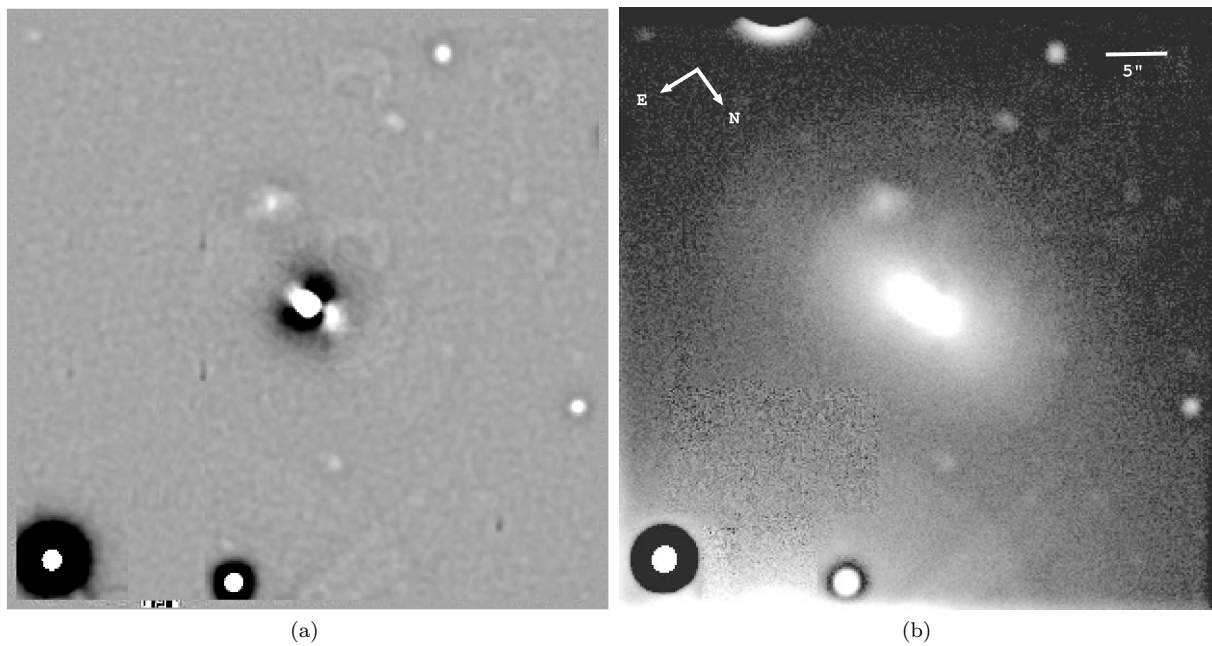


Figure B15. PKS 1559+02. (a) Smooth galaxy-subtracted image. (b) Unsharp-masked image.

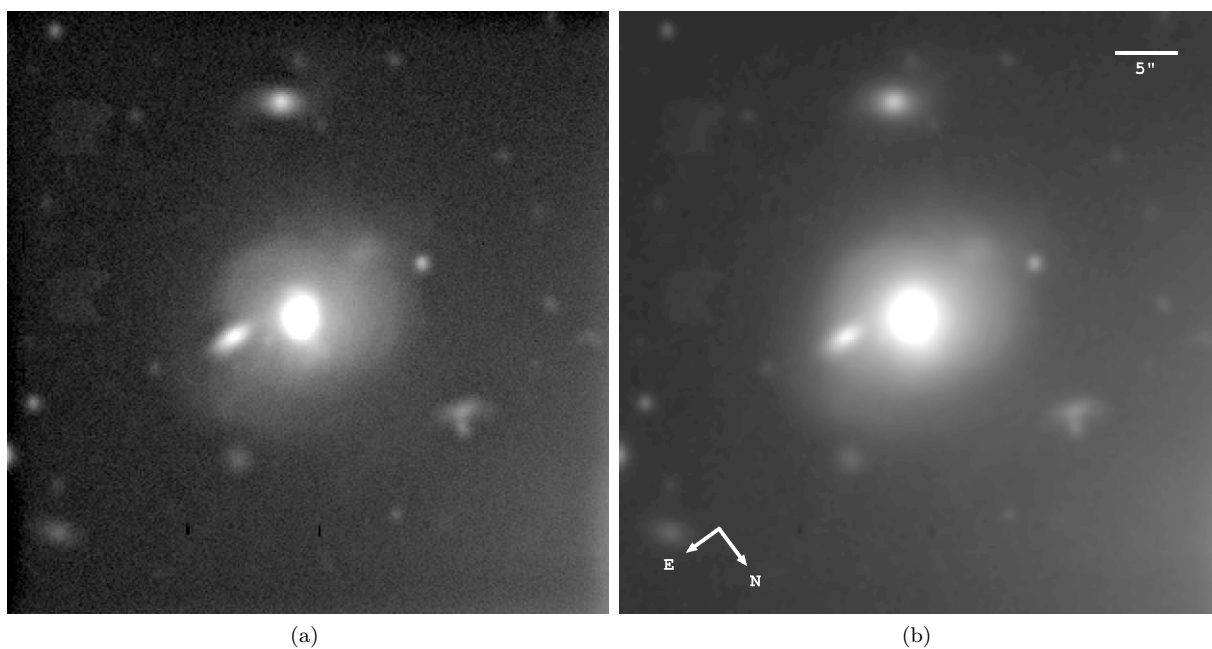


Figure B16. PKS 0806-10. (a) Unsharp-masked image. (b) Median filtered image.

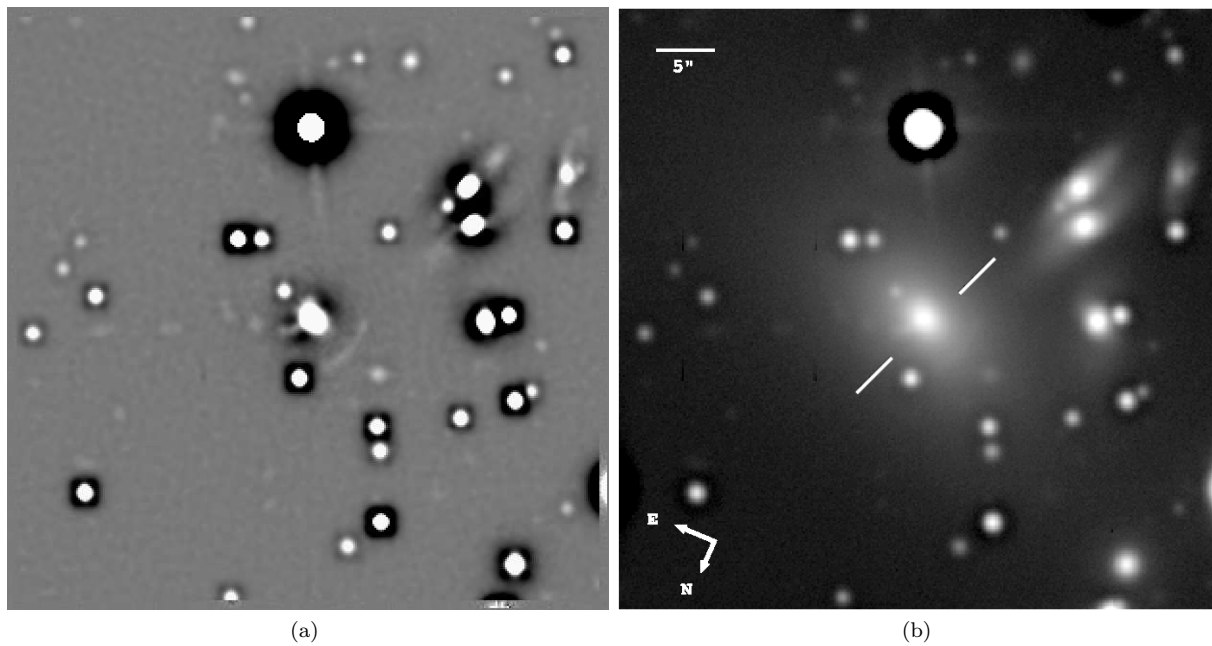


Figure B17. PKS 1839-48. (a) Smooth galaxy-subtracted image. (b) Unsharp-masked image.

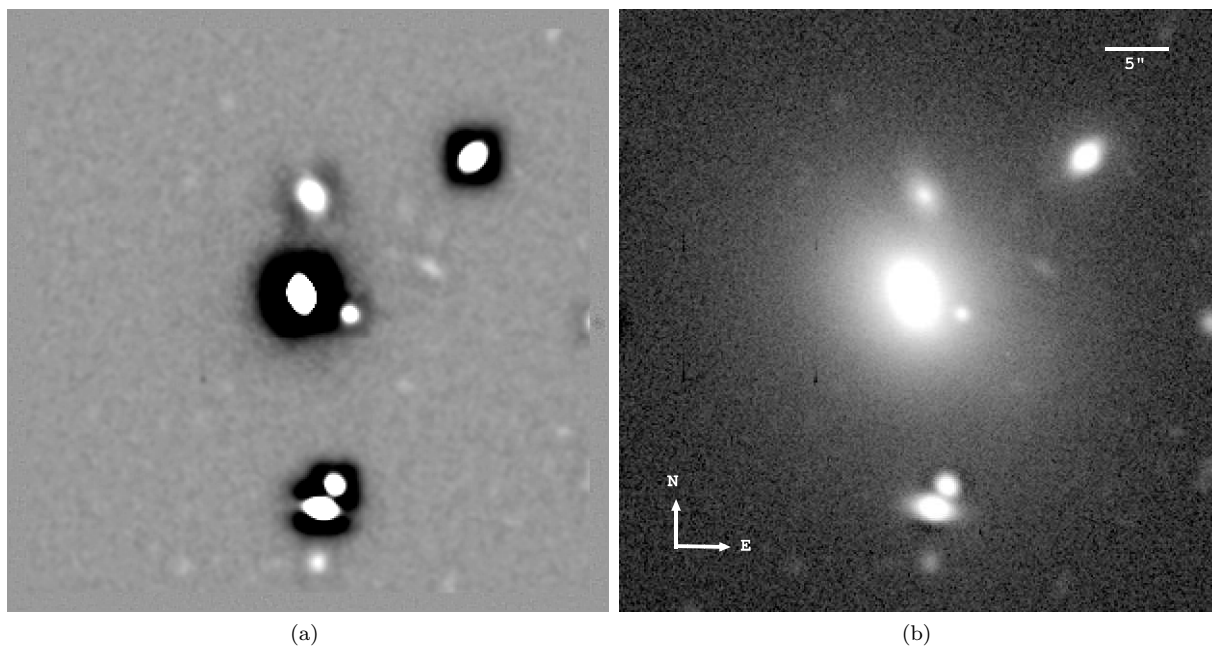


Figure B18. PKS 0043-42. (a) Smooth galaxy-subtracted image. (b) Unsharp-masked image.

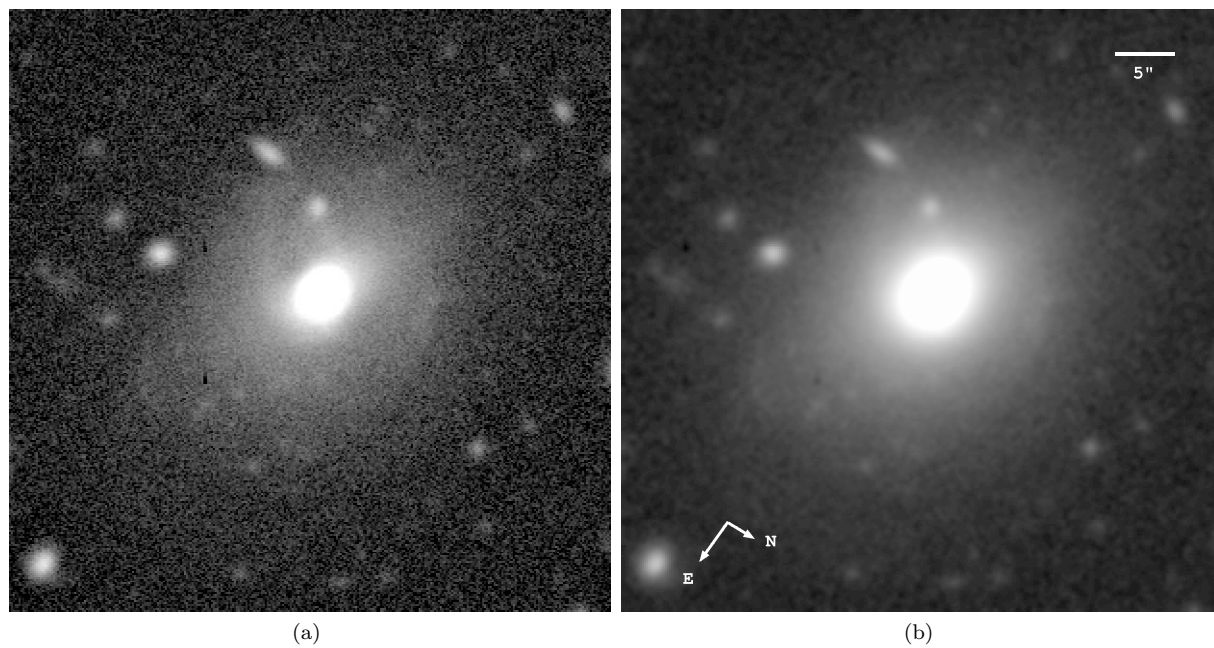


Figure B19. PKS 0213-13. (a) Unsharp-masked image. (b) Median filtered image.

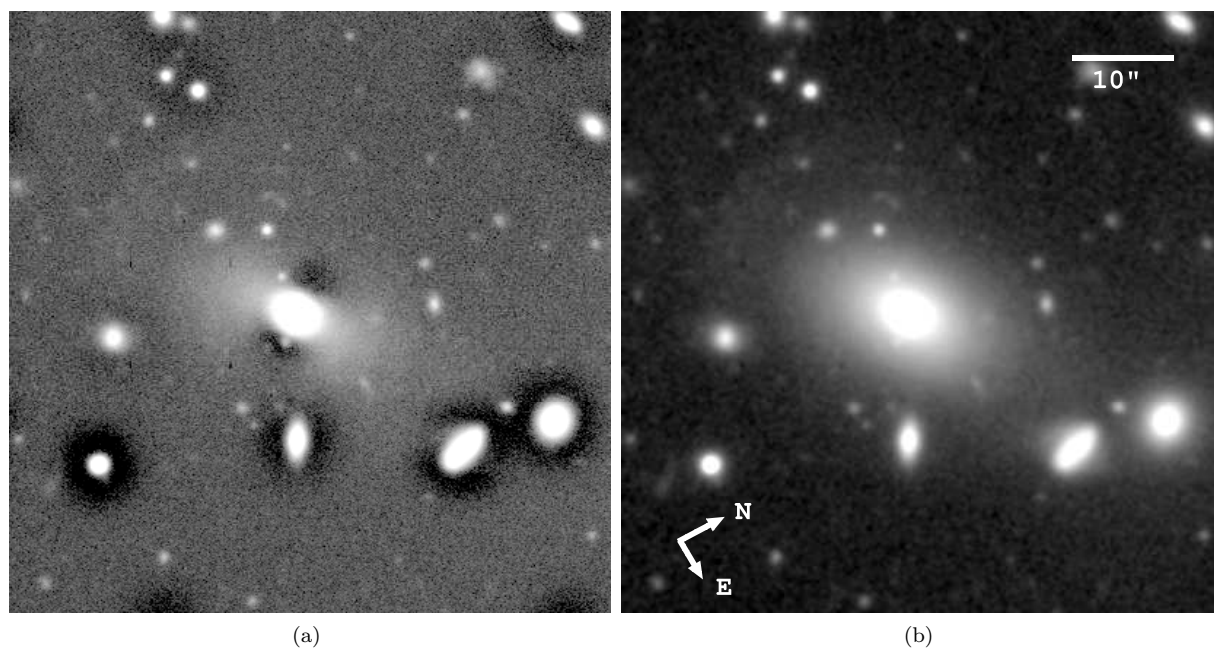


Figure B20. PKS 0442-28. (a) Unsharp-masked image. (b) Median filtered image.

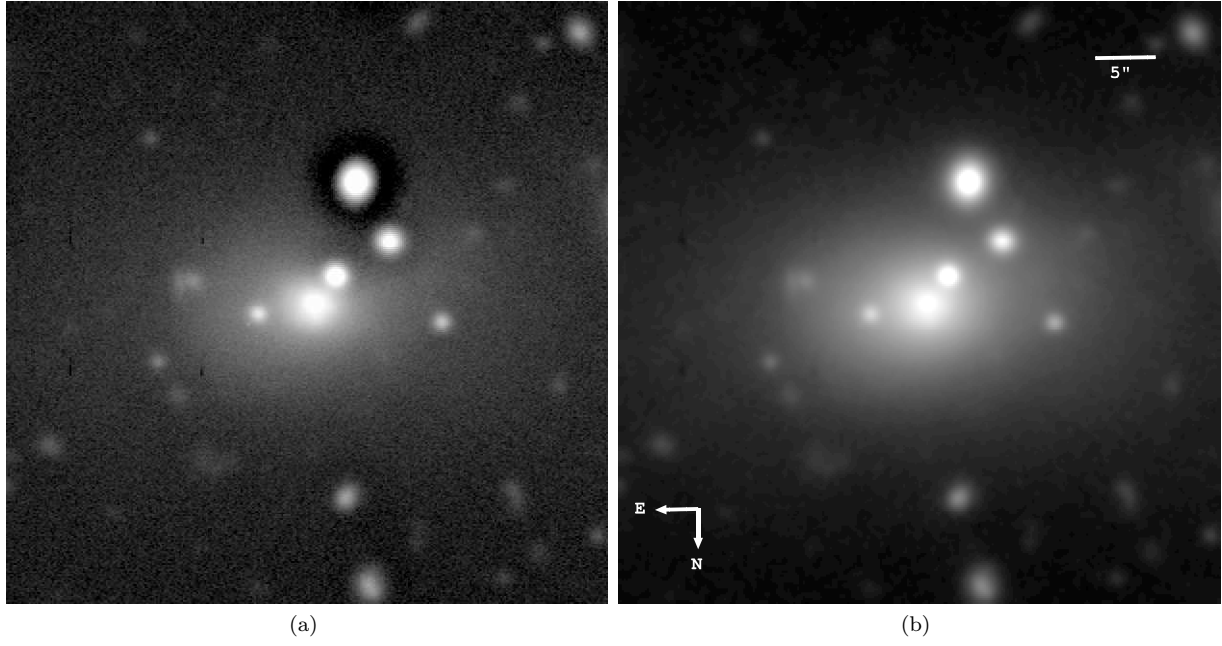


Figure B21. PKS 2211-17. (a) Unsharp-masked image. (b) Median filtered image.

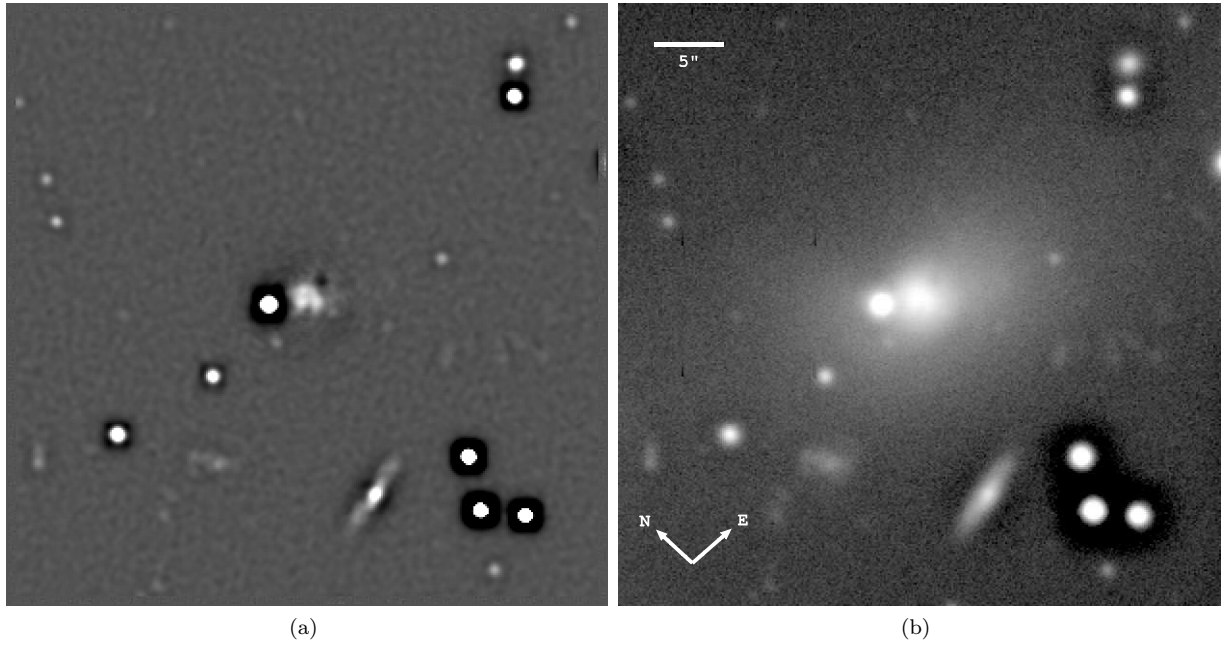


Figure B22. PKS 1648+05. (a) Smooth galaxy-subtracted image. (b) Unsharp-masked image.

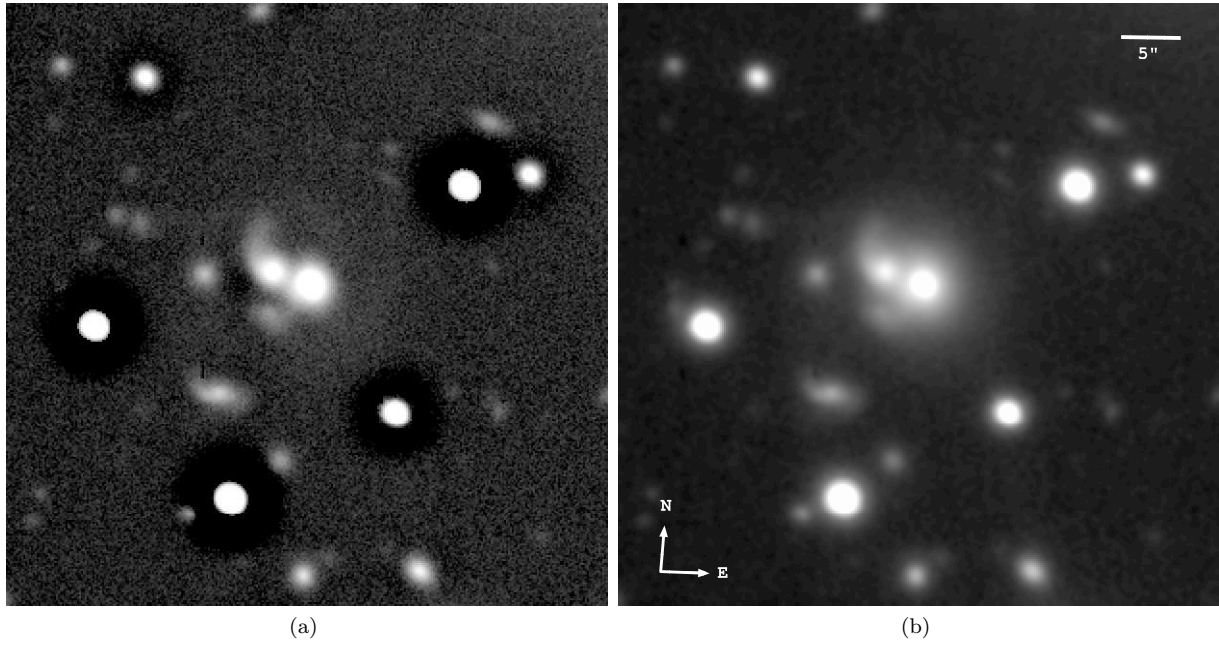


Figure B23. PKS 1934-63. (a) Unsharp-masked image. (b) Median filtered image.

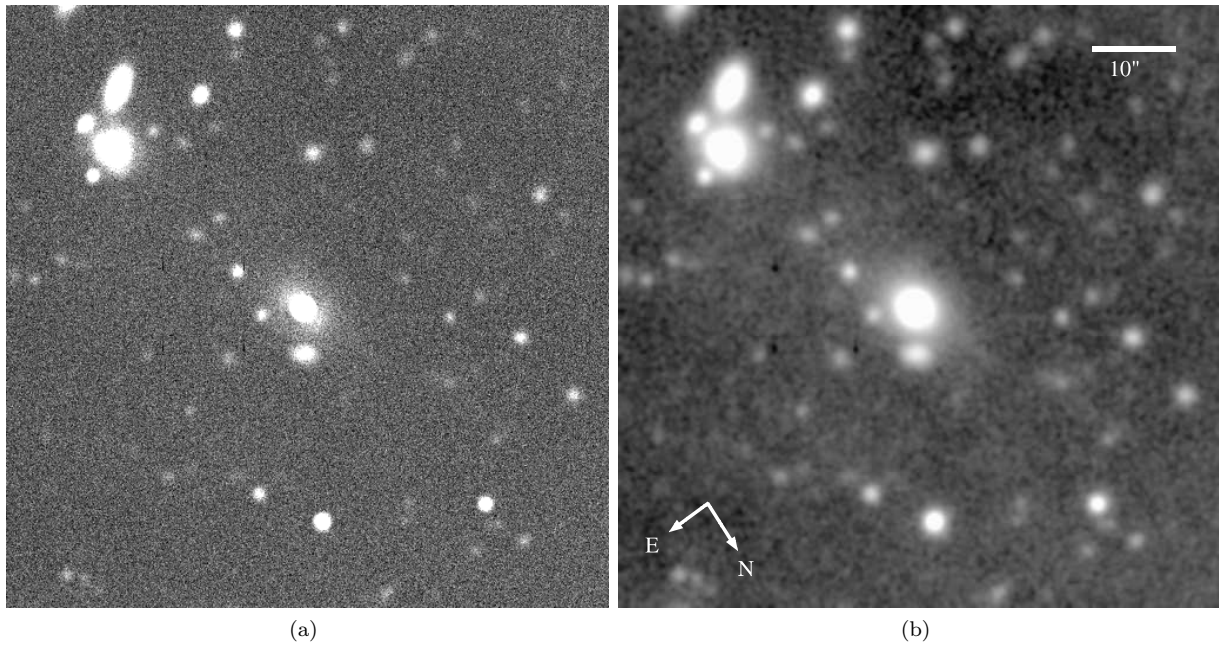


Figure B24. PKS 0038+09. (a) Unsharp-masked image. (b) Median filtered image.

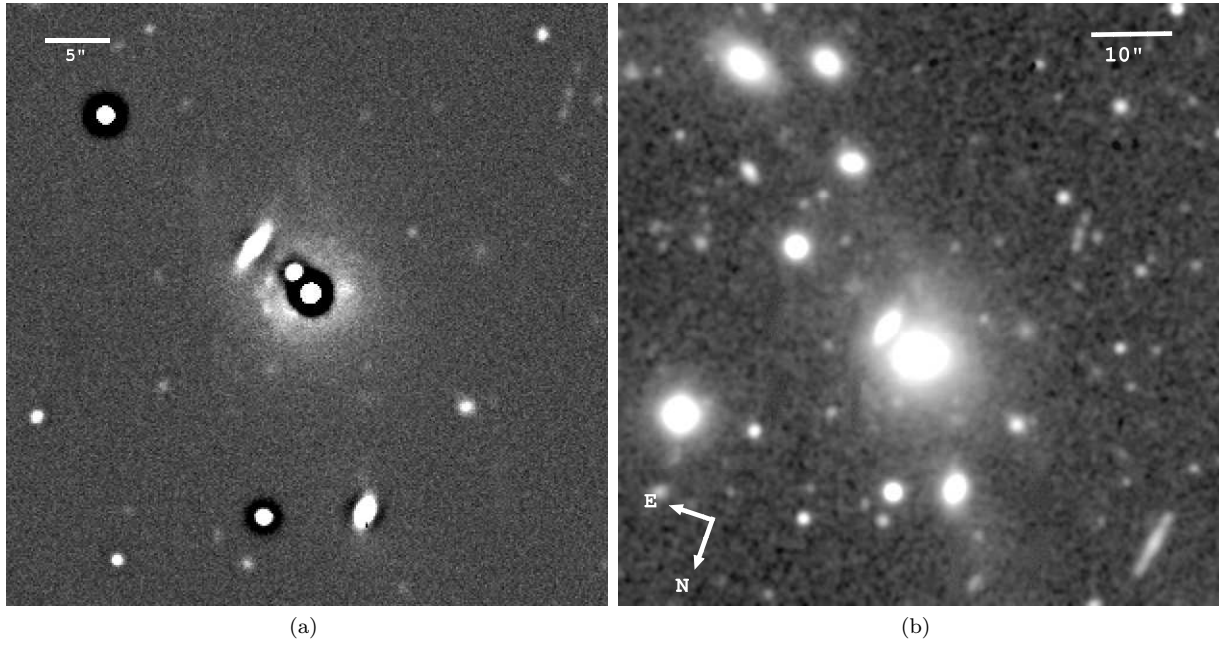


Figure B25. PKS 2135-14. (a) Unsharp-masked image. (b) Median filtered image.

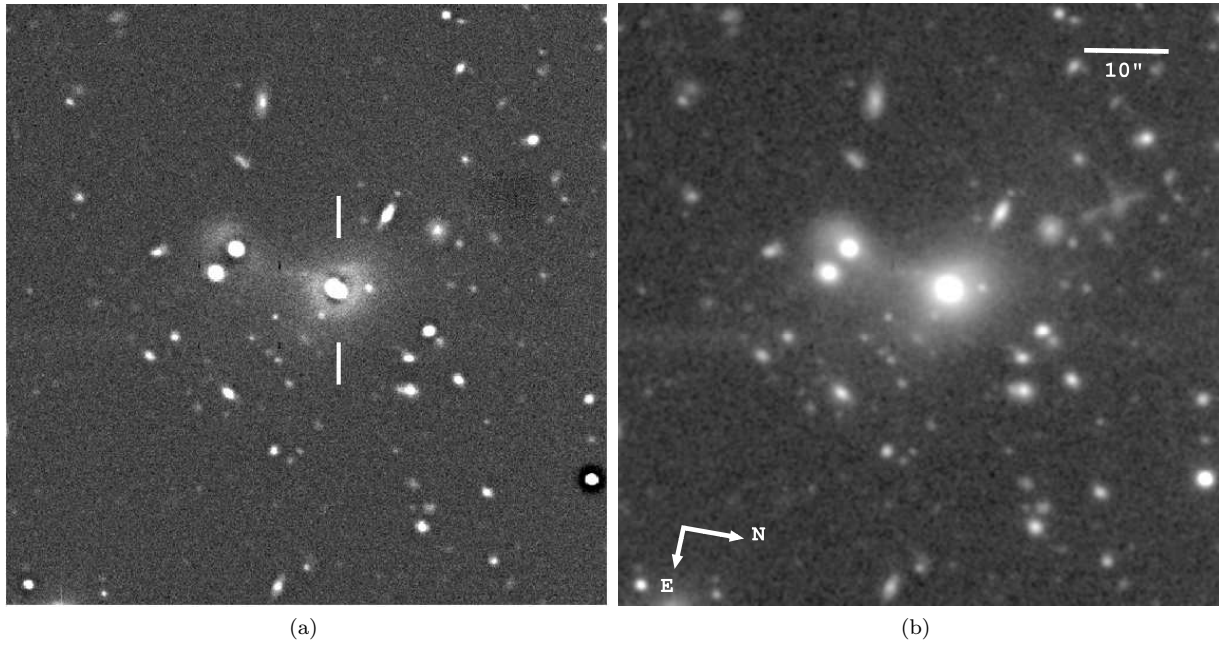


Figure B26. PKS 0035-02. (a) Unsharp-masked image. (b) Median filtered image.

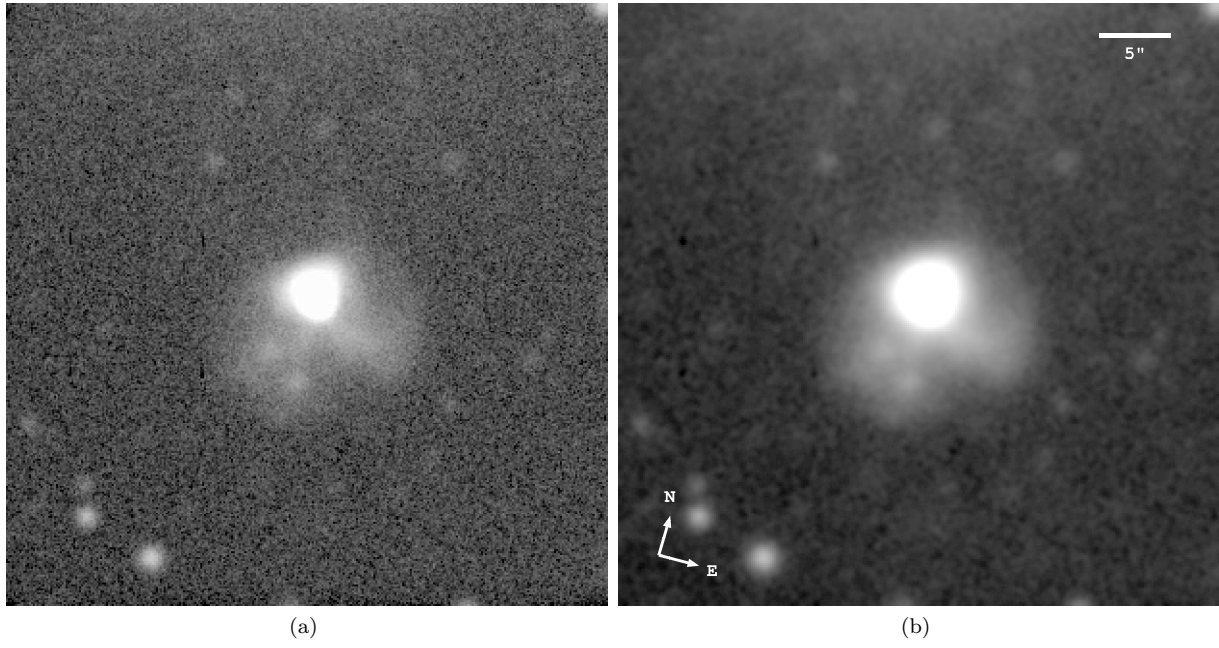


Figure B27. PKS 2314+03. (a) Unsharp-masked image. (b) Median filtered image.

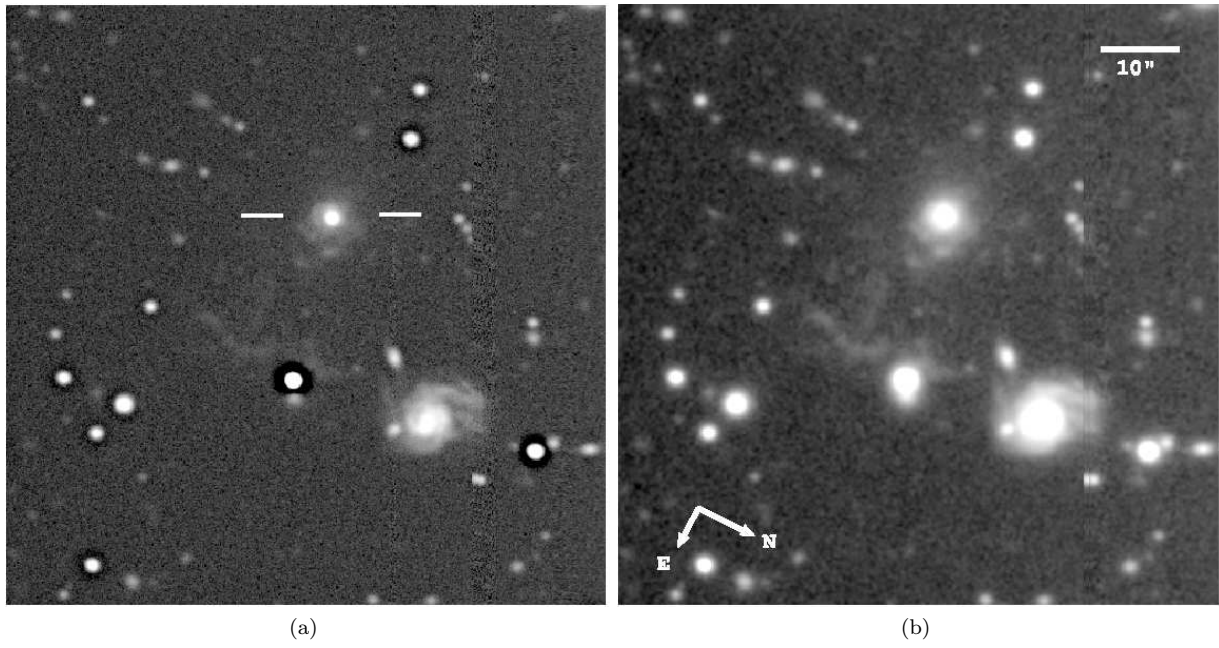


Figure B28. PKS 1932-46. (a) Unsharp-masked image. (b) Median filtered image.

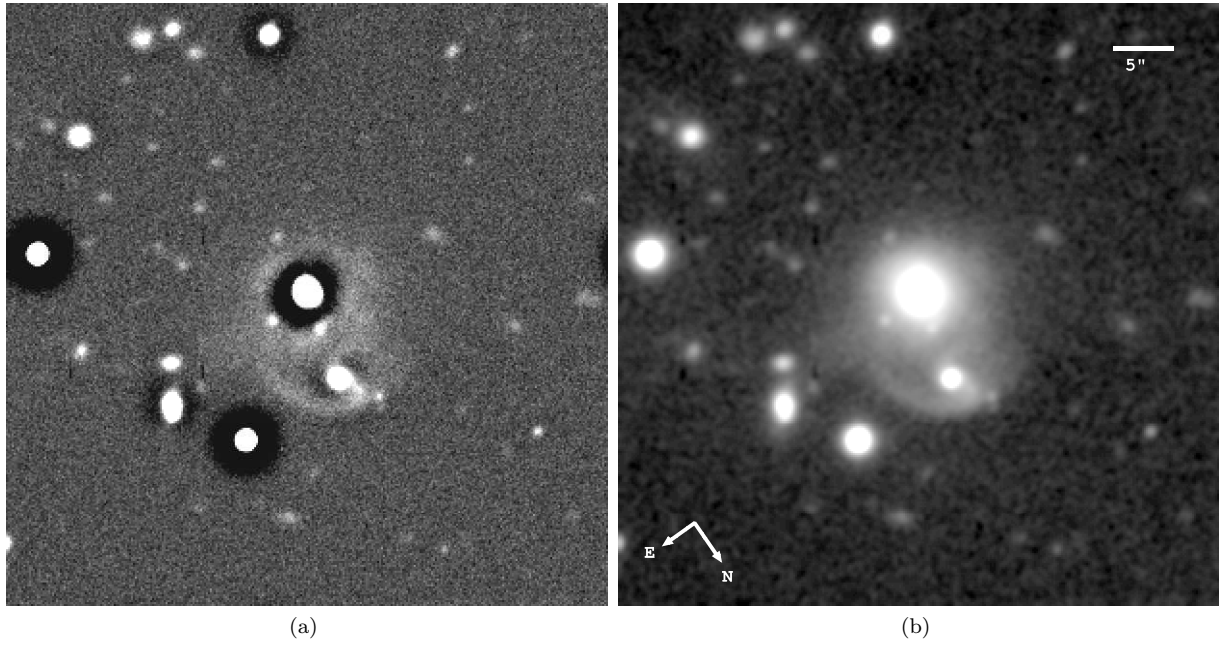


Figure B29. PKS 1151-34. (a) Unsharp-masked image. (b) Median filtered image.

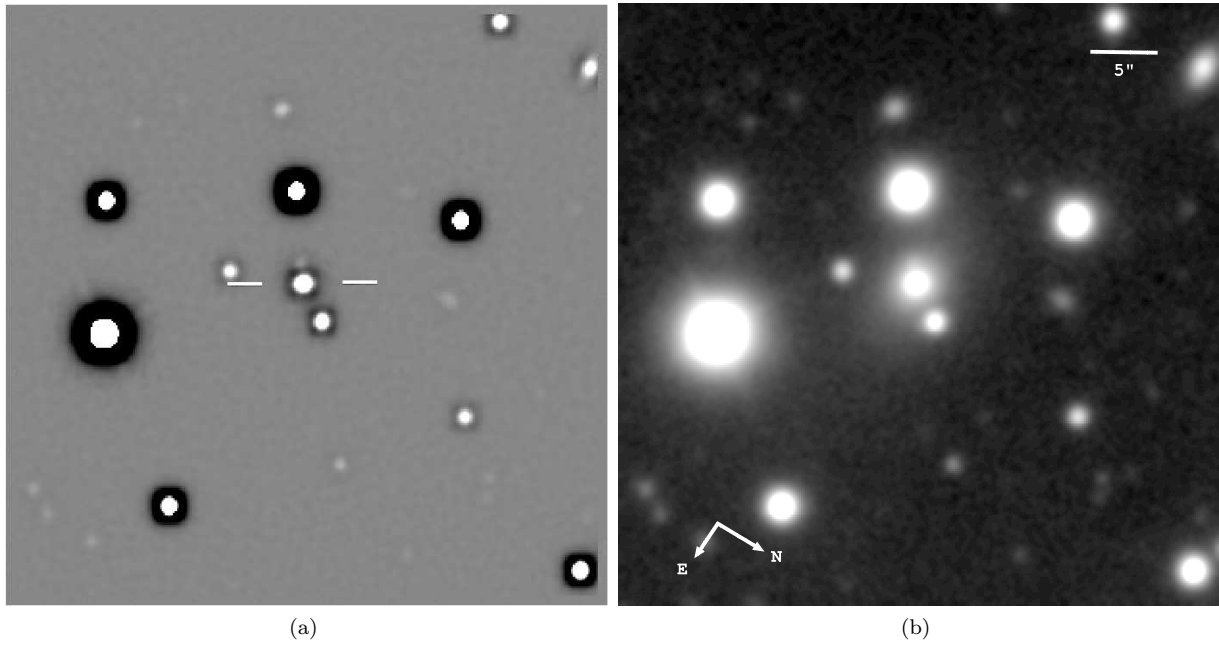


Figure B30. PKS 0859-25. (a) Smooth galaxy-subtracted image. (b) Median filtered image.

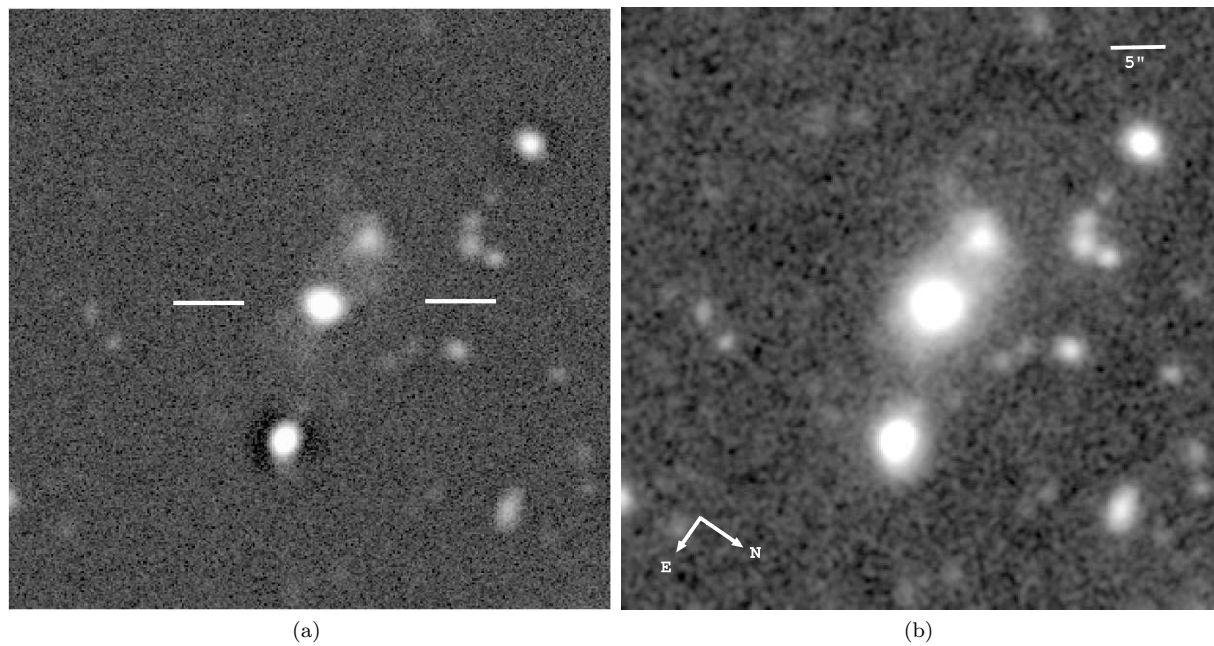


Figure B31. PKS 2250-41. (a) Unsharp-masked image. (b) Median filtered image.

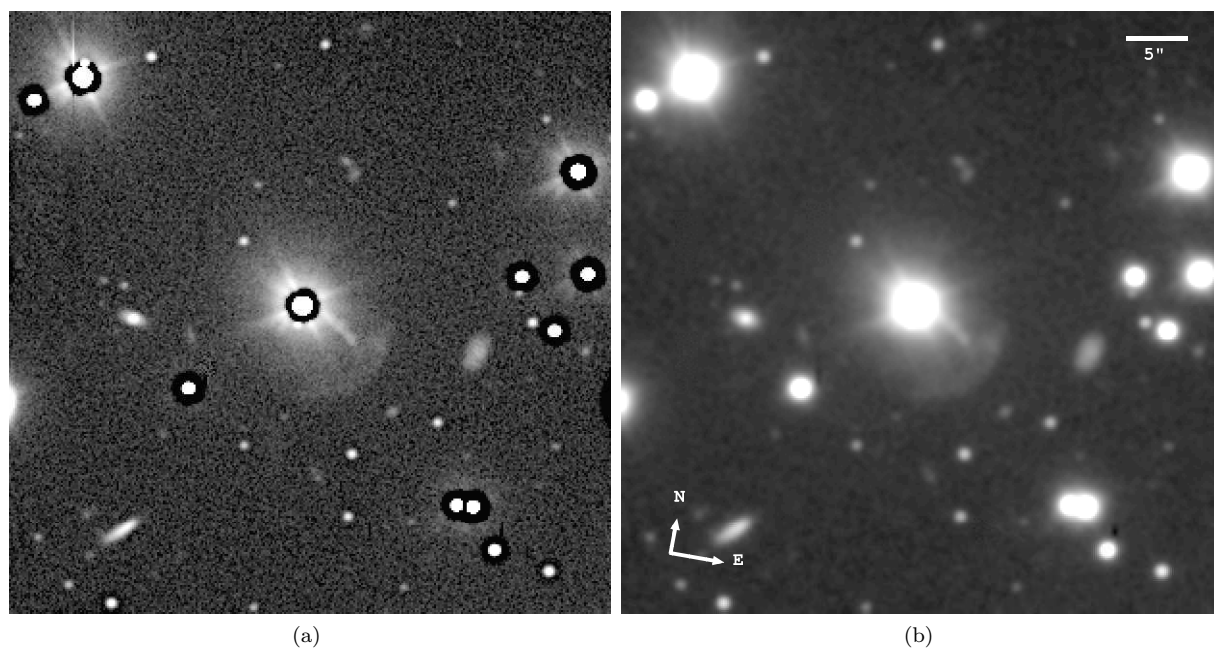


Figure B32. PKS 1355-41. (a) Unsharp-masked image. (b) Median filtered image.

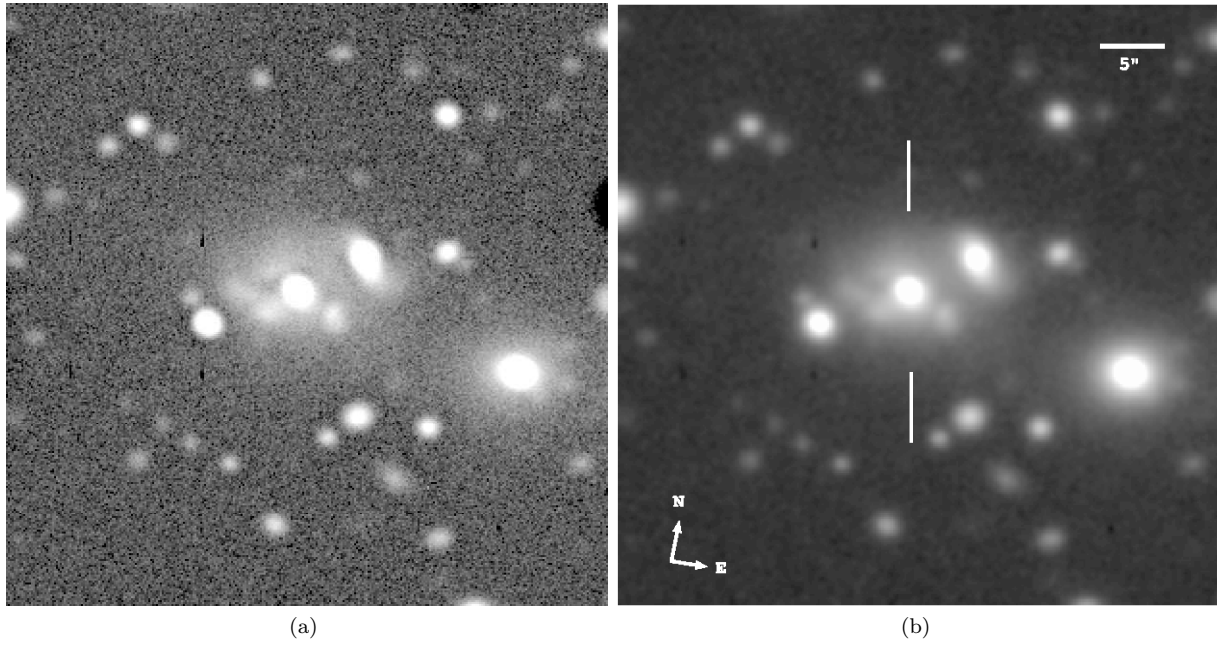


Figure B33. PKS 0023-26. (a) Unsharp-masked image. (b) Median filtered image.

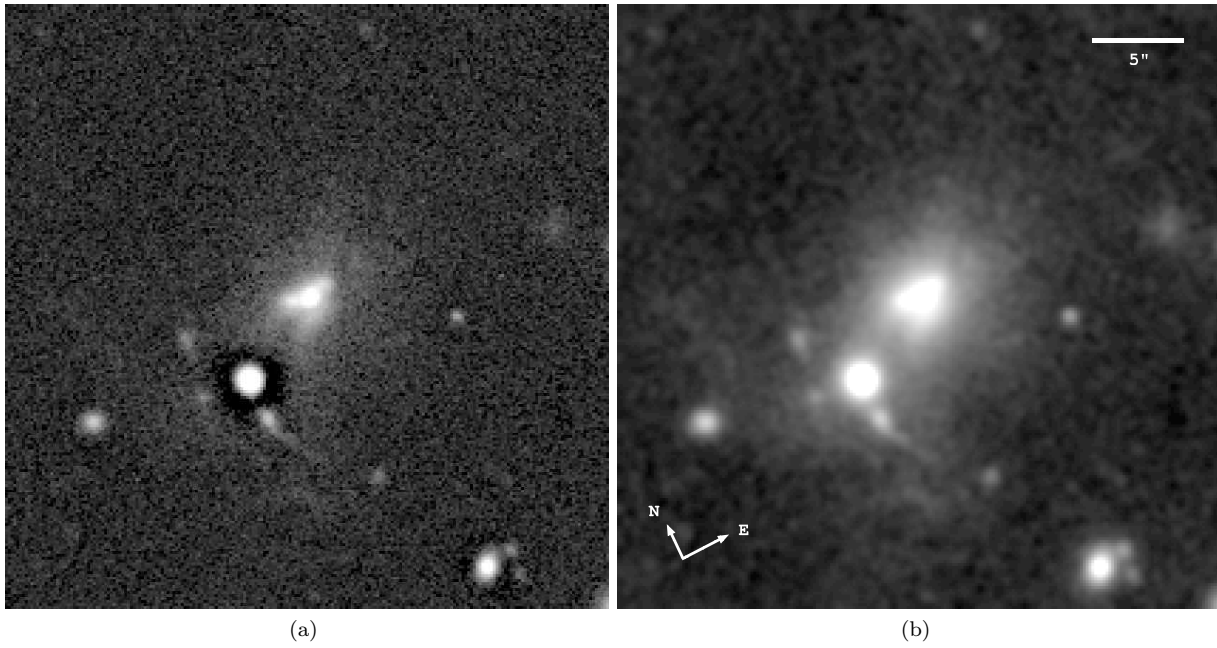


Figure B34. PKS 0347+05. (a) Unsharp-masked image. (b) Median filtered image.

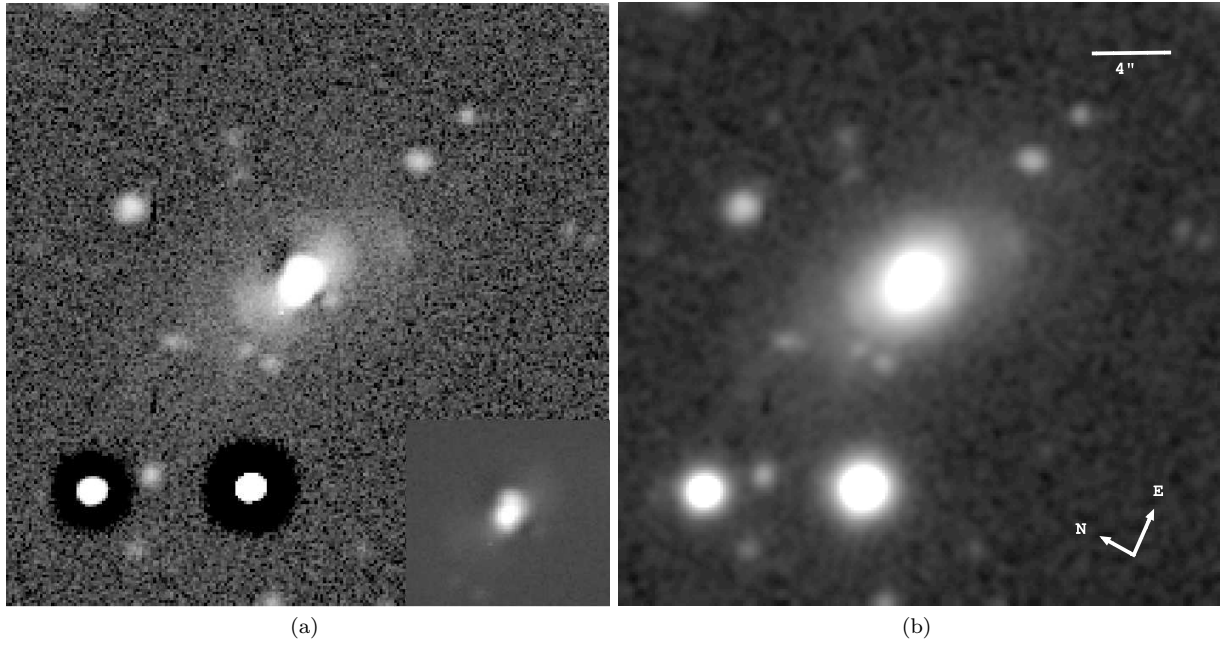


Figure B35. PKS 0039-44. (a) Unsharp-masked image. (b) Median filtered image.

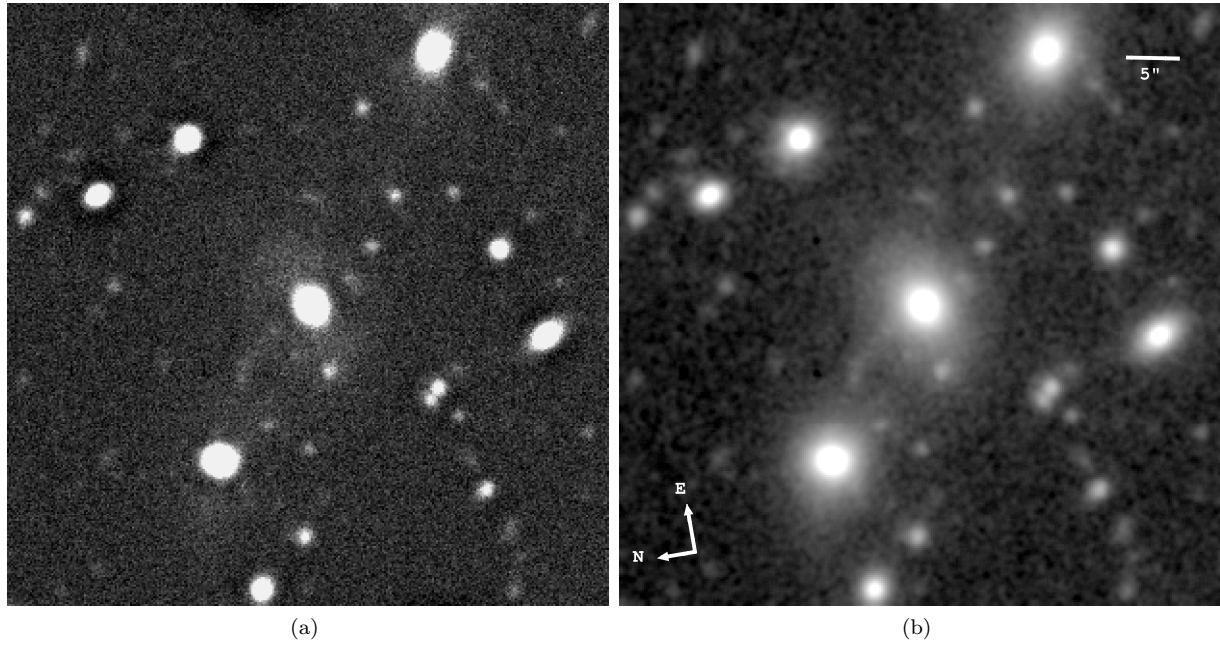


Figure B36. PKS 0105-16. (a) Unsharp-masked image. (b) Median filtered image.

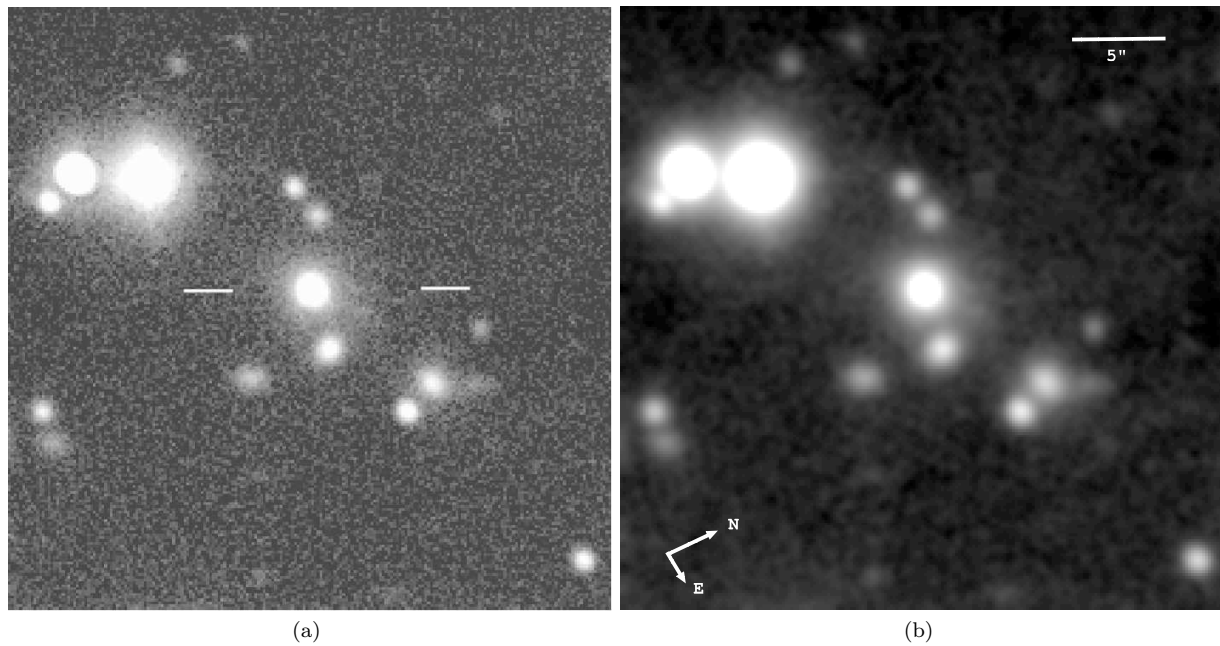


Figure B37. PKS 1938-15. (a) Unsharp-masked image. (b) Median filtered image.

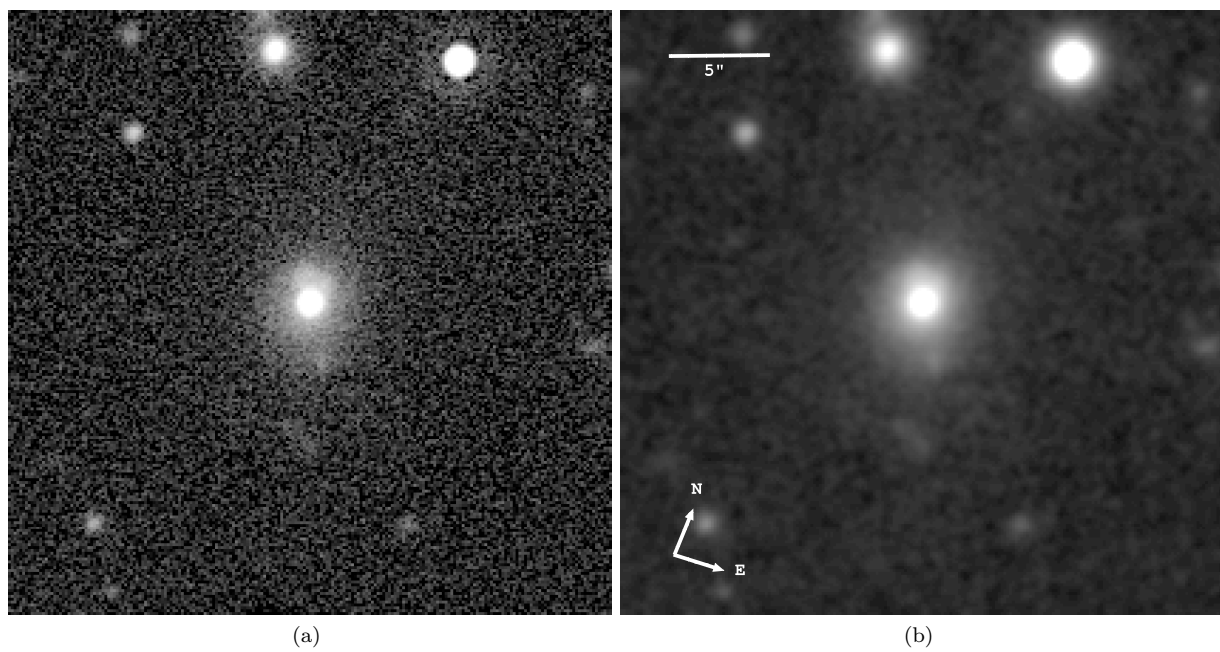


Figure B38. PKS 1602+01. (a) Unsharp-masked image. (b) Median filtered image.

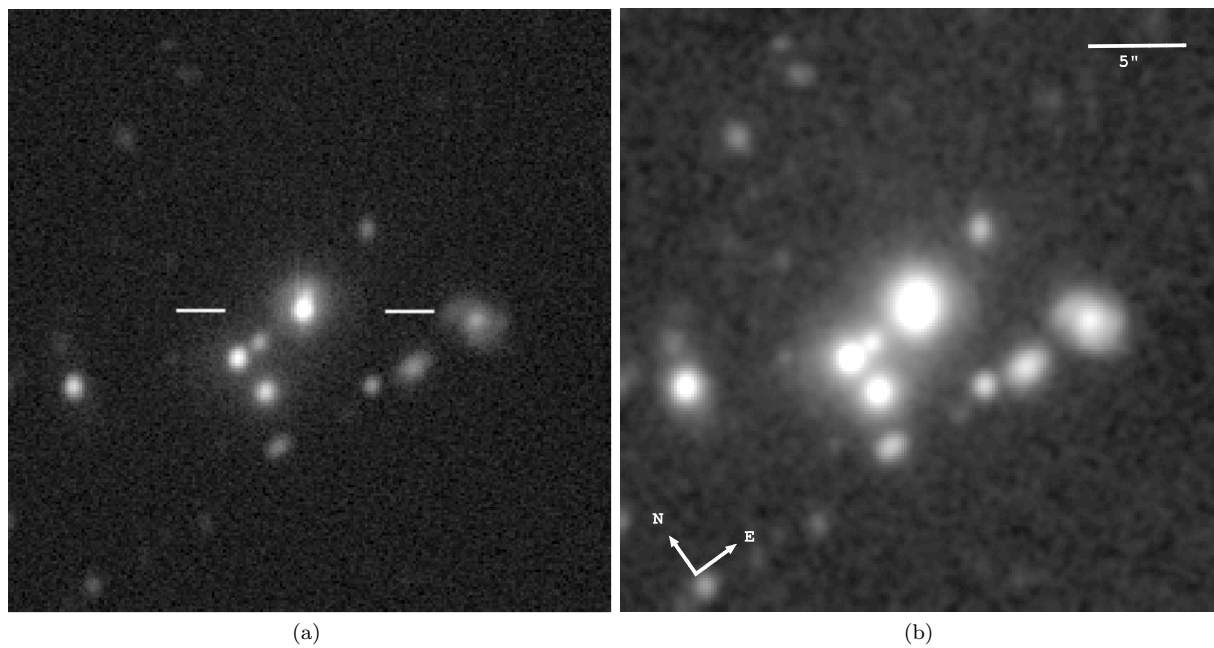


Figure B39. PKS 1306-09. (a) Unsharp-masked image. (b) Median filtered image.

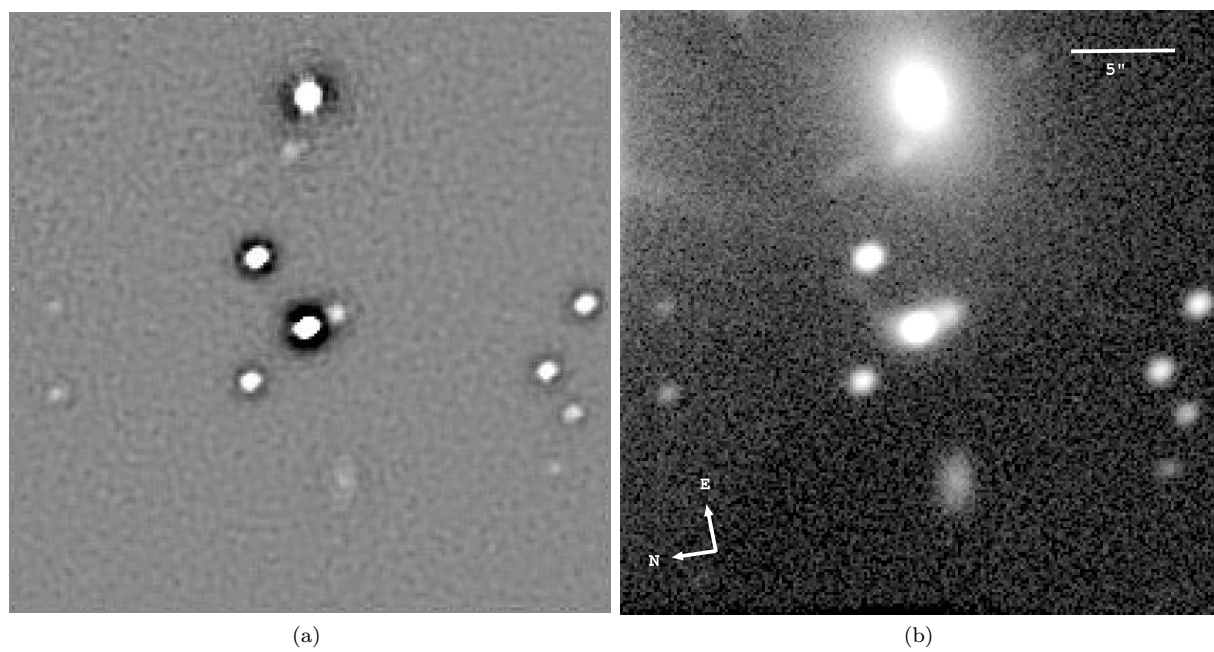


Figure B40. PKS 1547-79. (a) Smooth galaxy-subtracted image. (b) Unsharp-masked image.

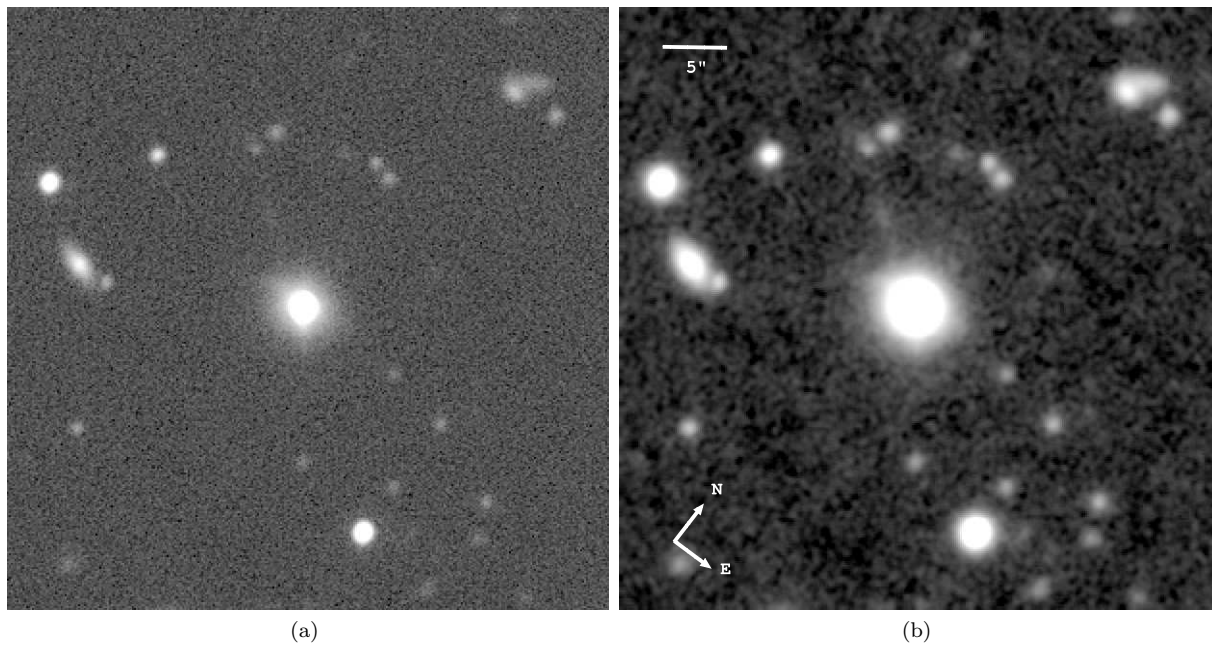


Figure B41. PKS 1136-13. (a) Unsharp-masked image. (b) Median filtered image.

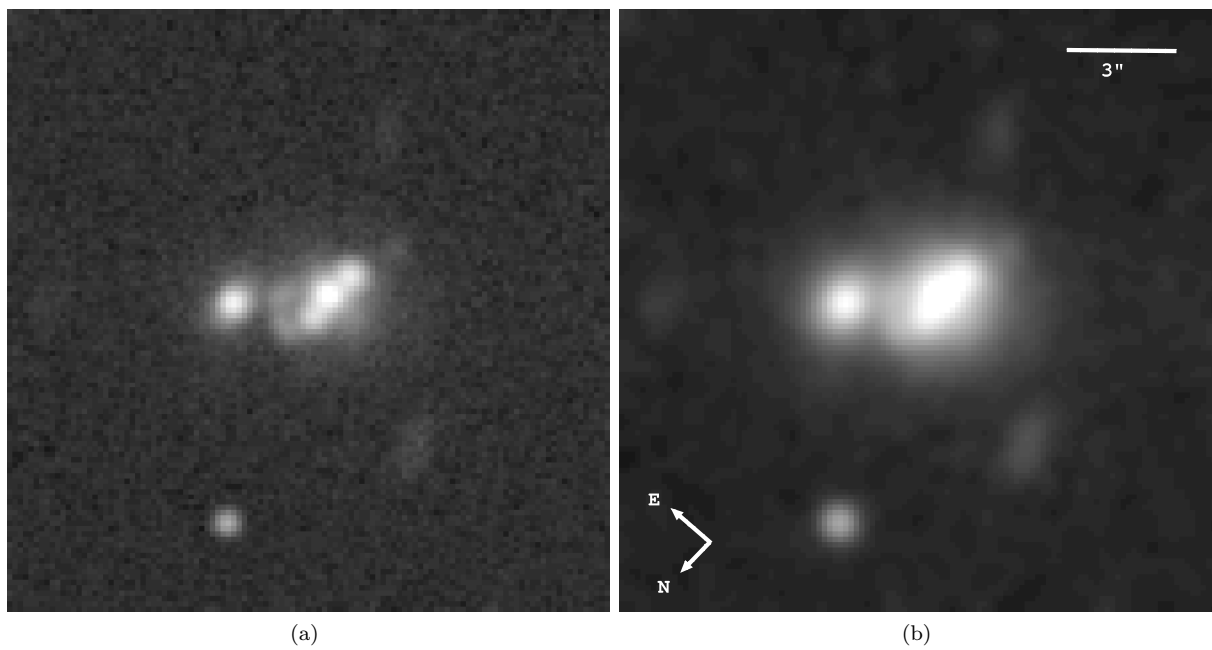


Figure B42. PKS 0117-15. (a) Unsharp-masked image. (b) Median filtered image.

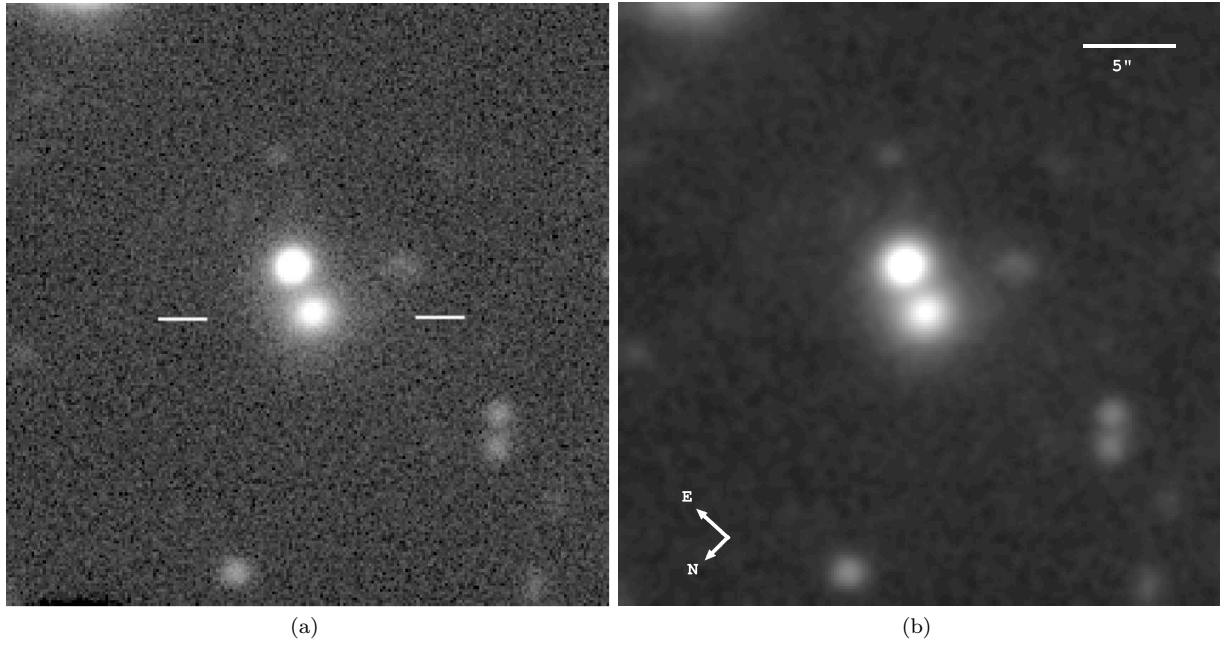


Figure B43. PKS 0252-71. (a) Unsharp-masked image. (b) Median filtered image.

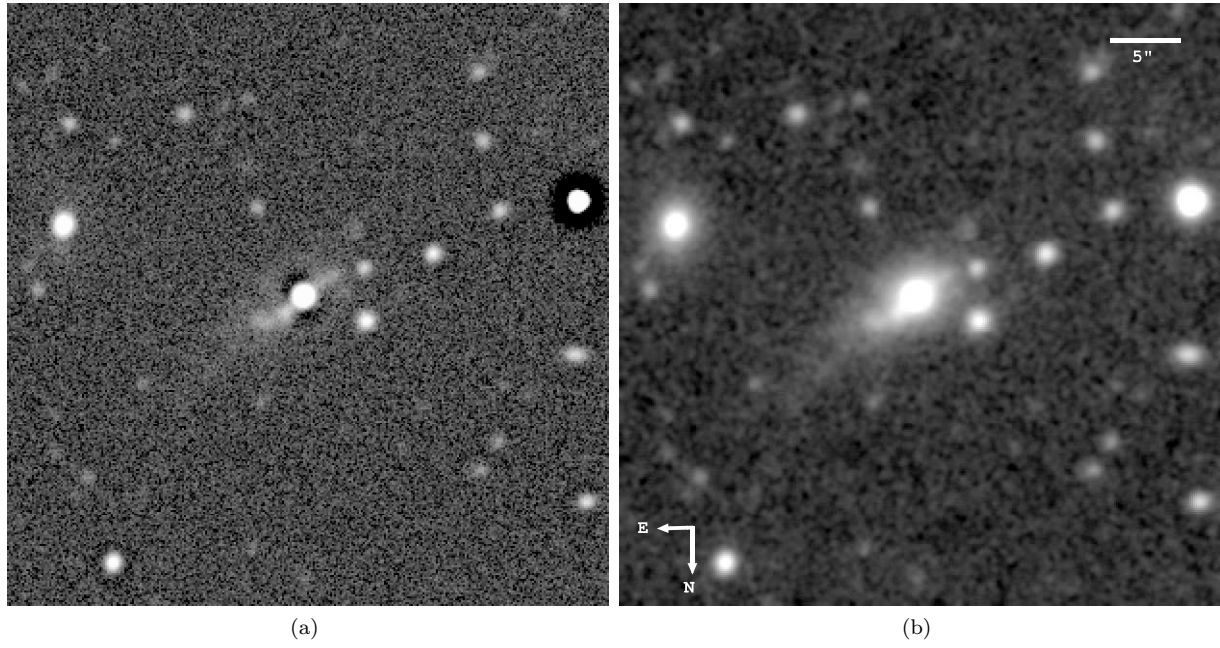


Figure B44. PKS 0235-19. (a) Unsharp-masked image. (b) Median filtered image.

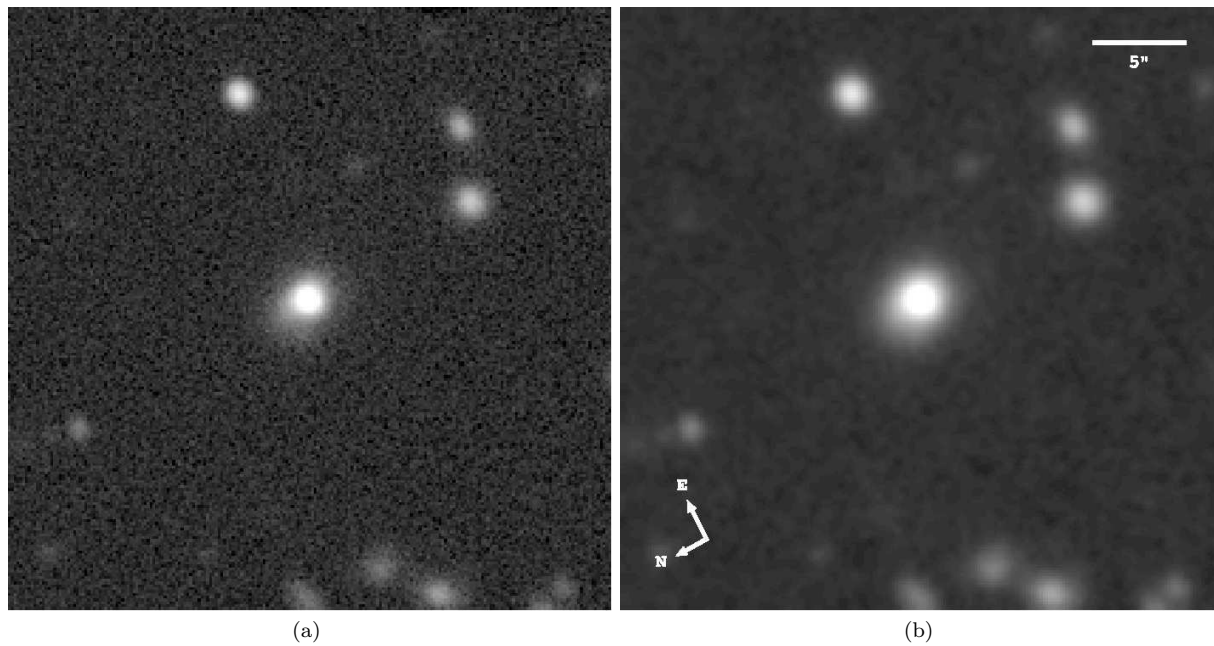


Figure B45. PKS 2135-20. (a) Unsharp-masked image. (b) Median filtered image.

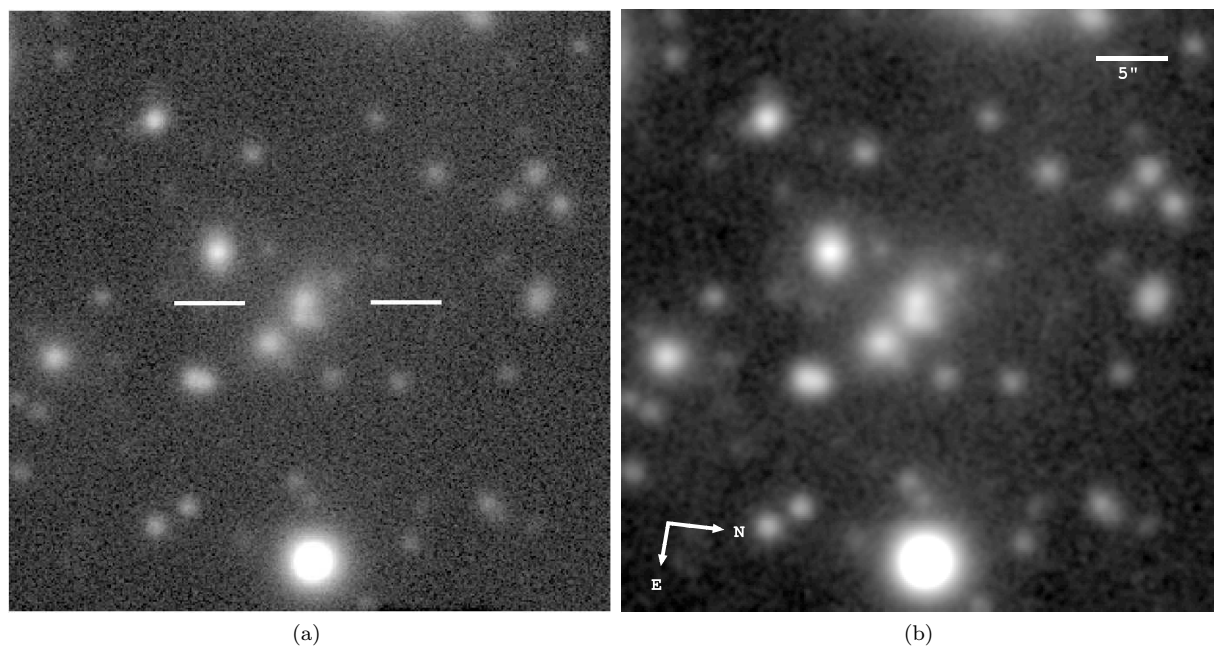


Figure B46. PKS 0409-75. (a) Unsharp-masked image. (b) Median filtered image.